STUDY ON CIRCULARLY POLARIZED SYNTHETIC APERTURE RADAR: PATCH ARRAY ANTENNAS AND SCATTERING EXPERIMENTS IN AN ANECHOIC CHAMBER

July 2016

MOHD ZAFRI BIN BAHARUDDIN

Graduate School of Advance Integration Science

CHIBA UNIVERSITY

（千葉大学審査学位論文）

STUDY ON CIRCULARLY POLARIZED SYNTHETIC APERTURE RADAR: PATCH ARRAY ANTENNAS AND SCATTERING EXPERIMENTS IN AN ANECHOIC CHAMBER

円偏波合成開口レーダの検討：電波無響室でのパッチアレイアンテナと散乱現象の実験

2016年7月

千葉大学大学院融合科学研究科

情報科学専攻知能情報コース

MOHD ZAFRI BIN BAHARUDDIN

TABLE OF CONTENTS

ABSTRACT

Observation of the Earth from aerial and space-borne platforms using synthetic aperture radar (SAR) has provided scientists and researchers with a deeper knowledge of the physical surface information of our planet. SAR imaging is typically performed using linearly polarized (LP) signals and has been extensively studied. Circularly polarized (CP) SAR imaging on the other hand is still in its early stages. Thus an investigation into using CP signals for SAR is desired. This thesis presents the design and testing of a SAR system using CP antennas, with an investigative focus on design of low side-lobe array antennas. With the aim of launching a CP SAR sensor for the purpose of remote sensing, a program to test the systems leading up to an unmanned aerial vehicle and eventually a satellite platform was planned. All related on-board subsystems of the SAR sensor must first be tested on the ground. In a preliminary study, a semi-automated rail enabled ground-based SAR imaging test-bed was developed and is able to function carrying L and C-band SAR systems. Measurements were performed outdoors on a corner reflector and LP imaging results are presented. Following this study, a controlled experiment was made in an anechoic chamber with the use of a vector network analyzer (VNA) and automated rotary turntable to mount targets. Measurements in the C-band were performed using CP signals. CP ISAR imaging results were compared with LP ISAR images. These works will lead to the investigation of generating images from CP receive and transmit signals, improvement of related imaging algorithms for CP signals and suitable antenna design. This thesis continues previous research on CP microstrip patch antennas for application in SAR measurements. Antenna designs are based on theory and design guidelines and were validated using electromagnetic simulation tools and measurements. Several prototype microstrip antenna designs were studied, fabricated using traditional PCB fabrication techniques and verified through performance parameter measurements. First, basic patch antenna shape were studied and compared for the best performance and design compromise based on material and fabrication method limitations. In the L-band, a proximity-coupled corner-truncated patch array antenna was designed. The antenna is an L-band 1.27 GHz, 2x5 element array that has been synthesized using the Dolph-Chebyshev method to reduce side-lobe levels. Fabricated antenna performance characteristics show good agreement with simulated results. A set of antennas were fabricated and then used together with the developed SAR system. Imaging results are discussed in this thesis. In the C-band, a planar CP, beam tilted, array antenna was studied. Several important antenna performance parameters customized to the utilized SAR systems were achieved in this study. Among them are low axial ratio of under 3dB with 130 MHz bandwidth via corner truncated square patches for circular polarization; steep scanning angle of 40 degrees using phased delayed 10-element array at 0.53 lambda element spacing; suppressed side-lobe level; and reduced radiation from spurious feeds through optimized feed network using T-junctions and mitered bends. The optimized design was fabricated and the array antenna performance parameters was verified through measurements in an anechoic chamber. Results show agreement between theoretical and simulated data which match the design parameters. The antennas and their connected SAR systems developed in this work are different from most previous work in that this work is utilizing circular polarization as opposed to linear polarization. To compare LP and CP results, a polarimetric analysis using theoretical scattering matrices was made.

ABSTRACT (JAPANESE)

合成開口レーダ（SAR: synthetic aperture radar）を用いた空や宇宙からの観測は地球表面の多くの情報を与える観測方法である．従来の SAR 画像取得方法は直線偏波（LP: linear polarization）のマイクロ波を用いた方法がなされており，円偏波（CP: circularly polarization）を用いた SAR の手法は未だ早熟であり，更なる研究が求められる．本論文では低サイドローブ CP アレイアンテナを用いた SAR システムの設計とその実験を紹介する．本研究は将来打ち上げ予定である CP-SAR 搭載航空機と人工衛星の開発につながる．しかし打ち上げ前に通常 SAR システムは地上で実験，検証を行わなければならない．そこでこの最初の検証実験として，L バンドと C バンドの地上型 SAR（GB-SAR: ground-based SAR）システムの開発を行った．本論文では二種類のアンテナである L バンドと C バンドのマイクロストリップアレイアンテナの設計作成を行った．L バンドのアンテナは地上実験用に開発され，電波無響室にてこのアンテナを搭載した SAR 実験を行った．C バンドのアンテナは航空機用に開発を行ったため，ビームチルトの機能が要求される．地上実験は三面コーナリフレクタとホーンアンテナを用いて屋外で行われ，LP-SAR 画像を得ることが出来た．この実験に続きベクトルネットワークアナライザ（VNA: vector network analyzer）とターゲットを回転させるターンテーブルを用いた SAR システム実験を逆 SAR（ISAR: inverse SAR）方式で電波無響室にて円偏波コーンアンテナを用いて実施した．得られた CP-SAR 画像を用いて LP-SAR 画像と比較し，円偏波 SAR 画像の偏波を用いた評価を行った．

LIST OF FIGURES

LIST OF TABLES

Chapter 1 INTRODUCTION

Polarization of antennas was first studied by Heinrich Hertz around 1886-1889 when he demonstrated that a receiver does not respond when the dipole antennas are aligned perpendicular to one another. He further showed that as the receiver is rotated the received signal increases and reaches a maximum strength when the dipole antennas are parallel [1]. Polarization of waves and antennas can be classified into three categories: linear, circular, and elliptical polarizations. Elliptical polarization is a general term and radio systems are rarely designed for use with this polarization specifically, even though linear and circular polarizations are the extreme special cases of elliptical polarization. Instead radio systems are typically designed to use linear or circular polarizations.

Linear polarization (LP) is easily generated and is commonly used for mobile phones, communications broadcasting, and automotive radar, among other classical radio applications. A pure LP signal should have only one electric field component, either horizontal or vertical. Thus, LP signals can be further classified as horizontal and vertical polarizations. Circular polarization (CP) on the other hand is used for global navigation satellite systems, near-field RFID and weather radar. CP also has two sub-classifications, left-handed and right-handed circularly polarized, depending on the rotation direction of the electric field vector [2]. A graphical representation of each polarization showing the electric field components is shown in Figure 1.1. The selection of polarization is based on the application as there are some characteristics of a polarized waveform that can be more advantageous for specific applications.

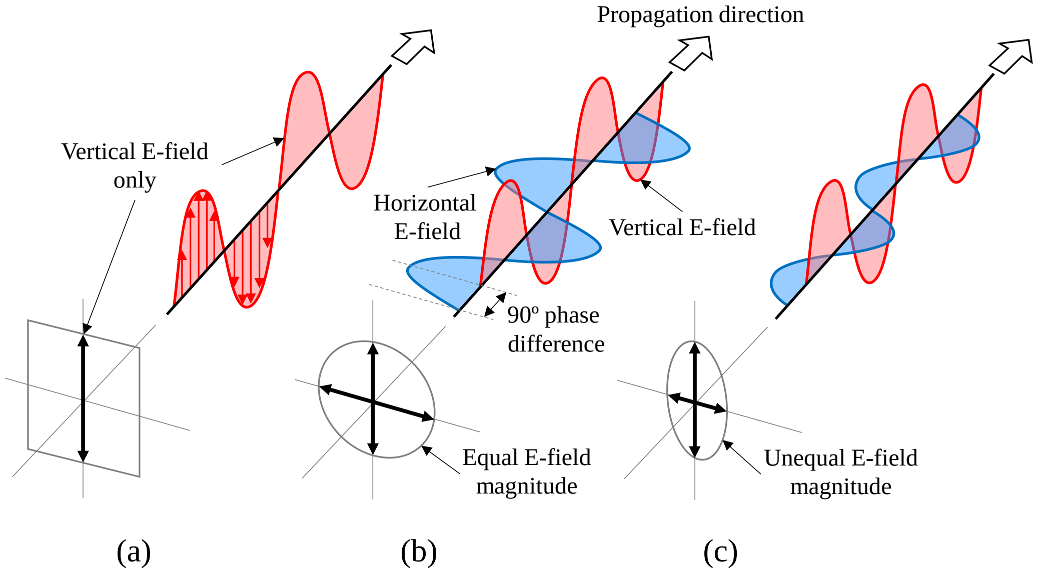

Figure 1.1: Polarizations of electromagnetic waves: (a) vertical linear polarization; (b) circular polarization; (c) elliptical polarization.

1.1 Circular Polarization

To generate circularly polarized radio signals, two orthogonal electric field components that are equal in amplitude and 90 degree phase shifted are required. Designing pure CP antennas without the use of external hardware such as a phase shifter is challenging. However, CP signals offer several benefits over LP signals:

1. **Immune to Faraday rotation.** As electromagnetic waves travel through the Earth's atmosphere, it experiences a rotation of the plane of polarization. This rotation occurs more in the upper atmosphere where the travelling wave is affected by ionized plasma that generates strong magnetic fields. Studies have shown that the Earth's magnetic field varies in strength throughout the globe, and depends on many other factors such as time of year and solar activity [3]. LP signals will be affected by this Faraday rotation and will experience polarization mismatch. Circular polarization however is immune to this effect because both orthogonal components have equal magnitude and are rotated by the same angle. This is the main reasoning for CP to be used in most Earth-to-space satellite communication systems [4].

2. **No multipath propagation.** Circularly polarized waves that are reflected by flat conductive surfaces will become counter polarized. For example, a right-handed CP wave will be reflected as a left-handed CP wave and vice-versa. This inherent property of the CP reflection allows the antenna to filter out reflected signals and is most beneficial to satellite based navigation systems [5]. CP is also advantageous in indoor based high data rate communications as it decreases interference between direct and reflected signals.
3. **No polarization loss due to misalignment.** Linearly polarized antennas must be precisely aligned to avoid polarization mismatch. CP antennas are not affected by polarization mismatch. Additionally, LP antennas can still receive pure CP signals with a loss of 3dB. This property is used in RFID tagging systems to ensure tags are detectable regardless of orientation.

1.2 Motivation and Challenges in using Circular Polarization for SAR

Circularly polarized antennas are to be designed to take advantage of the benefits stated in the previous section. Typical features of LP antennas such as wideband and pure polarization are not immediately available to CP antennas. The aim of this work is to propose antenna designs for use in an airborne or spaceborne SAR system. The antennas need to comply with designed SAR performance requirements, be circularly polarized, low mass, low profile, and include a beam that is shaped to reduce side-lobes and steered to a specified look angle. The designs are to be implemented in a synthetic aperture radar system.

Using an existing L-band pulse Doppler SAR measurement system [6], an initial pilot study was performed [7]. L-band has large wavelength which results in systems and equipment to be physically large. Measurements is only feasible in an outdoor range with large bulky reflector targets being placed at least 100 meters in range and a platform movement of at least 40 meters. Even though the pilot study was a success, the time consumption, man-power, equipment, and outdoor RF measurement licensing requirements [8] forced the study to be moved indoors.

This led to the development of an indoor reconfigurable wide-band vector network analyzer (VNA) based SAR system for testing antennas in different bands [9].

The setup was suitable for frequencies above 2 GHz. Lower frequencies are still possible but it is close range, almost near field. Several standard and custom designed LP and CP antennas were used to make SAR measurements in the indoor range. As opposed to the pulsed radar L-band system, this indoor VNA based system generates signals that are stepped frequency continuous wave (SFCW). SAR imaging with SFCW requires comparatively larger bandwidth to provide the same resolution.

To compare the LP and CP SAR imaging output, an understanding of polarimetric scattering is required. The scattering matrices for different target types are completely different between the two polarizations. An additional challenge imposed when performing polarimetric measurements is polarimetric calibration. LP calibration is well established but CP calibration is relatively unexplored. Calibration is an important step in the post-processing of the captured scattering results but is outside the scope of this thesis.

1.3 Research Summary

A synthetic aperture radar imaging system for studying imaging with circularly polarized antennas is developed in this thesis. This system is reconfigurable for imaging using a linear rail-based SAR or a turntable-based inverse SAR. This system uses a combination of range-gated stepped frequency continuous wave (SFCW) using a VNA as the transceiver, circularly polarized patch array antennas customized to specific frequency bands, and a back-projection algorithm (BPA) to produce the SAR image. The innovation in this thesis is mainly focused on developing circularly polarized array antennas as part of a new synthetic aperture radar system. Unlike previously developed systems which receive, transmit and process LP signals, the developed antennas and SAR measurement system were specifically designed for the study of CP signals for imaging from airborne or spaceborne platforms.

Several research topics were developed to accomplish this. Chapter 2 provides a brief background on SAR data collection geometry, synthetic imaging algorithms, state-of-the-art polarimetric SAR systems, followed by proposed innovations in antenna array design. In Chapter 3, an automated rail-based SAR measurement system was developed and tested in the L-band using linear polarization. After proving the functionality of the measurement system, Chapter 4 presents development of CP array antennas with reduced side-lobes to improve cross-range ambiguity. Beam tilting is also explored to conform to vertical mounting requirements of a targeted airborne platform installation. Finally, the CP antenna and SAR imaging system is integrated and CP measurements were performed in an anechoic chamber as presented in Chapter 5. It was found that CP imaging results are in agreement with theoretical analysis. Future work and conclusions are discussed in Chapter 6.

Chapter 2 SYNTHETIC APERTURE RADAR

An application utilizing radar systems that transmit a high power radio frequency signal and receives the backscattered echoes sequentially and then using decompression techniques to generate a high resolution image of the radar target is known as synthetic aperture radar (SAR). The SAR sensor itself is an imaging radar mounted on a moving platform. Electromagnetic waves are sequentially transmitted and the backscattered echoes are collected by the radar antenna. An appropriate number of received signals along the moving path allows the construction of a synthetic aperture that is much larger than the physical antenna length. The image that results after processing the raw data represents a measure of the scene reflectivity [10]. SAR has grown quickly over the last two decades to become one of the main instruments for remote sensing from airborne and space-borne platforms. Its inherent characteristics that provide high resolution images, all weather sensing and day and night monitoring have made it invaluable for remote sensing disaster monitoring applications [11] [12]. Past space-borne SAR systems are typically installed on relatively large satellites in the range of 1,000 to 4,000 kilograms such as the TerraSAR-X, ALOS and ALOS-2. Heavier payloads will require larger rockets with greater thrusts, which will inevitably be expensive to launch into orbit. Smaller and lighter satellites are cheaper to launch and can even be launched with other payloads as a piggyback [13].

With this in mind, the Josaphat Microwave Remote Sensing Laboratory (JMRSL) has embarked on a project to develop a unique space-borne SAR sensor with the aim of implementing the entire SAR system in a compact sized microsatellite. The proposed system is envisioned to be within 50 x 50 x 70 centimeters in size when stowed and weighing less than 100 kilograms [14]. Among the basic research planned to be conducted from the satellite is mapping of land surface, interferometry, and wave scattering mechanism of vegetation, snow or ice, rocks and desert areas. Potential applied research includes ocean monitoring, snow or ice monitoring and disaster monitoring.

Spaceborne SAR missions mostly operate in linear polarization (HH, VV, HV and VH) [4]. When linear polarized signals propagate through the Earth's atmosphere it can be sensitive to the Faraday rotation effect, particularly at low radio frequencies bands such as L-band. Our work focuses on a proposed circularly polarized synthetic aperture radar (CP-SAR) to obtain land deformation and physical information of the Earth's surface [14] [15].

In preparation for the spaceborne SAR imaging platform, an unmanned aerial vehicle (UAV) and an initial ground-based test-bed has been developed to evaluate outdoor performance of the required radio frequency (RF) transceiver, chirp-pulse generator and antenna subsystems [15]. The developed radar system uses a pulse compression signal processing technique as shown in the block diagram in Figure 2.1.

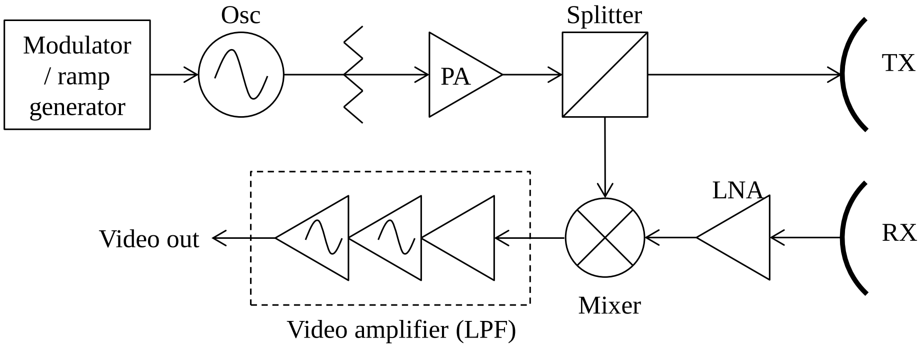

Figure 2.1: Pulse compression radar block diagram.

To test our antennas as well as imaging algorithms in a controlled environment, we have developed a simple SAR system for use in an anechoic chamber with a vector network analyzer (VNA) as the signal generator and capturing device. Already having a rotary turntable installed in our anechoic chamber, an inverse synthetic aperture radar (ISAR) configuration was adopted. A developed linear rail system was also used in experiments for comparison with the turntable results. As opposed to SAR, inverse SAR is an imaging method that utilizes relative motion of a target with respect to a stationary transceiver radar to generate an image of the target. As the radar beam remains fixed and while the target rotates, reflectivity data from different reflectors on the target can be measured.

Previous works on ISAR have introduced fundamental concepts for data collection and processing [16], studied on improving processing speeds by using Fast Fourier Transforms (FFT) instead of Discrete-Time Fourier Transform (DTFT) [17], or performed radar cross section measurements (RCS) using an ISAR configuration in an indoor measurement range [18]. The mentioned works included core concepts of ISAR as well as proposed techniques to improve image quality. The systems developed in this work are different from most previous work in that this work seeks to use circularly polarized (CP) radiation signals to generate images. This work will lead to the investigation of CP images, improvement of related imaging algorithms for CP signals and suitable antenna design.

2.1 Data collection Geometry

Inverse synthetic aperture radar is an imaging mode that takes into account the relative motion of a target with respect to a stationary transmitting/receiving antenna to image that said target [17]. To generate an ISAR image of a target from the returned signals two conditions need to be satisfied; (1) backscattered data has to be in two-dimensional format, (2) radar imaging geometry can provide returned data that contains slightly different geometrical information about the target. To comply with the two-dimensional format requirement, a frequency varying wave was used to obtain the range resolution for the first dimension. Two approaches were made to meet the second dimensional conditions: a rotary turntable for a rotational axis, and a linear rail for a Cartesian axis.

The measured backscattered signal can be interpreted as the radar cross section (RCS) of the target at the incident angle over the entire measurement bandwidth. There are various RCS measurements depending on the type of signal being transmitted [18]. We chose to measure the scattering data using a stepped frequency continuous wave (SFCW) in our measurements. In SFCW measurement, a band of frequencies are transmitted. This carries more information in terms of frequency components as compared to a single frequency element. Collected range response data is processed using matched filtering and Fast Fourier Transform to convert from frequency domain into time domain, and thus obtaining a measureable distance range profile [17] [19]. To generate the ISAR image, the data for each pixel is a two-dimensional inverse Fourier transform of range profiles of all the viewing angles [20] [21]. Reflection measurement geometry for the linear rail and rotary turntable based measurement is shown in Figure 2.2 and Figure 2.3 respectively.

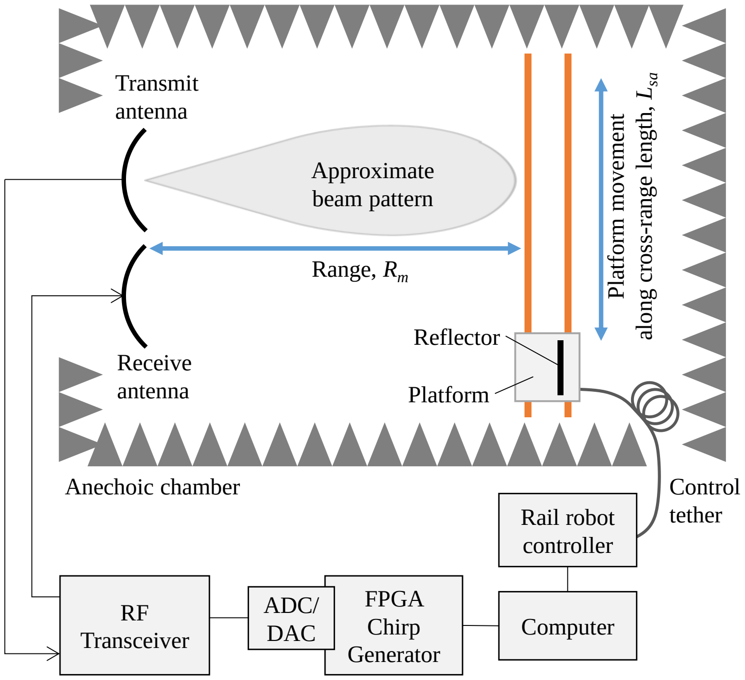

Figure 2.2: Linear rail based inverse SAR measurement layout and movement scheme in an anechoic chamber.

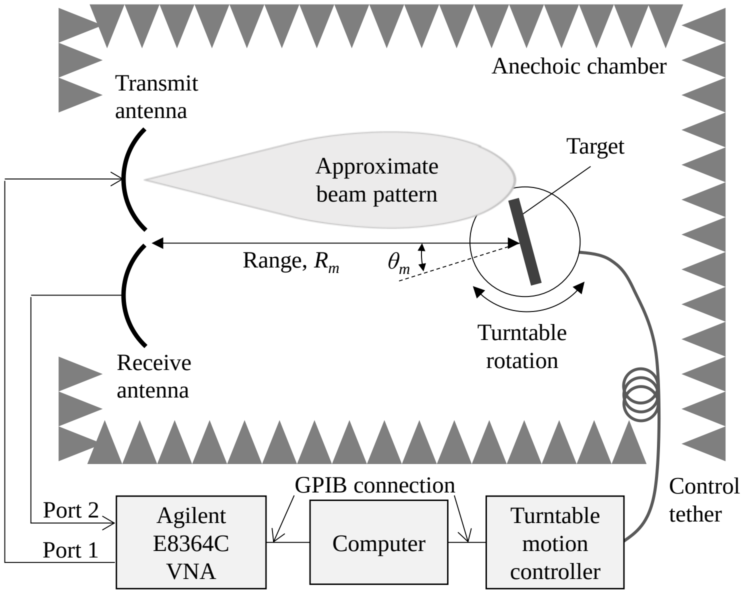

Figure 2.3: Rotary turntable based inverse SAR measurement layout and movement scheme in an anechoic chamber.

For a rotary turntable configuration in Figure 2.3, the reflection from the target can be considered as composed of multiple independent point reflectors that is proportionate to the scatterer reflectivity function ψ with the assumption that the antenna's radiation pattern is the same for all measured points in a cylindrical configuration [24]. The reflectivity function ψ is measured in the cylindrical coordinate $\psi(\rho,\phi)$, and then projected into the Cartesian image plane $\psi(x,y)$. The scattering parameters measured at a specified angle θ_m for a point scatterer target arbitrarily positioned at (x_0,y_0) or (ρ_0,ϕ_0) can be expressed as:

$$S_{\theta_m}(k_r) = \psi(\rho_0,\phi_0)\frac{1}{R_m^2}\exp(-jk_rR_m) \tag{2.1}$$

where k_r is the radiating signal two-way propagation wavenumber defined as $k_r = 4\pi f/c$, and R_m is the measured range distance from the antenna to the target. For expressing the scattering parameters viewed from every possible angle, Eq. (2.1) can simply be integrated over the entire view range as:

$$S_{\theta_m}(k_r) = \int_0^{2\pi}\int_0^{\infty}\psi(\rho_0,\phi_0)\frac{1}{R_m^2}\exp(-jk_rR_m)d\rho d\phi \tag{2.2}$$

2.2 Imaging Algorithms

In this work the back projection algorithm was utilized to process raw measured data for the image generation. The algorithm was made famous by [22] and has the advantage of being able to reconstruct images even when data is incomplete or not perfectly aligned to the measurement path. This makes it suitable for airborne missions where the flight path may shift or the aircraft body rolls slightly [23]. There has also been application of the back projection algorithm in prototype security systems to detect trespassers or concealed objects [24].

Back projection works by taking a number of finite projections of an object which is measured from the radar system. The projections are measured from different angles or views, each generating an image. The basic function of the algorithm is to simply run the projections back through the image, thus the name back-projection, to generate a rough approximation of the target object. These projections will add constructively in areas that have multiple scatterings. Projection reconstructed images will usually result in blurred artifacts surrounding the object, which can be removed by passing the image through a high pass filter.

The reflectivity image in the Cartesian plane is given by the inverse Fourier transform (IFT) of the reflectivity function, $\psi(x,y)$, as [24]:

$$\psi(x,y)=\int_{-\pi}^{\pi}\left[\int_{0}^{\infty}S_{\theta_m}(k_r)\exp(jk_rR_m)k_r dk_r\right]d\theta_m \tag{2.3}$$

The integral inside the bracket of Eq. (2.3) can be viewed as a one-dimensional IFT as a function $Q_{\theta_m}(k_r)=S_{\theta_m}(k_r)k_r$, evaluated at a specified range, R_m. By defining $q_{\theta_m}(r)$ as the IFT, Eq. (2.3) is simplified to:

$$\psi(x,y)=\int_{-\pi}^{\pi}q_{\theta_m}(R_m)d\theta_m \tag{2.4}$$

Eq. (2.4) is the back projection algorithm that is used in this study to generate Cartesian images from reflection measurements of targets on a rotating turntable. Implementation codes in MATLAB are presented in the Appendix.

2.3 SAR Polarizations / Radar Polarimetry

The polarization of radiation is an important property when discussing propagation and scattering of electromagnetic waves. Polarization refers to the electric field vector locus in the plane perpendicular to the propagation direction. The length of the vector denotes the wave amplitude and the rotation rate of the vector denotes the frequency of the wave. Polarization then refers to the shape and orientation of the pattern that is traced by the vector. Figure 1.1 visualizes this showing in (a) linear polarization where there is only a single electric field vector component that is either vertical or horizontal, (b) circular polarization where there are two orthogonal electric fields of equal amplitude that have a 90 degree phase shift between them, and (c) elliptical polarization where the amplitude and phase can be different between two orthogonal electric fields.

Depending on the property of the target, the transmitted wave can change after reflection and the backscattered wave can be in the form of different polarizations. The study and analysis of these receive and transmit polarization combinations is the science of radar polarimetry [26] [27].

2.3.1 Linearly polarized SAR

Most SAR radars are designed to transmit radiation that is either vertically polarized (V) or horizontally polarized (H). This is because polarization on either receiving or transmitting signals can be synthesized with distinct relationships between them. In this thesis, all receive-transmit pairs are ordered by the receive polarization, followed by the transmit polarization. There are four typical combinations of receive and transmit polarizations:

HH - horizontal transmit and horizontal receive

VV - vertical transmit and vertical receive

VH - vertical receive and horizontal transmit, and

HV - horizontal receive and vertical transmit.

HH and VV polarization combination is also referred to as “co-polarized” because the receiving and transmitting polarizations are the same. Likewise, the VH and HV combinations are referred to as “cross-polarized” because the receiving and transmitting polarizations are orthogonal to each other.

Polarimetric radar can be utilized to the find the scattering matrix or target response using two orthogonal polarizations. Given a known scattering matrix of a target, computation of any combination of incident and received polarization is possible. Through this polarimetric combination, the detectability of selected features in an image can be enhanced. This is where full polarimetric measurement is most powerful.

2.3.2 Compact-SAR

Compact polarimetry is a recent technique using dual-polarization SAR systems to construct quad-pol information. Compact polarimetry shows advantages of being able to reduce size, complexity, price and resolution of a SAR system while possibly maintaining the same capabilities of a full polarimetric system. First introduced by

Souyris et al. [28], the original setup uses a linearly polarized transmit antenna mounted 45 degrees with respect to the horizontal and vertical receive antennas.

Follow up research has included comparative studies of different Compact-SAR modes [29] such as those using circular polarization for transmit, and polarimetric calibration techniques [30]. Adoption of the Compact-SAR in actual application are being tested in the NASA-ISRO SAR Mission (NISAR) [31] and JAXA’s ALOS-2 experimental mode [32].

2.3.3 Circularly polarized SAR

The most recent mode in polarimetric construction of SAR images is the circularly polarized SAR (CP-SAR). In this mode, both receive and transmit antennas are circularly polarized (CP). Initial concepts have shown that polarimetric combinations in CP provide different backscattering information than that of linearly polarized systems [33] [34] [35] [36]. This can provide further insight into properties of observed targets. It is the aim of this work to contribute to the realization of the fully polarimetric circularly polarized SAR system.

2.4 Antennas

2.4.1 Antenna Design Methodology

The antenna design methodology is shown in the flowchart of Figure 2.4. Designing an antenna begins with considering the designed SAR requirements and combined with a new antenna concept. After drawing and designing the antenna, it is simulated in the FEKO full wave simulation tool. If the simulated performance parameters achieves the expected performance, the design is taken for fabrication. Prototype is fabricated in-house using traditional chemical etching process. The completed prototype is measured using an Agilent E8364C PNA Network Analyzer for the reflection coefficients. Far field radiation parameters such as the radiation pattern, gain and axial ratio are measured in the JMRSL anechoic chamber using the same network analyzer and an ETS Lindgren 3102 conical log spiral antenna. The chamber is installed with 45 cm long pyramidal carbon loaded urethane foam absorbers to suppress reflections. A rotary turntable in the chamber allows measurements to be performed in a single dimension. Measurement setup and calculations are made based on techniques recommended by the IEEE Std 149-1979 (R2008) Standard Test Procedures for Antennas [37].

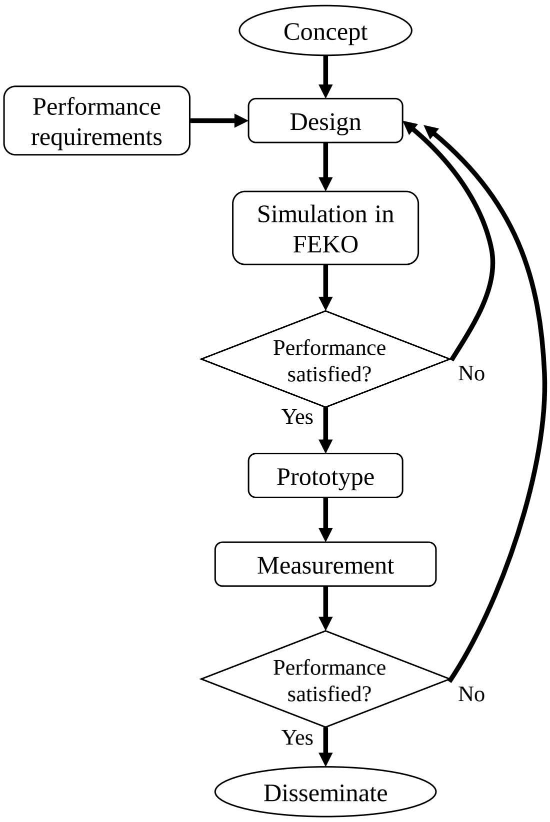

Figure 2.4: Methodology for designing an antenna.

2.4.2 Antenna Parameters

Antenna performance is evaluated based on many parameters. The antenna that is being tested for performance is known as the antenna under test (AUT). Generally antennas are designed specifically for each application, thus the importance of each parameter varies depending on its use. In the case of CP-SAR requirements, the following performance parameters are measured.

2.4.2.1 Reflection coefficient

Reflection coefficient is the amount of power that is reflected by a port *i*, referred to as S_{ii} measured in dB. According to the law of conservation of energy, any power that is not reflected gets converted into heat, or radiated by the antenna. Typically an antenna has a single port; port $i = 1$. Ideally an antenna port should reflect zero power, effectively radiating all the power. An antenna is considered good at radiating at a certain frequency, f, if the S_{11} at that frequency is below –10 dB. The range of frequencies where the criteria $S_{11}(f) < -10$ dB is fulfilled is called the impedance bandwidth. The S_{11} is measured directly at the antenna port using a vector network analyzer.

2.4.2.2 Radiation pattern and gain

It is very important to know the radiation direction of an antenna. This can be known from the antenna’s radiation pattern and gain. The radiation pattern shows the power radiated by the antenna at all angles as a function of θ and ϕ with the center of the antenna as the origin. The power values are normalized to its maximum value to provide information on the antenna angular properties. The radiation pattern alone, however, does not provide information on the exact power being radiated.

Directivity is a measure of how directional an antenna is. An antenna with zero directionality radiates equally in all directions (isotropic), thus this antenna would have a directivity of 1 (or 0 dB). Conversely an antenna that is very directional will have a high directivity value. In remote sensing, such as our application of antennas in SAR, would require an antenna with relatively high directivity to maximize power transfer and to reduce signals from undesirable directions. Directivity of an AUT can be defined as ratio of radiation intensity in a specified direction to the radiation intensity of an isotropic antenna. The radiation intensity of an isotropic antenna, U_{iso}, can be written as:

$$U_{iso}(\theta,\phi) = \frac{P_{rad}}{4\pi} \tag{2.5}$$

where P_{rad} is the total radiated power.

Using this with the directivity definition, an AUT would have a directivity, D, of:

$$D = \frac{U_{AUT}(\theta,\phi)}{U_{iso}(\theta,\phi)} = \frac{4\pi U_{AUT}(\theta,\phi)}{P_{rad}} \tag{2.6}$$

where $U_{AUT}(\theta,\phi)$ is the radiation intensity at a specified direction. However, it is very difficult to practically measure the total radiated power. Thus the definitions of gain and realized gain are used as acceptable performance parameters.

The gain of an antenna describes how much power is radiated in the peak radiation direction compared to that of an isotropic antenna, which should be all the power that is not reflected at the input port. The gain, G, in a specified direction can be calculated as:

$$G = \frac{4\pi U_{AUT}(\theta,\phi)}{P_{in}} \tag{2.7}$$

where P_{in} is the electrical power received by the AUT. Gain can also be defined as directivity multiplied by the radiation efficiency, which in turn is a ratio of total radiated power over input power. In practical measurements, the gain of the AUT is the ratio of measured power in a given direction to the measured power of a reference antenna in a reference direction. The gain value is dimensionless and express in decibel isotropic (dBi). Dipole antennas are used as reference antennas to calculate the gain. A set of left and right-handed circularly polarized conical spiral log antennas were used as gain standard antennas for their high degree of polarization purity. Gains measured with reference to these circularly polarized antennas are expressed in dBiC.

2.4.2.3 Axial ratio

Axial ratio (AR) is a measurement of polarization purity of the AUT to be circularly polarized. Circularly polarized signals consists of two orthogonal E-field components of equal magnitude that are 90 degrees out of phase. The axial ratio is then the ratio of the two E-field components. A pure circularly polarized wave has an AR of 1 (or 0 dB), whereas a linearly polarized wave has an AR = ∞. In CP antenna measurement, AR is the cross polarization ratio between LHCP and RHCP radiation intensity in a given direction, given by the following equation [38]:

$$AR_{dB} = 20\log_{10}\left(\frac{1+10^{-\frac{|U_{RHCP}-U_{LHCP}|}{20}}}{1-10^{-\frac{|U_{RHCP}-U_{LHCP}|}{20}}}\right) \tag{2.4}$$

where U_{RHCP} and U_{LHCP} are the measured radiation intensities in dB for a specified angle and frequency with respect to the reference RHCP and LHCP antennas.

The axial ratio bandwidth is the frequency range where the AR value is under a specified value. In this study, an antenna is considered to be circularly polarized when it has an AR of under 3-dB. The radiation pattern can be given by an amplitude, phase, and polarization at each direction of space.

2.4.3 Horn Antennas

In terms of antenna design, it is possible to modify the feed method of an LP antenna for it to generate CP signals. For example an LP quad-ridged horn antenna can have two input ports, one for horizontal and another for vertical polarization. If a signal is input into a 90 degree phase shift splitter, the in-phase output and 90 degree phase shifted output can together be fed into the LP horn antenna to generate a CP signal. An example of this is shown in the circuit and image of Figure 2.5.

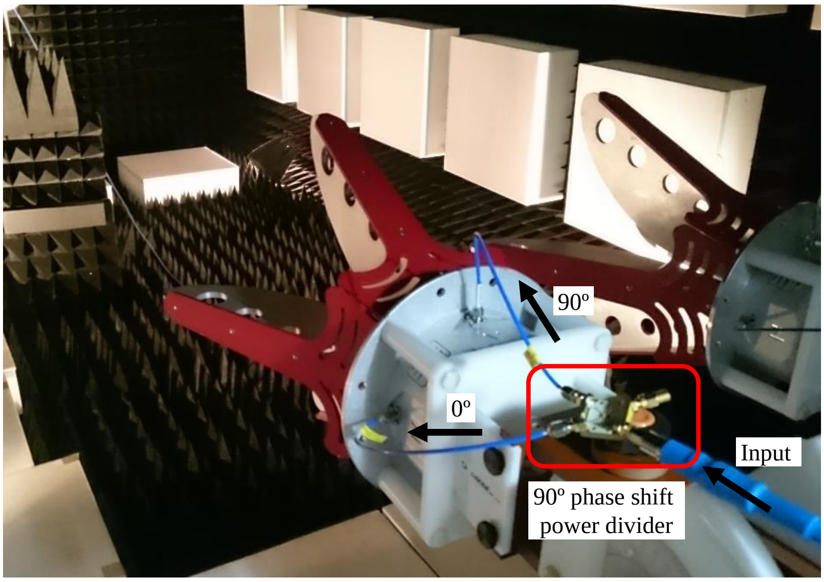

Figure 2.5: A linearly polarized horn antenna used to generate a circularly polarized signal using a 90 degree phase shifter.

2.4.4 Microstrip Patch Antennas

Microstrip patch antenna technology has matured since it was introduced in the year 1953. It is now widely used in mobile phones, aircraft radar, interplanetary communications, and satellites, where size, low profile, weight, performance and ease of installation are requirements. They are relatively simple and inexpensive to manufacture using traditional printed circuit techniques. When mounted on rigid bodies, they are very robust and can conform to different shapes. Patch antennas have some drawbacks however, in terms of low efficiency, low power, low polarization purity, spurious feed radiation and very narrow frequency impedance bandwidth [2]. Over the years, researchers have improved patch antenna designs to overcome the said drawbacks but balancing the performance with design complexity is an engineering challenge.

2.4.4.1 Feeding techniques

The antennas required in this study need to be circularly polarized. CP can be achieved by exciting two orthogonal modes with a 90 degree time-phase difference between them. For CP enabled patch antennas, there exist several prominent techniques. For a square shaped element, circular polarization can be generated by simply feeding the patch at two adjacent sides with signals that are 90 degree phase shifted from each other. This method adds complexity to the feed and can be difficult to design especially for large arrays. The two feed method can also be used in coax fed circular patches.

Since the feed network for multiple feed can be quite challenging and contribute to spurious radiation, a single feed is preferred. For a single feed, there are designs to excite the patch diagonally from a corner of a nearly square patch. Rectangular patches can also be fed along the diagonal line to create circular polarization. These designs will result in a very narrow bandwidth.

2.4.4.2 Truncated corner

Another popular single feed technique is to generate CP signals by truncating two opposite corners of a square patch. The truncation will cause rotation of surface waves on the patch which in turn will radiate circularly polarized signals. This method has the advantage of simple feed network, highly reduced unwanted spurious radiation, and wider axial ratio bandwidth compared to the diagonal feed.

2.4.4.3 Spiral antennas

Spiral antennas are used in ultra-wideband (UWB) applications. These antennas are defined by angles, such that they are also referred to as frequency independent antennas. They are however significantly larger in size and the beam pattern changes depending on the input frequency. The antenna generates an RHCP beam on one side and an opposite LHCP on the reverse side. Since the frequency range is very wide, reflectors cannot be used to block the rear lobe. Reflectors need to be placed $\lambda_0/4$ away and would thus make it frequency dependent. Absorbers can be used on the other hand but this will reduce the efficiency by half.

Chapter 3 SEMI-AUTOMATED SAR TESTBED

An initial ground-based test-bed was developed to evaluate the performance of the required radio frequency (RF) transceiver, chirp-pulse generator and antenna subsystems in a pilot study. The aim of the test-bed is to safely perform ground tests on all the required SAR and flight control subsystems, while also finding the best setting to provide the fastest scan time along the azimuth or cross-range length using the rails. The rail imaging platform and its systems developed in this work are different from most previous work [39] [40] in that this work is in the L-band, which entails relatively larger sized hardware due to the longer wavelength. This chapter presents the RF subsystem, which generates, transmits and receives the electromagnetic waves at the front-end and also the developed rail-based Positioner Subsystem moving platform.

3.1 System implementation

The developed rail-based SAR imaging platform simulates the linear movement of an airplane or satellite and forms the aperture required for a ground-based SAR system. As shown in Figure 3.1, our ground-based SAR is divided into (1) the RF Subsystem, which generates, transmits and receives the electromagnetic waves; and (2) the Positioner Subsystem, which manages all movement of the rail platform. All components under the box marked “Positioner Moving Platform” are mounted on the rail and are moved all at once. Platform movement controls are managed by equipment at the control station. A technical specifications summary of the SAR system is shown in Table 3.1

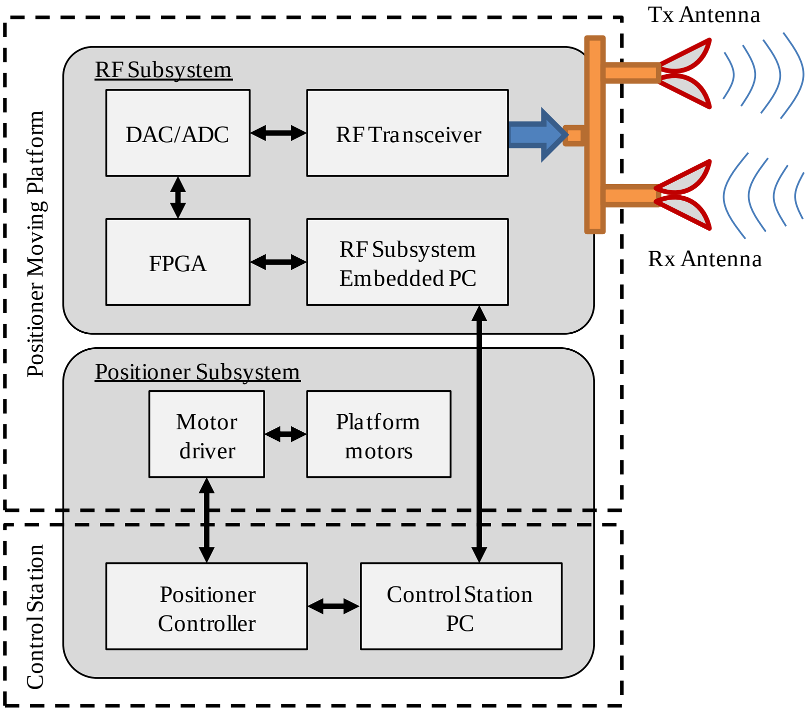

Figure 3.1: SAR rail imaging platform system block diagram

Table 3.1: SAR imaging system design specifications

No.	**Rail SAR Technical Specifications**		
	Specifications	***Design Value***	***Remarks***
1.	Operating frequency	1.27 GHz	L-band, $\lambda = 23.6$cm
2.	Bandwidth	100 MHz	Resolution: 1 meter (azimuth), 1 meter (range)
3.	Waveform, pulse width	FM Pulse	0.5µs pulse width
4.	Polarization	Single, VV	VV transmit and receive
5.	Antenna Aperture	30 cm	Quad-ridged horn antenna
6.	Antenna Gain	20.4 dB	47 dBm transmit power
7.	3dB beamwidth	30.0°	Azimuth range illumination: ~200 m at range distance 1000 m
8.	Signal-to-noise ratio (SNR)	> 10 dB	at 1000 m
9.	Overall Sensor Weight	< 35 kg	

3.1.1 RF Subsystem

The RF Subsystem consists of the RF Transceiver embedded computer which saves raw data and controls the FPGA. The FPGA generates the chirp pulse and triggers the RF Transceiver to transmit and receive the radar pulse. The digital-analog converter (DAC/ADC) handles signal con-version between the FPGA and RF Transceiver. Our customized RF Transceiver takes the chirp-pulse and runs it through a high power amplifier (HPA) to be transmitted by the antenna. Two open boundary quad-ridged horn antennas were used for their good gain and low VSWR in the L-band. Two antennas are used; one for transmit, another for receive. Both antennas are set to vertical polarization (VV).

The system uses a pulse-Doppler radar architecture. Our system's operating center frequency is in the L-band because this frequency band is suitable for deep penetration of media. Among the planned observation targets are vegetation, snow and soil. The RF transceiver is designed with a rated transmit output power of 50 Watts. Sizing for the system begins with calculations suggested by [1]. The implemented system operates at 1.27 GHz with a bandwidth of 100 MHz. The horn antenna has a 30 centimeter diameter d_a and thus an azimuth antenna beamwidth of

$$\Theta_a = \frac{\lambda}{d_a} = \frac{0.236}{0.3} = 0.786\,\text{rad} \tag{3.1}$$

where λ is the wavelength. The slant range resolution δ_r is inversely proportional to the system bandwidth according to $\delta_r = c_0/2B_r$, where c_0 is the speed of light. This is followed by the synthetic aperture length given by $L_{sa} = \lambda r_0/d_a = 70.81$ meters and azimuth resolution:

$$\Theta_a = r_0 \frac{\lambda}{2L_{sa}} = \frac{d_a}{2} = 0.15\,\text{meters} \tag{3.2}$$

This resolution can be achieved using multi-pass techniques. Thus, for single pass scans we have assumed an image resolution of 1 meter. Figure 3.2 shows the radiation pattern of the horn antenna employed in this SAR ground measurement [41]. It can be seen in the figure that the 3dB beamwidth of the horn antenna is approximately 30.0°.

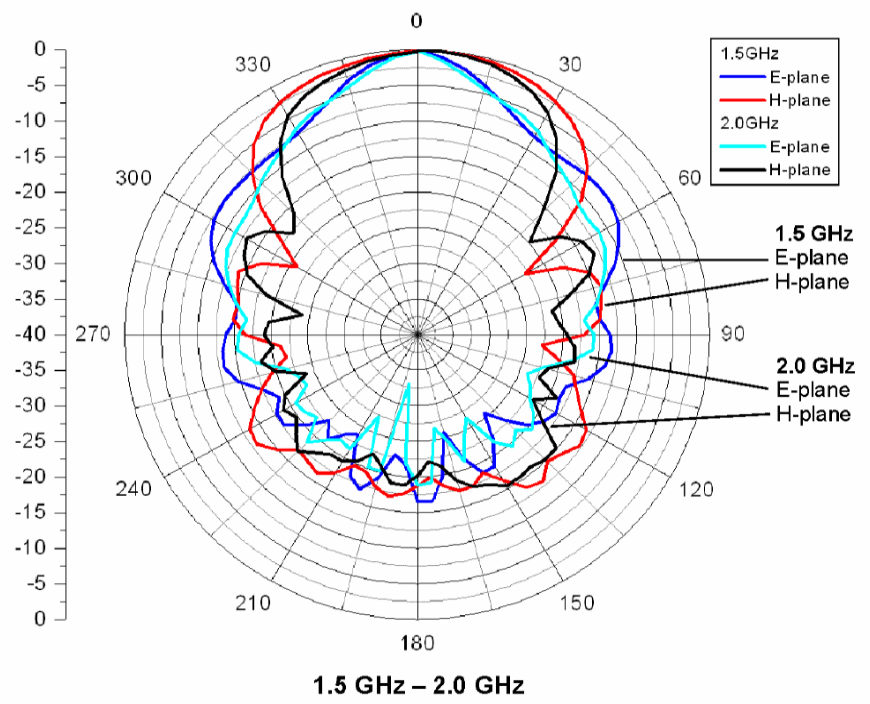

Figure 3.2: Radiation pattern of the ETS Lindgren quad-ridged horn antenna at the operating frequency [41].

The radar system front-end is the RF Transceiver module and can be seen in the block diagram of Figure 3.3. LO is the local oscillator generating the 1.27 GHz sinusoidal continuous waveform. The LO signal is modulated with the chirp signal coming from the digital-to-analog converter (DAC). Band-pass filters (BPF) are used to reduce noise distributed by nearby components. The modulated signal is fed through a high-power amplifier (HPA) to achieve the pulse transmission output power of 47 dBm. The amplified signal is then fed through a 3-port circulator with a 50 Ω matched load on one of the circulator ports. This effectively makes it an isolator to block any unwanted return signals that may come from the antennas. The chirp signal from the circulator is then radiated towards the target scene via the transmit horn antenna.

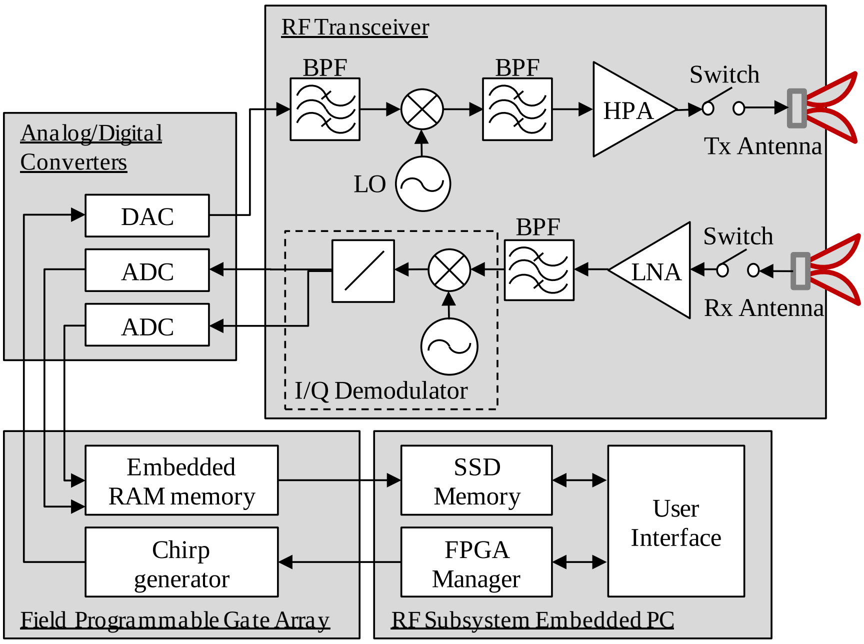

Figure 3.3: Main components of the RF Subsystem.

Reflected signals from the target scene are then received by the receive antenna, passed through a circulator and limiter. Since return signals are typically much smaller than the transmit signal, signals from the receive antenna are fed through a low-noise amplifier (LNA) with 30 dB gain. The output of the LNA is fed through a band-pass filter and continues into the RF port of the mixer in the I/Q de-modulator. The intermediate frequency (IF) output of the mixer is passed through an in-phase (I) and quadrature-phase (Q) demodulator. The IQ signals are then digitized using a pair of analog to digital converters (ADC). These IQ signals contain the frequencies which provide the range to target information.

To test the RF Subsystem, the RF chirp-pulse amplified output is looped back through 200 and 100 nanosecond delay lines and attenuators back into the transceiver input. The respective I and Q signals for the 200 nanosecond delay line loopback test are shown in Figure 3.4. After performing inverse fast Fourier transform (IFFT) on the IQ signals, the range measurement shows a peak at 30 meters as shown in Figure 3.5. This corresponds to the length of the delay line being used.

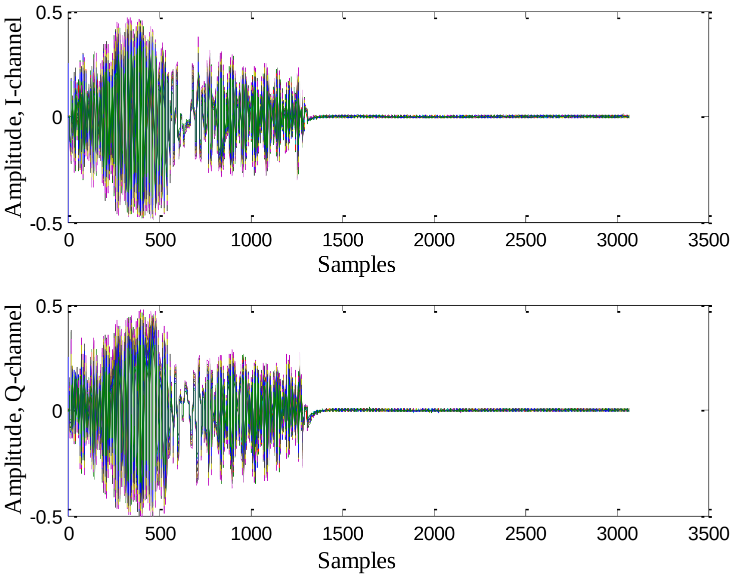

Figure 3.4: IQ received signals from a 200 nanosecond loopback test.

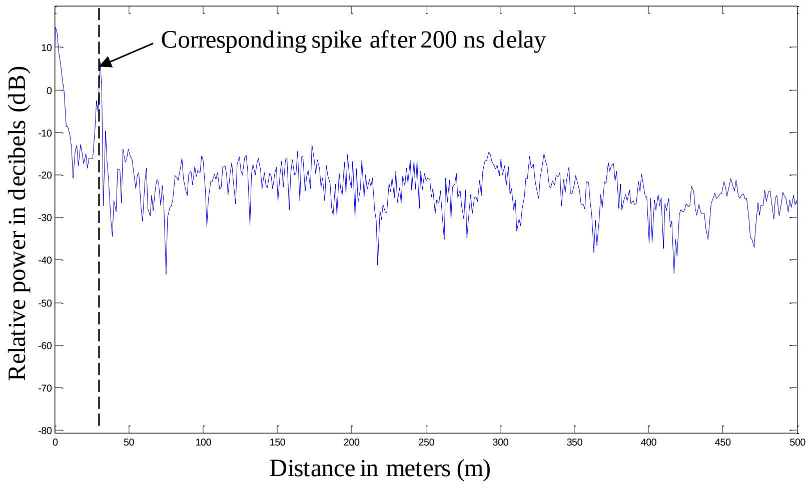

Figure 3.5: Range measurement from a 200 nanosecond loopback test.

3.1.2 Positioner subsystem

The RF Subsystem is carried by the moving platform controlled by the Positioner Subsystem. The antenna Positioner Subsystem ensures the moving platform is positioned according to the movement interval requirements along the cross range. All SAR subsystems were placed on the Positioner moving platform to reduce RF power losses and signal delays since the cross range distance of 50 meters would have required coaxial cables that are far too long.

Due to the criticality for the raw data to be as precise as possible, the Positioner is designed to have a precision of 0.1mm. The ramp up and ramp down speeds have been tuned to minimize vibrations that would otherwise be apparent due to the large inertia caused by the relatively large mass of the system. A complete system installation with the Positioner mast, two horn antennas, RF transceiver, chirp generator and data collector add up to a total of 30kg of mass.

Movement sequence of the platform is managed by a user interface on the Control Station PC where the user inputs parameters such as total distance, interval length and motor speed. The user interface sends speed and position commands to the motor Positioner Controller module via a General Purpose Interface Bus (GPIB). The Positioner Controller then controls the rotation speed of the motor and onboard encoders provide rotational position feedback.

For each interval the Control Station PC moves the platform to the desired location, and then sends a command via network socket to the RF Subsystem Embedded PC, which in turn controls the radar to transmit a chirp-pulse signal. Once the RF Subsystem process of receiving and saving the raw range profile data has been completed the embedded PC will send a flag to the Control Station PC. The Control Station PC will move the platform to the next interval and the process repeats itself automatically for the entire cross-range distance. It is further planned to have real-time onboard data processing to provide better radiometric calibration accuracy as opposed to offline post-processing.

The rail itself is of modular design, each being 1.5 meter in length. This enables us to move the platform along any arbitrary distance, given a sufficiently flat length of area. Several movement schemes can be chosen on the user interface. In the “semi-automatic” scheme the user has to manually send the move and transmit commands on the user interface. This is akin to a stop-and-go movement and is useful for troubleshooting. The “automatic with stops on interval” scheme will move the platform to each interval, stops on the interval location, and captures the range profile automatically. The “automatic continuous” scheme moves and captures profiles while moving. Figure 3.6 shows the Positioner Subsystem on-site experiment layout and movement scheme. The RF front end, with the transmit and receive antennas mounted on the mobile platform, is shown in Figure 3.7.

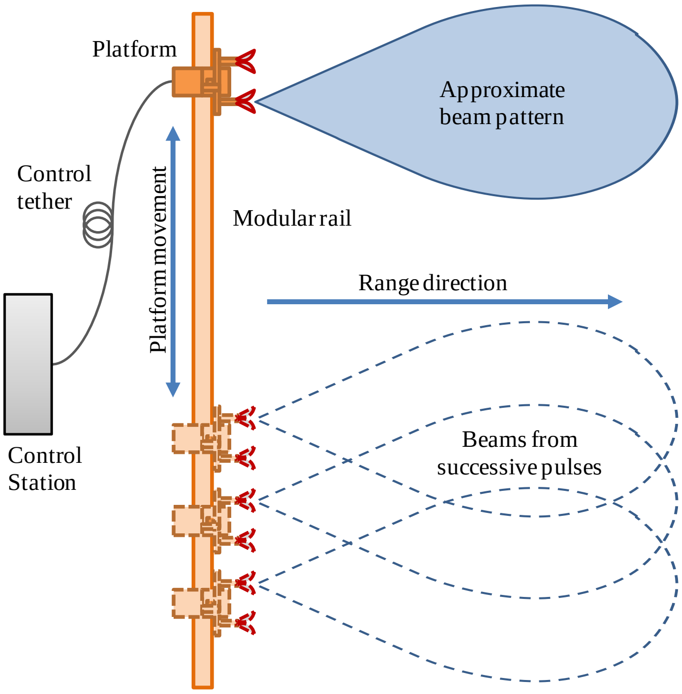

Figure 3.6: Positioner Subsystem layout and movement scheme.

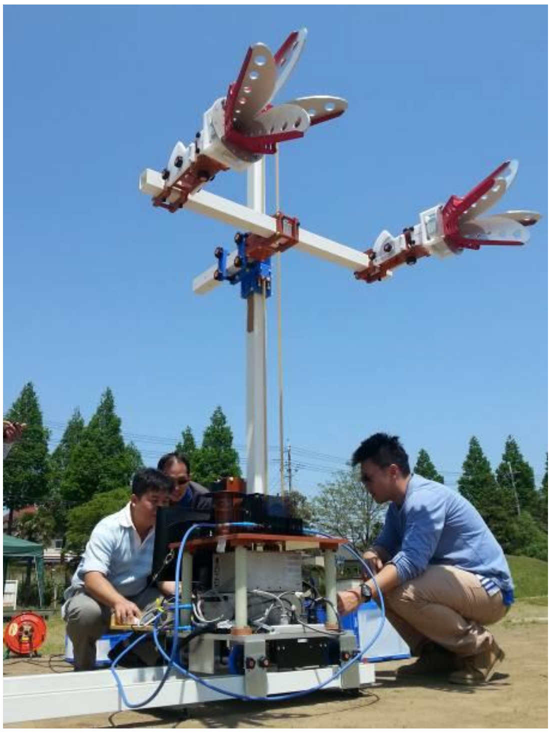

Figure 3.7: The Positioner Rail SAR Imaging System mounted on modular rails used on the test site.

3.2 Ground test and measured data

A 50 meter long track was prepared on an open field with low background clutter. A trihedral corner reflector was installed at a distance of 90 meters from the track, one meter above the ground, to act as a point target. This arrangement is shown in Figure 3.8. The side length of the trihedral should ideally be 10 times the signal wavelength [43]. Working at 1.27 GHz the corner reflector should have a size of 2.5 meters on each side. This is prohibitively difficult thus a 1.80 meter trihedral corner reflector was used instead. Our corner reflector was made using 0.6mm thick aluminum sheets backed by 10mm thick plywood. This will result in a smaller than desired point target reflection reading.

In this experiment the platform moves along the high precision track at 100 mm per interval, which would yield roughly 450 sample points along the azimuth. The "semi-automatic" movement scheme was employed. Captured data at each interval would be stamped with its corresponding source location relative to the movement on the track.

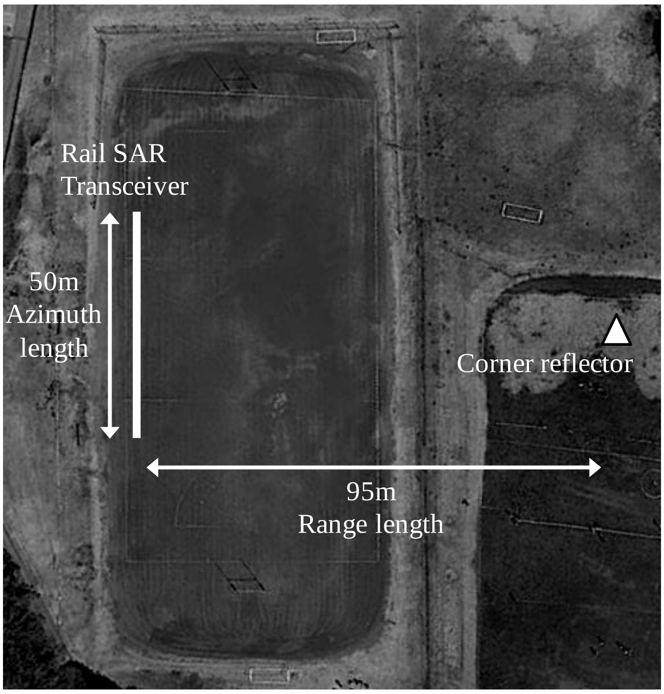

Figure 3.8: Arrangement of rail SAR transceiver and target corner reflector on test site.

A series of field experiments have been conducted to verify the performance of the CP-SAR system. These include point target measurement as mentioned in section 3.1.1, and ground-based SAR experiments using the developed moving platform. After range compression, an ideal point target appears at each pixel of the recorded raw image with the same amplitude. Azimuth range compression is achieved by multiplying the azimuth range sample with the complex conjugate of the baseband reference signal at frequency domain, and finally, the resultant signal is inverse Fourier transformed to yield a focused image in both range and azimuth domain [44].

During the ground measurement, the system (antenna and sensor) was mounted on the Positioner moving platform, facing perpendicularly to the identified natural target. Radar echoes were captured in a stop-and-go manner with ground displacement of 100 mm, along the 50 meter ground track.

The collected data was processed using a unique SAR signal processing technique named Range Doppler Algorithm (RDA) [44]. RDA uses frequency domain calculations in both range and azimuth. Each dimension is operated separately and in the algorithm a range cell migration technique (RCMC) is performed in the range Doppler domain. Figure 3.9 shows the point target return of trihedral at a distance of 92 meters.

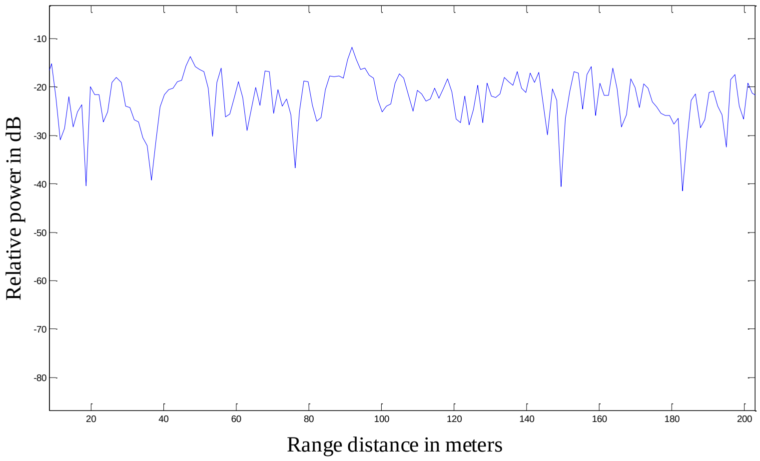

Figure 3.9: Range measurement with point target return of trihedral detected at a distance of 92 meters.

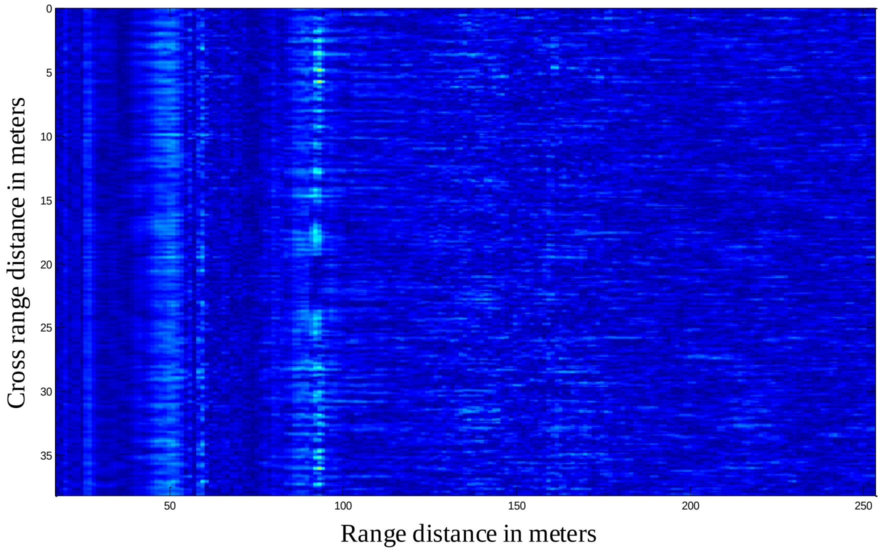

Figure 3.10: SAR Image obtained using datasets from 381 points.

The image obtained from this stop-and-go ground measurement is shown in Figure 3.10. Incomplete focus of the point target seen in Figure 3.10 is due to total collected datasets in the measurement is only 381 points and the measurement was forced to stop due to bad weather conditions. The corner reflector could still be sufficiently detected even though it is not at the optimum size. There is a fence along the 60 meter mark which clearly is providing some unwanted reflections.

A new L-band ground-based SAR system operating at 1.27 GHz has been designed and developed. The CP-SAR system can potentially provide high resolution of SAR imagery for disaster monitoring. The Positioner moving platform that was presented provided a stable test-bed to assess the L-band SAR imaging system. Setting up the entire system does take considerable time due to large component sizes – but the benefit of this rail is providing a stable and accurate positioning for SAR ground measurement and experimentation.

Chapter 4 ANTENNA DESIGN

One of the most important subsystems of the SAR system is the antenna. Antenna radiation patterns have side-lobes that add to ambiguity in the form of ghosting and object repetition in SAR images. Applying filtering, such as the Hamming, to reduce side-lobe level effects has a drawback of degrading image resolution. The aim of this work is to develop an antenna suitable for the SAR system that has been designed with a focus on side-lobe reduction using Dolph-Chebyshev synthesis and optimized feed network. This chapter presents the development process of the proximity-coupled corner-truncated patch array antenna. The proposed antenna was designed and then simulated using the FEKO electromagnetic simulation tool before fabrication.

4.1 Reduced side-lobe Circularly Polarized Array Antenna

The radiation pattern design of the SAR antenna depends on factors such as azimuth ambiguity, range ambiguity, range gain variation, and reflections from the surrounding structures [47]. Range ambiguity is caused by echoes received from earlier or later pulses arriving back to the antenna at the same time as the desired echo. Range gain variation occurs due to the side-looking scan method. Correction is required to compensate the difference of power delivered in range due to a large scan swath. Proper design of the antenna fixture and suppression of the side-lobes can reduce reflection significantly. SAR performance parameters were set and used to design the array antenna. Microstrip patch antenna technology was chosen as it is lightweight and has the potential to achieve the design requirements with proper design.

The proposed L-band proximity-coupled corner-truncated patch array antenna is an iteration of our own previous design [45]. This array consists of 10 elements in a 2 x 5 arrangement. Each square radiating patch has a side length of 79 mm to operate at the center frequency of 1.27 GHz. Circular polarization is achieved by truncated corners. Two substrate layers are used for a total thickness of 3.2 mm; the top layer consists of the radiating patches, the middle layer is the feed network which includes T-junction power dividers. Quarter-wave transformers are employed to provide better matching along the feed network. The feed line has a width of 5 mm to achieve an impedance of 50 Ω. The last copper layer is the ground plane. In this work we have employed the NPC-H220A substrate from Nippon Pillar Corporation, having a thickness of 1.6 mm, a relative permittivity of $\varepsilon_r = 2.17$, and a loss tangent of $\delta = 0.0005$.

4.1.1 Single element design

The first step is to design a single radiating patch, which will then be used as elements in an array. A square patch with truncated corners is used. Changing the patch size will change the center operating frequency. The feed point, determined by the distance Fd, is offset from the center of the patch to provide optimum reflection coefficient. Varying the truncation size will affect the axial ratio (AR), and thus the level of circular polarization. Several samples made during the optimization process is shown in Figure 4.1. By optimizing the corner truncation length, C, the axial ratio can be minimized. When using the same design in an array, the suitable truncation size requires re-optimization as its size depends greatly on the overall patch size, patch spacing and feed network.

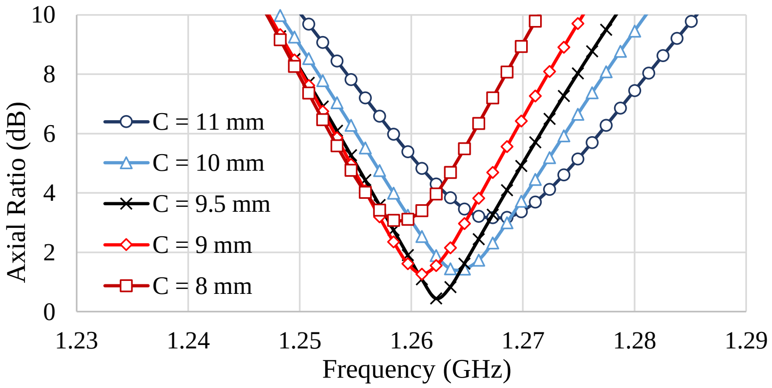

Figure 4.1: Effect of corner truncation size, C, on the axial ratio.

4.1.2 Array design

An array with uniform power division typically results in good gain in the main lobe, but also large side-lobe levels which can add to ambiguity. To further reduce the signal-to-noise ambiguity, the side-lobes are reduced by utilizing the Dolph-Chebyshev synthesis method.

The movement of the SAR sensor across the target area results in a Doppler frequency shift proportional to the relative velocity of the target, and a time delay proportional to the range distance. Due to the signal sampling rate, aliasing will occur in the azimuth signals which results in ambiguity. Azimuth ambiguity is quantified with the azimuth ambiguity-to-signal ratio (AASR) and can be calculated [45]. Based on the AASR requirement and system PRF, a side-lobe level (SLL) of 20dB would provide sufficient AASR for good SAR system performance. This value was used as input to the Dolph-Chebyshev synthesis.

The other input for the synthesis is the distance between elements, *d*, which is limited by the following equation:

$$d_{\max} \leq \frac{\lambda}{\pi} \cos^{-1}\left(-\frac{1}{z_0}\right) \tag{4.1}$$

where λ is the wavelength at the operating frequency and z_0 is the Chebyshev polynomial matching variable [2]. Selecting a spacing larger than Eq. (4.1) will result in unwanted grating lobes. The spacing is chosen to be $\lambda_0/2$, which complies with Eq. (4.1). For the 2 x 5 element array, the array factor can be derived as:

$$AF(u) = a_0 + 2a_1 \cos u + 2a_2 \cos 2u \tag{4.2}$$

where

$$u = 2\pi(d/\lambda)\cos\theta \tag{4.3}$$

For $d = \lambda_0 / 2$, $u = \pi \cos \theta$. By comparing Eq. (4.2) with the corresponding Chebyshev polynomial, the normalized array factor equation becomes:

$$AF(u) = 1 + 2(0.8327)\cos u + 2(0.518)\cos 2u \tag{4.4}$$

The antenna factor, $AF(u)$, provides the theoretical beam pattern and is plotted as the dotted line in Figure 4.2. The figure shows that the theoretical side-lobe level is 20 dB below the maximum of the main lobe. Another value of importance in the figure is the beamwidth that is ±11 degrees. This design complies with the narrow azimuth beamwidth requirement.

Table 4.1: Derived Dolph-Chebyshev Array Factors for 2x5 Planar Array

Patch designation	*Array Factor*
Patch (1,1) and (1,2)	0.518
Patch (2,1) and (2,2)	0.8327
Patch (3,1) and (3,2)	1.0
Patch (4,1) and (4,2)	0.8327
Patch (5,1) and (5,2)	0.518

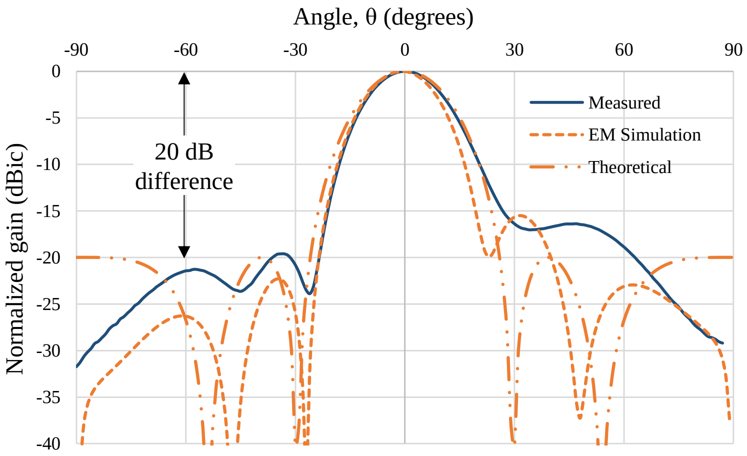

Figure 4.2: Theoretical, simulated and measured normalized antenna beam patterns of the proposed array antenna.

4.1.3 Array signal distribution network

Once the array factors have been derived, these values can be used to design the array signal distribution network. The distribution network will channel energy to each patch at the right magnitude to generate the designed Dolph-Chebyshev beam pattern. A corporate feed network was utilized with lengths kept short and line widths at a low impedance. Most of the embedded microstrip line has an impedance of 35Ω while the network has an input impedance of 50Ω and connected to an SMA connector. The proposed L-band proximity-coupled corner-truncated patch array antenna is shown in Figure 4.3.

Unsymmetrical microstrip T-junctions are used in the feed network to divide the power among the patches according to the array factor in Table 4.1. The geometrical design of the feed is optimized using a method-of-moment based software. After optimization, the array antenna designed shown in Figure 4.3 was fabricated with the dimensions listed in Table 4.2. In total, four arrays were manufactured for measurement and use in the SAR system; two units of left-handed circularly polarized (LHCP) and two units of right-handed circularly polarized (RHCP).

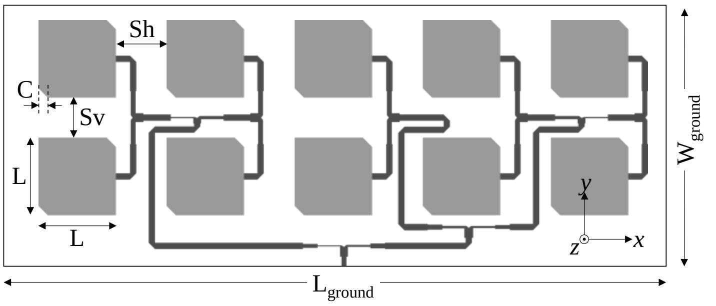

(a) Top view

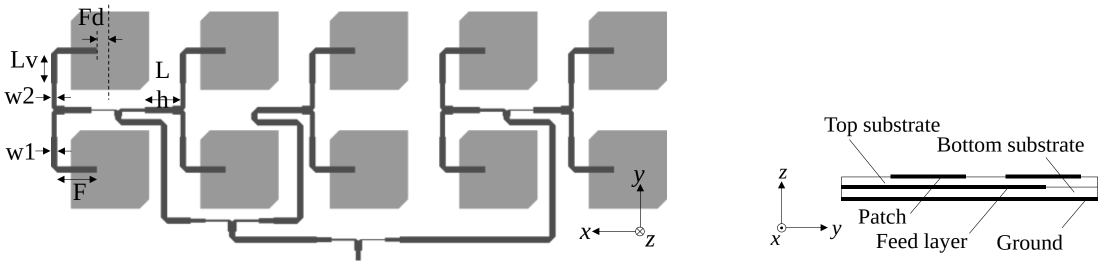

(b) Feed network, viewed from bottom

(c) Side view

Figure 4.3: Dimensions of the proposed side-lobe reduced array antenna.

Table 4.2: Proposed Array Antenna Dimensions

Parameter	*Size (mm)*	*Parameter*	*Size (mm)*
L	79.18	Sv	50.0
C	9.0	R	24.0
Fd	14.0	w1	6.8
F, Lh	40.0	w2	5.0
Lv	38.0	Lground	655.0
Sh	54.0	Wground	285.0

4.1.4 Simulated and Measured Results

A fabricated LHCP array antenna is shown in Figure 4.4. The antenna's reflection coefficient and radiation pattern were measured in an anechoic chamber and compared to simulated performance. In Figure 4.5, the reflection coefficient shows good agreement between simulation and measured values. The impedance bandwidth achieved is 58 MHz with a minimum reflection coefficient of -20 dB at around the center operating frequency. At maximum bandwidth, the antennas can function at frequencies from 1.241 to 1.299 GHz. The realized center frequency is slightly higher most probably due to errors in fabrication of the radiating patch size.

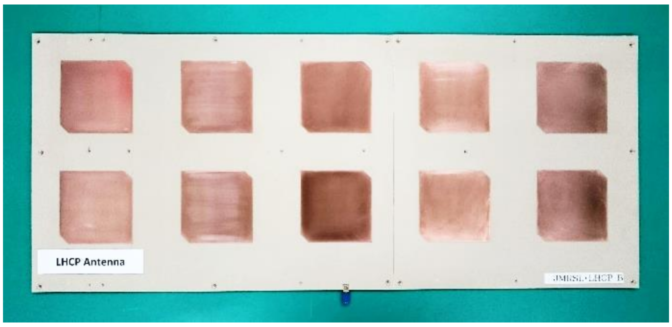

(a) Radiating layer

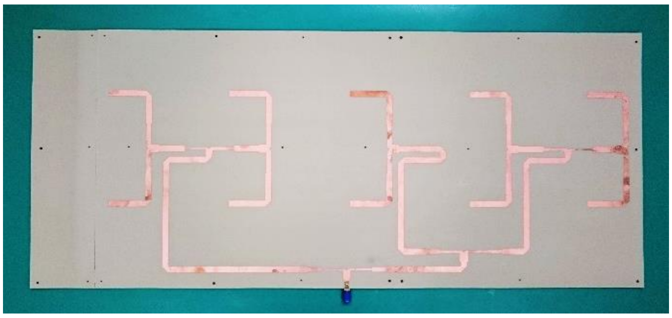

(b) Feed network layer

Figure 4.4: The top and bottom layers of the LHCP fabricated array.

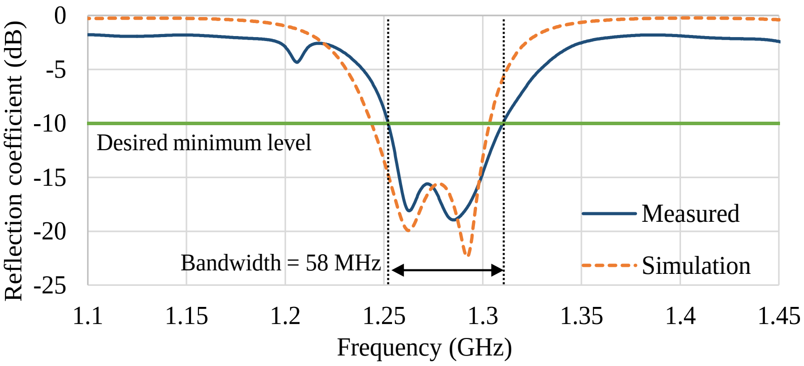

Figure 4.5: Simulated and measured reflection coefficient of the RHCP array antenna.

The radiation pattern in Figure 4.2 shows the measured side-lobe level to the left of the main lobe to be –20 dB. This matches the theoretical and simulated levels. However on the right of the main lobe the side-lobe levels are not as low. This can be attributed to the feed design. From the feed designs seen in Figure 4.3(a) and Figure 4.5(b), there are more microstrip lines on the right side. These will contribute to spurious radiation. Figure 4.6 shows the lopsided beam pattern on a polar graph.

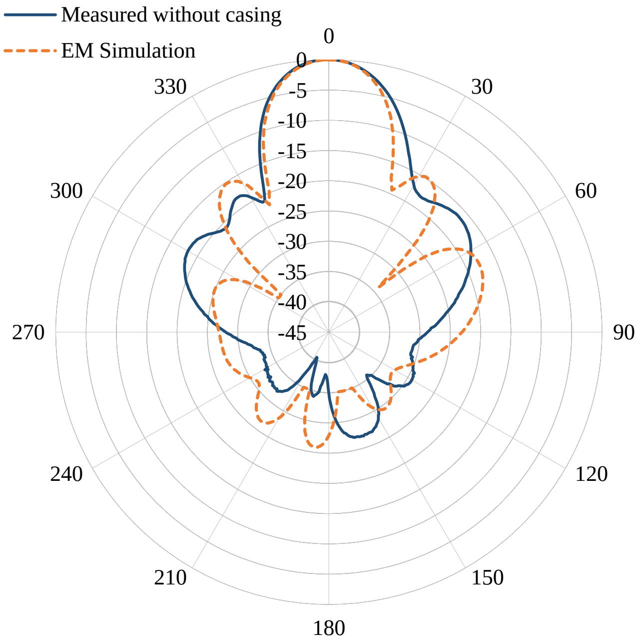

Figure 4.6: Simulated and measured radiation pattern of the RHCP array antenna.

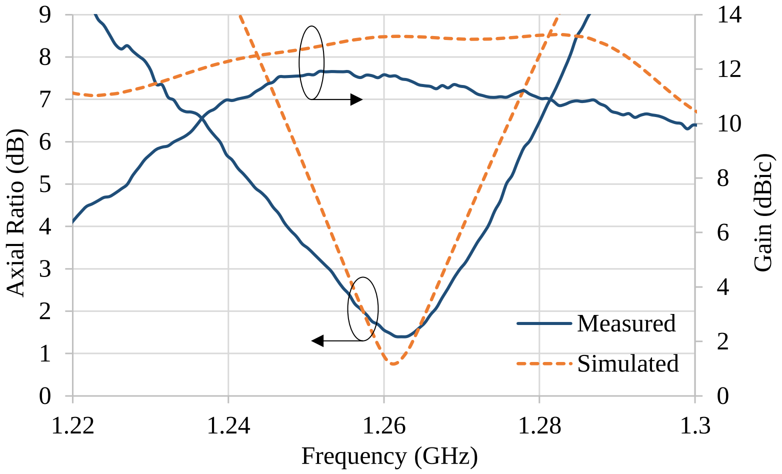

Figure 4.7: RHCP array antenna simulated and measured axial ratio and gain against frequency.

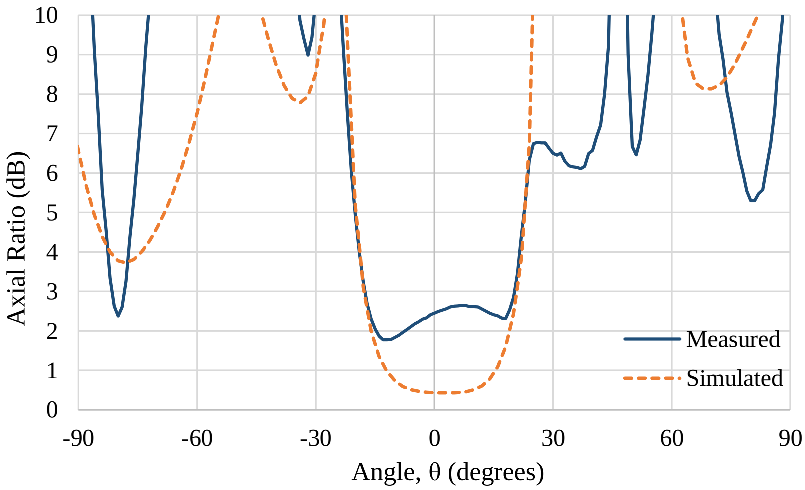

Figure 4.8: RHCP array antenna simulated and measured axial ratio against angle.

The simulated and measured AR and gain against frequency is plotted in Figure 4.7, showing the measured gain is 10.0–11.9 dBic from 1.241 to 1.299 GHz. The 3-dB AR bandwidth achieved at the direction of θ = 0° (i.e., the AUT is set perpendicular to the standard antenna during parameter measurement) is about 17 MHz, which corresponds to 1.36% of the operation frequency of 1.27 GHz. In the simulation, on the other hand, the value is 13 MHz, or around 1.00% of the operation frequency. The minimum axial ratio of the measured data is around 1.40 dB, exhibiting a difference of around 0.64 dB as compared with the simulation result. Inaccuracies in the implementation of the corner-truncated patches are one possible cause of differences between the simulated and measured results. As explained in Section 4.1.1, the truncation size greatly effects the axial ratio. Displaying AR against angle in Figure 4.8 shows that the designed array antenna has a measured axial ratio of <3 dB for +-20 degrees from main beam.

4.2 Beam tilted Circularly Polarized Array Antenna

In this section, a circularly polarized antenna array employing beam tilting as well as side-lobe reduction using the Dolph-Chebyshev synthesis method at C-band 5.3 GHz is presented. The antenna developed in this work is to be used in an airborne SAR system. Comparatively to spaceborne systems, airborne SAR operates at a much lower altitude and thus has a different set of operating parameters such as shorter range, and a lower average transmit power. In our case the SAR range is around 15 km with an average transmit power of around 50 watts based on a previous study [46]. The travelling speed is also much slower thus the pulse repetition frequency (PRF) requirement is lower.

The antenna performance requirements were provided from the initial SAR system study and used as a starting guideline. The SAR system is to be operated on a Boeing 737-200 aircraft with the antenna mounted on a location above the fuselage, between the front wings and rear stabilizers as shown in Figure 4.9. To reduce power loss it is desired that the transmission line lengths be minimized. As such, the SAR system processor and data logging are installed in a working compartment at the rear of the aircraft fuselage, while the RF front-end (transceiver module) is located in the radome with the antenna. Connection between the RF front-end and the antennas is made with minimal use of semi-rigid cables.

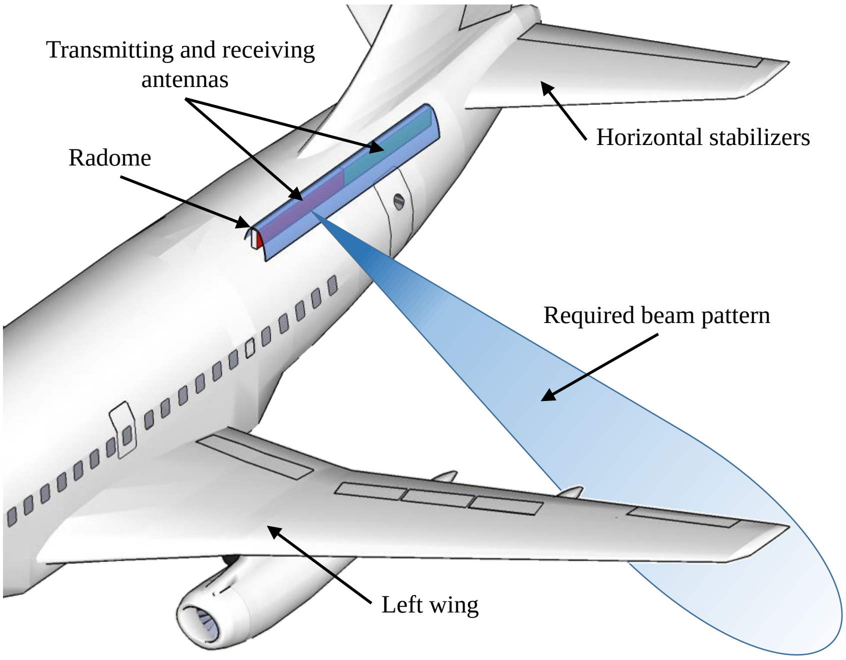

Figure 4.9: Location of antennas and required beam pattern path.

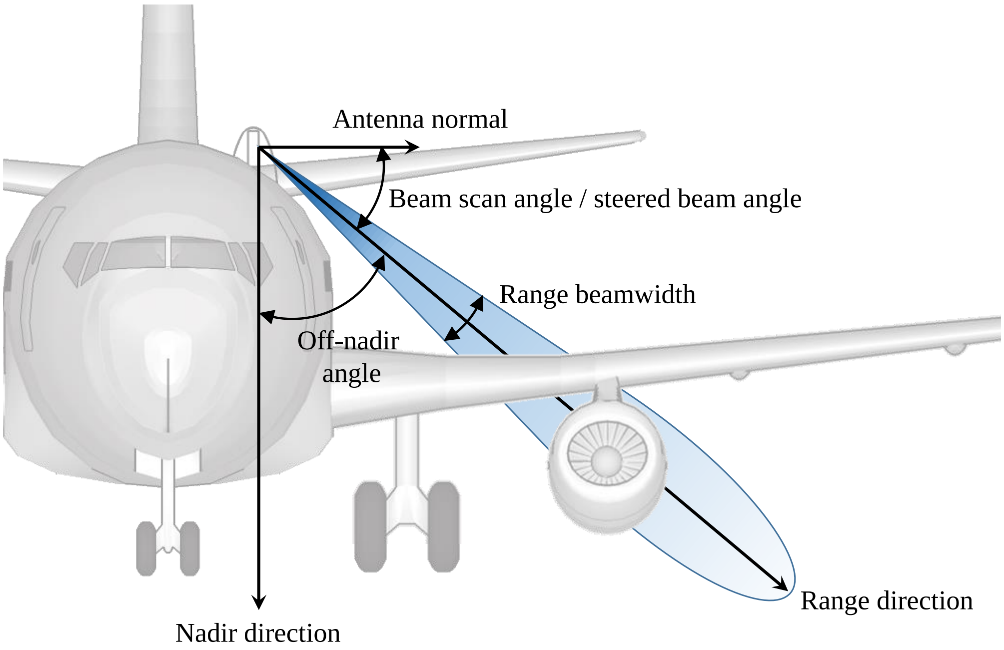

Figure 4.10: Profile of desired antenna beam pattern.

Considering the antenna radiation pattern design factors for airborne SAR [47], an azimuth ambiguity over signal ratio (AASR) and side-lobe level (SLL) of -20 dB was selected for acceptable SAR performance. Range ambiguity is caused by scattering received from earlier or later pulses arriving back to the antenna at the same time as the desired echo. Taking into account the SAR design constraints above and the vertical mounting orientation of the antenna shown in Figure 4.10, the vertical and horizontal plane radiation patterns are designed. For the vertical plane, a 3-dB beam-width of 11 degrees and a beam shift angle of 40 degrees from the antenna normal is required.

For full polarimetric measurements a total of four antennas will be required; two left hand-polarized and two right-hand polarized. As an operational example, if a left-handed antenna is transmitting, a different left-handed antenna and a right-handed antenna will receive the backscattered signal. The receiving-transmitting pair notations are listed in Table 4.3. The antennas are marked on the right side of the RF system diagram in Figure 4.11. Each back-scattered radar signal is digitized in the real and imaginary format, and saved for SAR image generation during post processing.

Table 4.3: Circular polarization (left/right-handed) notation for receive and transmit antennas.

Receive	*Transmit*	*Notation*
Left	Left	LL
Right	Right	RR
Right	Left	RL
Left	Right	LR

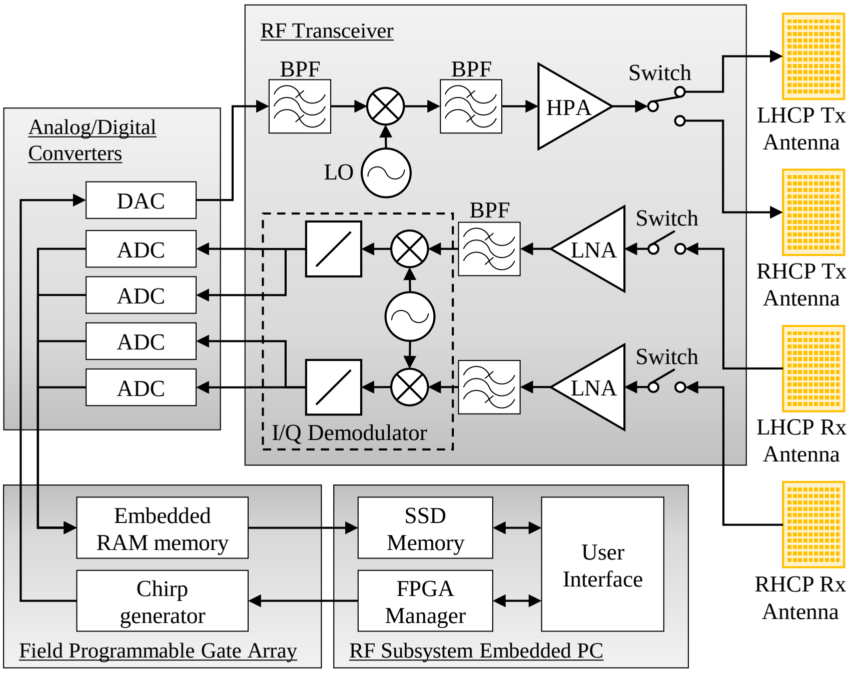

Figure 4.11: RF system diagram.

The radiation pattern requirements can be achieved with a planar microstrip patch array. The patch array design process begins with designing a single patch element to comply with the operating frequency and circular polarization performance requirements. The single element patch is repeated multiple times in a row with uniform spacing to form a linear array. Antenna synthesis was performed to reduce side-lobe levels typically generated by uniform arrays. To conform to the look angle of the SAR system, a 40 degree scanning angle was applied. Finally, with the designed parameters, the feed network consisting of power splitters/combiners and transformers was designed. Each step of the array design is explained in further detail in the following subsections. Ten elements were used to generate the vertical plane pattern, whilst 12 elements were required for the horizontal-plane, resulting in a 120-element array.

4.2.1 Single element design

An electromagnetically coupled square patch was used as the radiating element because a wider impedance bandwidth is desired. The structure contains two substrates with the same dielectric constant. The radiating patch is on the top, the feed line in between the two substrates, and the ground layer is at the bottom. With this structure spurious radiation is also reduced as the feed line is located closer to the ground plane. A combined thicker substrate between the radiating patch and ground plane also provides improved impedance bandwidth over the conventional microstrip-fed patch [2], [48].

Geometry design of the single patch is presented in Figure 4.12. Two identical layers of Nippon Pillar substrate was used, each with 1.6 mm thickness, relative permittivity of 2.85 and loss tangent of 0.0024. Patch dimensions of 15.54×15.54mm results in a center operating frequency of 5.3GHz. The feed line, w2, has a width of 2.533 mm for an impedance of 50Ω and a length of 26.813mm or 3λ/4 to have the current peak at the radiator. The feed width under the radiator, w1, is 3.822 mm for an impedance of 39.95Ω. A quarter-wave transformer was used to match the impedances of the single patch feed.

For circular polarization, truncations were made at two opposing corners to excite the two orthogonal modes simultaneously with a 90 degree time-phase difference. Axial ratio was calculated as a measure of circular polarization. As shown in Figure 4.13, varying the truncation length changes the axial ratio value. Axial ratio values under 3-dB is considered to be circularly polarized. Optimizing the length to 22% of the patch length, the axial ratio was minimized.

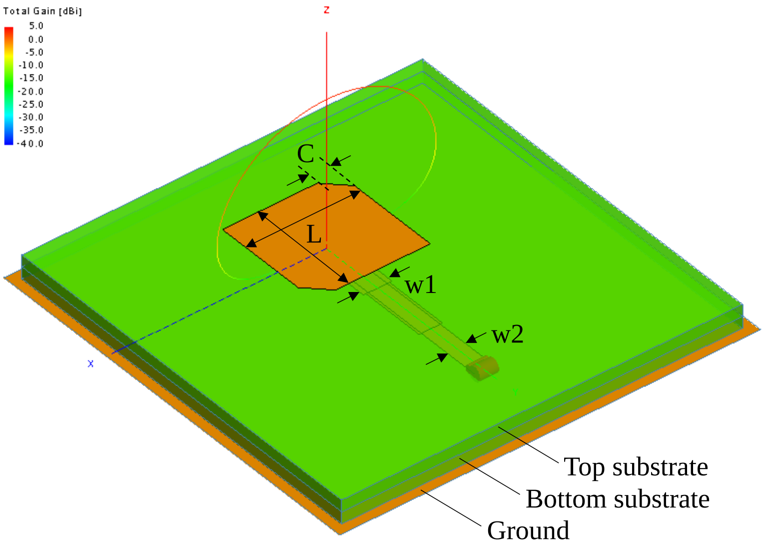

Figure 4.12: Single element corner truncated patch antenna on dual substrates. Also shown is the radiation pattern that peaks at 5 dBi at the boresight.

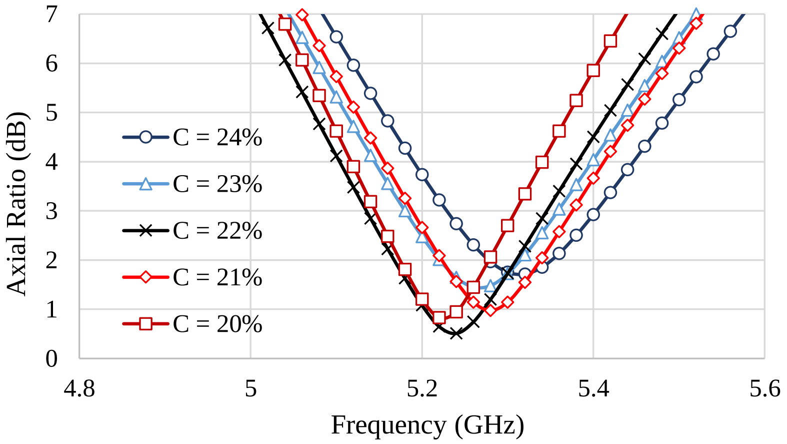

Figure 4.13: Axial ratio values as a function of the truncation size. The truncation size is shown as a percentage of the patch width.

4.2.2 Steered beam design

Based on the design requirements, the antenna main beam needs to be steered to ideally 40 degrees due to the vertical mounting of the antenna on the aircraft. A phased-shifted linear array structure was adopted as it is simple to implement. The only disadvantage of this structure is the beam steer is fixed, however in our implementation there is no need for digital beamforming.

The phase increment, $\Delta\varphi$, between each successive element is calculated using equation (1), where *d* is the distance between the individual patches, Θ_s is the steer angle, and lambda is the system wavelength [49].

$$\Delta\varphi = \frac{360° \cdot d \cdot \sin\Theta_s}{\lambda} \tag{4.5}$$

The value of *d* cannot be too large to avoid unwanted grating lobes. The value of *d* was selected to be 0.53λ. Ideally a 45 degree steer was required by the system design. However through the design iteration process only a 40 degree steer was achieved as steering even further will result in reduced side-lobe level and degraded performance. The calculated phase delay for each patch element is shown in Table 4.4. Phase delays are implemented using carefully sized microstrip lines which will be explained in Section 4.2.4.

4.2.3 Design of reduced side-lobe

A linear array with uniform power division typically results in good gain in the main lobe, but also large side-lobe levels which can add to cross-range ambiguity in the SAR processing. To further reduce the signal-to-noise ambiguity, the radiation pattern side-lobes were reduced by utilizing the Dolph- Chebyshev synthesis method to find the array factor for each element.

To reduce the side-lobe levels the Dolph-Chebyshev synthesis method was utilized with satisfying results. The array consists of 10 elements arranged linearly with spacing between each element set to 0.53λ. Based on AASR requirement and system PRF, a side-lobe level of -20dB would provide sufficient AASR for good SAR system performance. This value was used as input to the Dolph-Chebyshev synthesis. The synthesis output for each antenna element is shown as array excitation coefficients in Table 4.4. The array consists of 10 elements arranged linearly with equal spacing, *d*, between each element. Based on AASR requirement and system PRF, a side-lobe level of -20dB would provide sufficient AASR for good SAR system performance. This value was used as input to the Dolph-Chebyshev synthesis using the array factor equation below [2].

$$(AF)_{2N} = \sum_{n=1}^{N=5} w_n \cos\left[(2n-1)u\right] \tag{4.6}$$

$$u = \frac{\pi d}{\lambda}\cos\theta \tag{4.7}$$

Where w_n is the excitation coefficients of each array element. Solving the above equations with the cosine series expansion, the array factor equation becomes:

$$(AF)_{10} = 0.15\cos u + 0.133\cos 3u + 0.103\cos 5u + 0.069\cos 7u + 0.045\cos 9u \tag{4.8}$$

The synthesis output for each antenna element is shown as array excitation coefficients in Table 4.4. As a comparison, Figure 4.14 shows the simulated radiation patterns of the designed array with and without the synthesized array factors. Note the drop in side-lobe magnitude as well as expansion of the beam-width compared to the un-synthesized radiation pattern. The reduction of the side-lobe is important for improving range and cross-range ambiguity during image construction of the synthetic aperture radar.

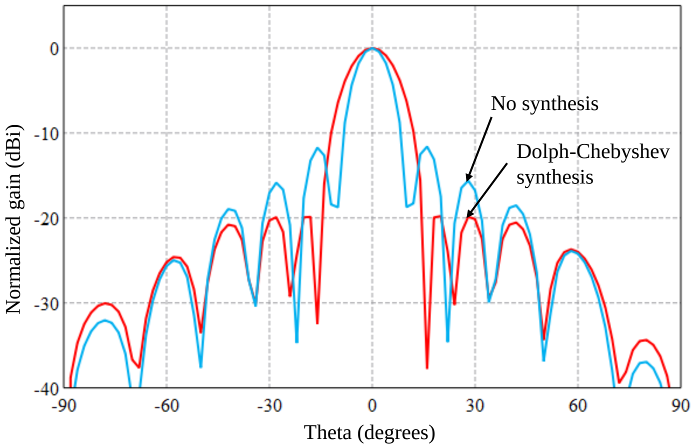

Figure 4.14: Comparison of a 10-element radiation pattern with and without the proposed synthesis method.

Table 4.4: Derived excitation coefficients and phase delay for each patch element.

Element	1	2	3	4	5	6	7	8	9	10
Relative amplitude	0.045	0.069	0.103	0.133	0.150	0.150	0.133	0.103	0.069	0.045
Phase (degree)	0	135	270	405	540	675	810	945	1080	1215
Phase (lambda)	0	0.375	0.750	1.125	1.50	1.875	2.250	2.625	3.00	3.375
Distance from feed (mm)	117.4	130.2	143.0	155.8	168.6	181.4	194.2	207.0	219.8	232.6

4.2.4 Array Signal Distribution Network

Once the phased shift angle and array factors have been derived, these values can be used to design the array signal distribution network. The distribution network will channel energy to each patch at the right time and magnitude to generate the designed beam pattern. A corporate feed network was utilized with lengths kept short and line widths narrow to minimize spurious radiation [48]. The network has an input impedance of 50Ω while most of the microstrip line has an impedance of 67Ω.

To implement the steered beam of Section 4.2.2, the phased shifted network was designed by delaying the signal to each subsequent element. The simplest way to achieve this is to increase the distance travelled by the signal. This method of delayed power feed is a form of constrained feeding. Each patch will be fed with a signal that is delayed by a phase of $\Delta\varphi$ degrees, or a length of d_φ, as calculated from:

$$d_\varphi = \frac{\Delta\varphi}{360^\circ}\times d_\lambda \tag{4.9}$$

Where d_λ is the electrical length the microstrip line at the center operating frequency when using the specified substrates. This electrical length can be estimated through calculations but it is found that EM simulation results provided values closer to the actual length.

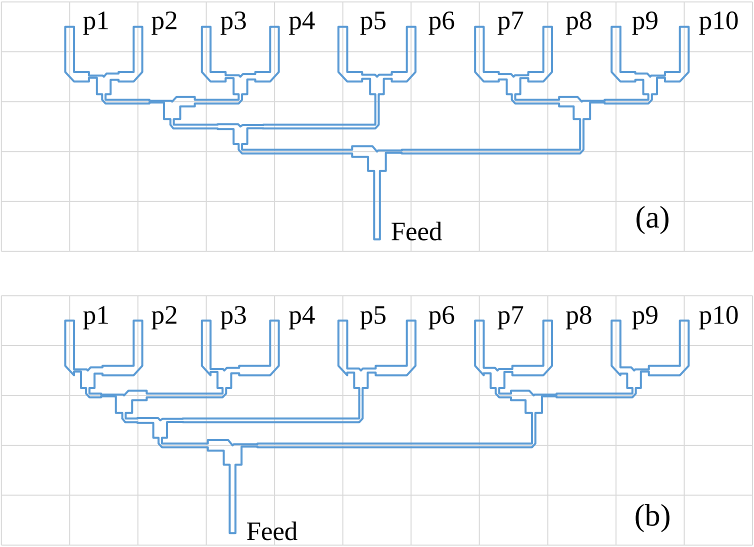

Figure 4.15: Design of microstrip feed network with synthesized power distribution: (a) Zero degree beam steer; (b) 40-degree beam steer. Note the shifted lengths of the microstrip lines.

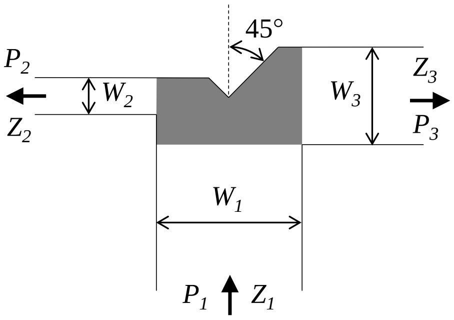

Figure 4.16: Unsymmetrical microstrip T-junction design.

With the calculated feed delay lengths for each element, the feed network for beam steering is designed as shown in Figure 4.15(b). As compared to the feed network with no phase delay in Figure 4.15(a), the phase delayed network has a feed microstrip lines that are shifted to one side. This will affect the radiation beam pattern slightly.

To implement the reduced side-lobe of Section 4.2.3, unsymmetrical microstrip T-junction power dividers [50] were used in the feed network to divide the power to each patch according to the calculated array factors. Figure 4.16 shows a modified unsymmetrical T-junction with a v-notch to improve power division. Each T-junction is sized specifically using (4.10) to match the final output requirement at the individual patches.

$$Z_1 = \frac{Z_2 \times Z_3}{Z_2 + Z_3}, \; P_2 = \left(\frac{Z_1}{Z_2}\right) P_1, \; P_3 = \left(\frac{Z_1}{Z_3}\right) P_1 \tag{4.10}$$

The calculated impedances, Z_n, for each power divider would have a specific line width, W_n, when implemented as an embedded microstrip. The respective line widths can be calculated by solving for W in the following equations:

$$Z = \frac{60}{\sqrt{\varepsilon_e}} \ln\left(\frac{5.98h}{0.8W + t}\right) \tag{4.11}$$

$$\varepsilon_e = \varepsilon_r \left(1 - \exp\left(-1.55 \frac{h_1}{h}\right)\right) \tag{4.12}$$

Where h is the dielectric thickness, h_1 is the total thickness of both substrates, t is the trace thickness, ε_r is the relative dielectric constant, ε_e is the effective dielectric constant, and Z is the required impedance.

With the phase delay lengths and T-junction power dividers calculated and sized, the geometry of the 1x10 beam steered antenna is drawn and presented in Figure 4.17(a). The figure shows the patch width and length, *L*, the corner truncation size, *C*, the distance between antenna elements, *d*, and the ground plane size. The bottom view of the designed array clearly showing the phase shifted, power distributed feed network is shown in Figure 4.17(b). The various substrate and copper layers are shown in Figure 4.17(c).

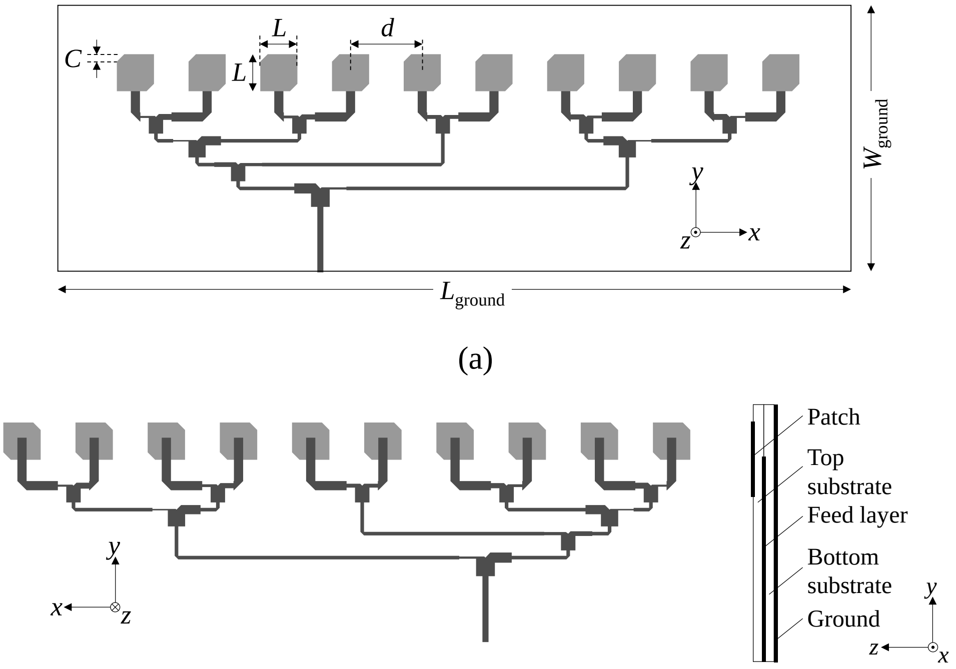

(a)

(b) (c)

Figure 4.17: Geometry of left-handed circularly polarized array antenna: (a) top view (light gray is radiating patch, dark gray is the feed network); (b) bottom view; and (c) side view.

4.2.5 Simulated and measured results

The proposed 10×1 element array antenna was studied using the FEKO electromagnetic simulation software. The simulation process starts with designing a balanced feed with no delay lines and uniform power distribution. The scattering parameters at the output to each element was observed to confirm that the feed has equal phase and power. Next, feed lines were introduced to apply beam steering, followed by unsymmetrical T-junction power dividers. The scattering parameters were observed and confirmed at each step, making adjustments to the calculated input if necessary. To complete the 10×1 element array, the optimized radiating patch was applied. The full model was then simulated for return loss, axial ratio, input impedance, and far field radiation patterns. Using the finalized design, the beam steered, synthesized 10×1 element array was fabricated and a left-handed CP prototype is shown in Figure 4.18. The fabricated array antenna performance parameters were then measured to confirm agreement with the simulated results.

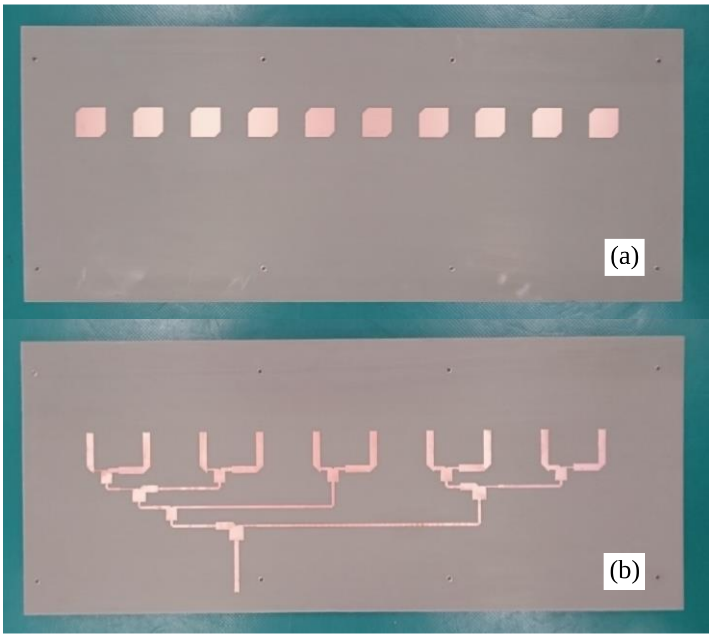

Figure 4.18: Prototyped left-handed circularly polarized array antenna: (a) top substrate; (b) bottom substrate.

4.2.5.1 Beam steered, synthesized 10×1 array

Beam steering at varying angles were studied to determine the maximum angle possible with the designed feed network. Figure 4.19 is a polar diagram showing the radiation pattern magnitudes of several notable angles. As expected, the main lobe is straight into the +z-direction when no steer is implemented. It is interesting to note that the gain increases slightly when the beam is steered above 15 degrees. The raised gain is maintained until around 40 degrees, after which there is a sharp decline in gain. This is due to the appearance of grating lobes on the opposite side of the array. Magnitudes of other side-lobes also increase above 40 degrees. At beam steer angles larger than 41 degrees, the T-junctions closest to the first element will not have enough space and a total redesign of the feed will be required. As such the maximum beam steer angle limit is 40 degrees.

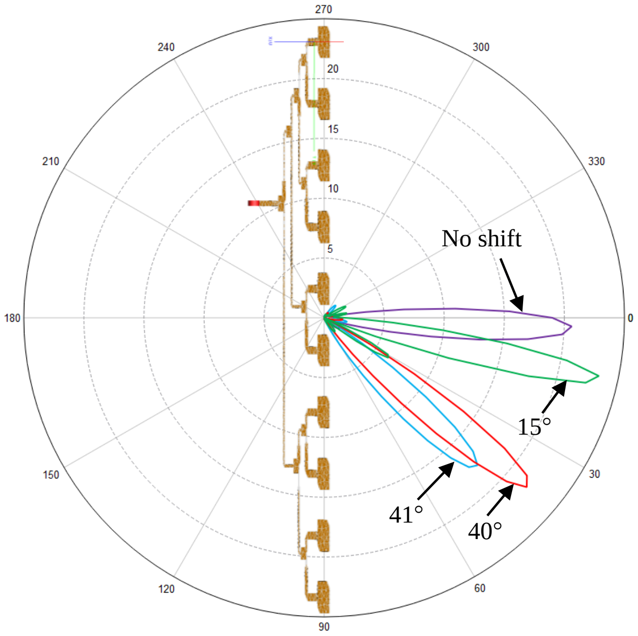

Figure 4.19: Magnitude and beam steering at different angles.
40 degrees provides the best compromise of steer angle and gain

Once the desired beam steer is achieved, a full 3D radiation pattern was simulated to ensure no excessive spurious radiations occur. The simulated 3D radiation pattern in decibel and magnitude scales are shown in Figure 4.20. The side-lobe in the +z-direction is the largest and several side-lobes are found to be slightly above the designed –20dB side-lobe level requirement.

After optimization in the software, the designed array antenna was fabricated in-house using chemical etching. Both radiating patch and feed network layers of the fabricated antenna are shown separately in Figure 4.18. Scattering parameters were taken using a vector network analyzer and far field radiation patterns were measured in the anechoic chamber.

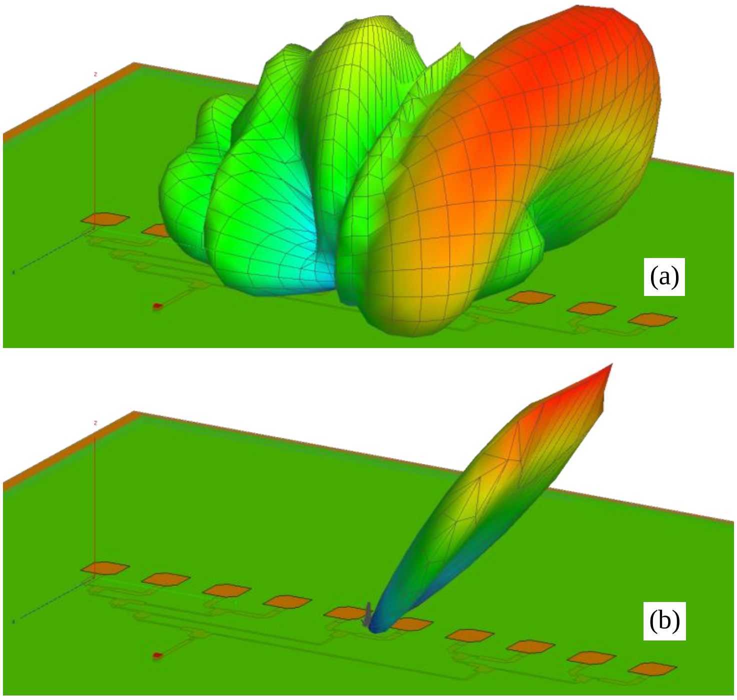

Figure 4.20: Simulated 3D radiation pattern at 40 degree beam tilt: (a) decibel scale; (b) magnitude scale.

The measured and simulated return losses of the proposed array antenna in Figure 4.21 show good agreement. The realized bandwidth is 215 MHz (4.1%) from 5.157 GHz to 5.39 GHz at a center frequency of 5.2825 GHz, which matches the 215 MHz (4.0%) simulated bandwidth but at a slightly different frequency range from 5.165 GHz to 5.38 GHz with a center frequency of 5.2725 GHz.

A far field frequency sweep was measured between the proposed antenna and a set of left and right-handed CP spiral cone antennas to calculate the gain and axial ratio. Angle of measurement had to be properly planned as the beam steering must be taken into account. An axial ratio of 125MHz or 2.43% (5.085–5.210GHz) seen in Figure 4.22 was measured at the 40 degree boresight angle. Simulated axial ratio was slightly less at 120 MHz or 2.30% (5.155–5.275GHz). The measured gain plot must be compared to an isotropic antenna gain to calculate the realized gain [37]. A 5.3 GHz dipole antenna was measured and its peak gain was used as the isotropic gain value. The realized left-handed gain was calculated and the graph has some agreement with the simulated results as also shown in Figure 4.22. The peak left-handed CP gain was measured at 12.1 dBiC, slightly lower than the simulated gain of 12.7 dBiC. The differences between simulated and measured values can be attributed to manufacturing imperfections.

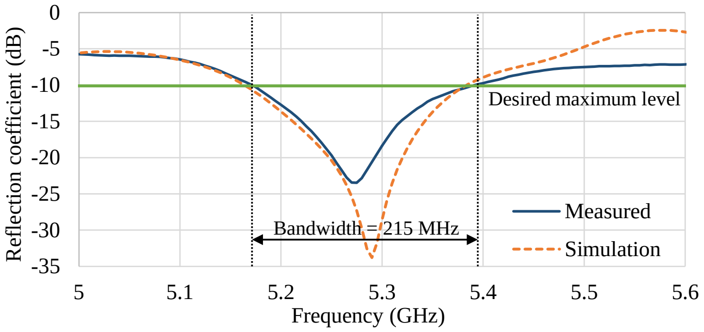

Figure 4.21: Measured and simulated return losses of the proposed array antenna.

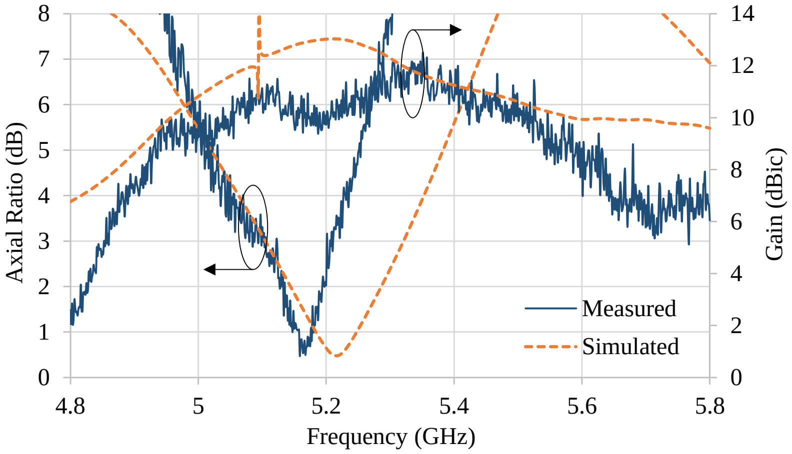

Figure 4.22: Measured and simulated axial ratio of the proposed array antenna.

Lastly, an angular sweep was performed to obtain the array radiation pattern at the designed operating frequency of 5.3GHz. The proposed antenna was placed on a rotary turntable and measured in the far field with standardized CP antennas. The measured and simulated left-handed radiation patterns are shown together in Figure 4.23. Simulation was performed on an infinite substrate, thus there is no radiation below the ground layer as shown by the dotted line plot. There is good agreement between the radiating sides of the two plots. However in terms of side-lobe performance, and as noted before, the side-lobe levels did not conform to the -20dB requirement. The measured radiation pattern shows a side-lobe level of -15dB which is still an improvement of over 5dB compared to an un-synthesized feed network. The beam steer was successfully implemented as the main lobe is clearly directed in the 40 degree direction, with a half-power (3-dB) beam-width of 11.5 degrees.

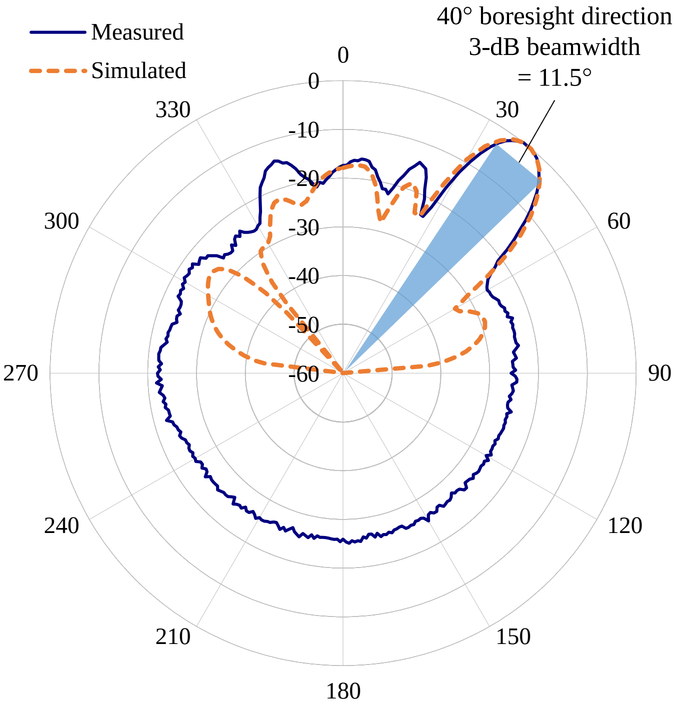

Figure 4.23: Measured and simulated radiation pattern of the designed left-handed circularly polarized array. Simulated maximum gain is 12.7 dBiC, measured gain is 12.1 dBiC.

4.2.5.2 Array module to achieve target gain

A study into the design of a suppressed side-lobe, beam-steered, CP 10×1 element array antenna was completed. The design procedures resulted in a fabricated antenna that matched the simulation results. However, the single linear array with 10×1 elements was not sufficient to generate the required minimum gain of 17 dBiC. To reach this requirement, a larger planar array has to be designed. A modular structure is adopted for ease of mounting, transport and increasing the gain if required.

Figure 4.24 presents the proposed three layer substrate array module structure. The radiating patches in the top substrate is the same as designed in this study. The feed network of the middle layer will also contain the designed phase delays and power distribution for steered beam and reduced side-lobes. The additional layer at the bottom will have via probes connecting to an unbalanced 3-way Wilkinson power divider. This power divider will perform the same function as the first stage divider of the linear array design, but with greater efficiency. Each module would contain 10×4 elements to generate 18 to 19 dBiC of gain which complies with the minimum system gain requirement.

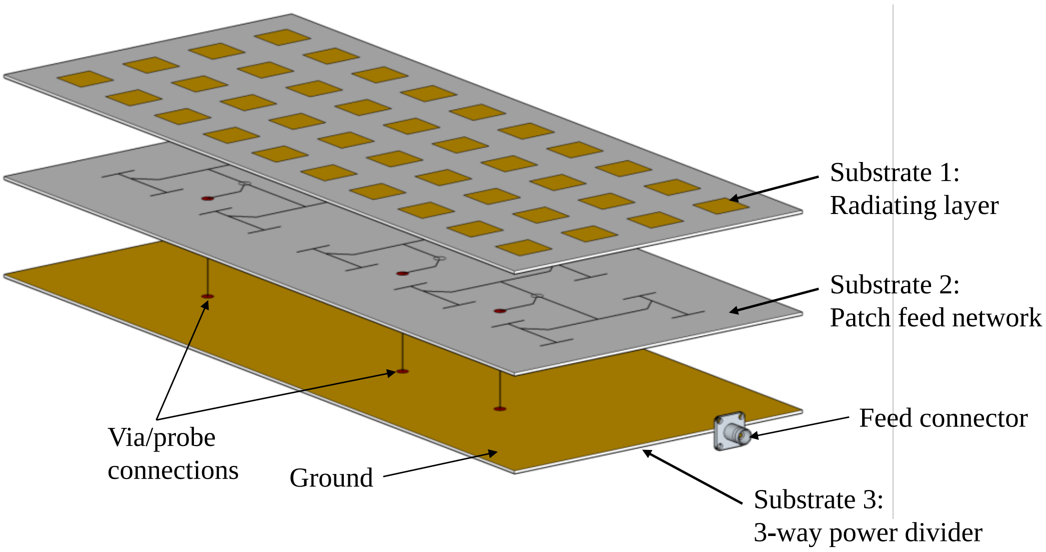

Figure 4.24: Proposed array module structure. From top: radiating patch, feed network, and 3-way power divider layers.

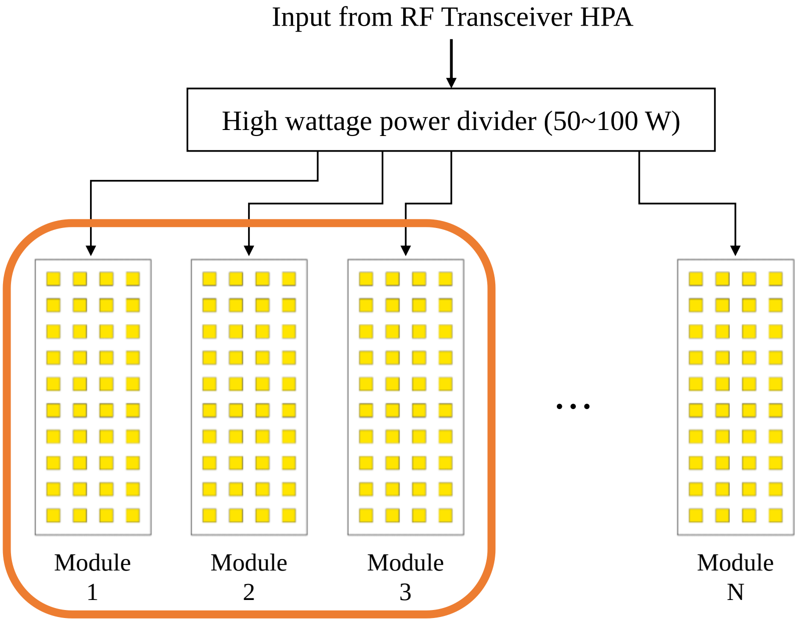

Figure 4.25: With a high wattage power divider, use of multiple modules can increase the total system gain as required.

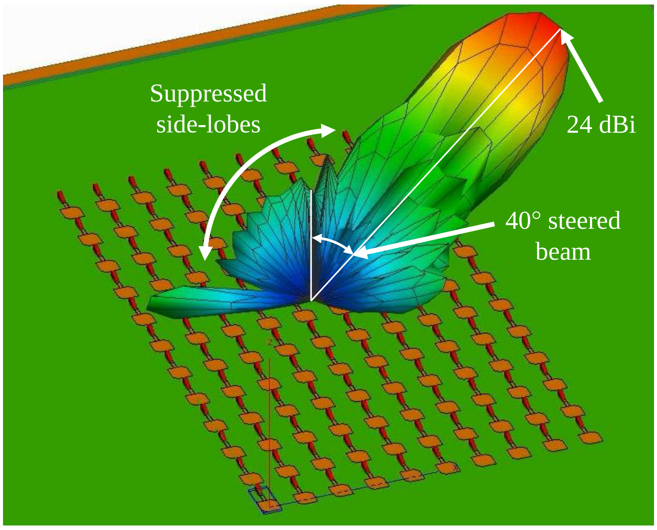

Figure 4.26: Simulated 3D radiation pattern of a 10×12 element array achieved by utilizing three antenna modules.

If higher gains are required, additional modules can be added. For example as shown in Figure 4.25, three modules can achieve a gain between 21-24 dBiC. Figure 4.26 shows the radiation pattern generated by a 10×12 element array consisting of three of the proposed modules for a total of 120-elements. The boresight is still steered by 40 degrees and side-lobes are suppressed to between -15 dB and -20 dB. The vertical plane 3-dB beam-width is 11.5 degrees, the same as the 10×1 array. Meanwhile, the horizontal plane 3-dB beam-width is 5 degrees.

A simple corner truncated square patch was used as elements in a beam steered array. By using a corporate feed structure with unsymmetrical T-junctions and varying feed line lengths, a side-lobe level of -15 dB and high beam steer angle of 40 degrees is achieved. The power to each patch is distributed using a Dolph-Chebyshev synthesis to reduce the side-lobes. The designed 10-element array was simulated and fabricated after optimization. The fabricated prototype achieved a circular polarized bandwidth of 125 MHz or 2.43% (5.085 – 5.210 GHz) and impedance bandwidth of 215 MHz or 4.1% (5.157 – 5.39 GHz) was achieved. An antenna peak gain of 12.1 dBiC was realized with a half-power beam-width of 11.5 degrees. With the achieved performance parameters of the prototype, a set of the proposed array antenna is suitable for use as transmit and receive antennas in the planned airborne circularly polarized synthetic aperture radar system. To increase the gain, a planar array structure was proposed with simulated results showing compliance depending on the SAR system gain requirements. The modular structure makes it easier to customize the antenna size to different missions.

Chapter 5 INTEGRATED SAR SYSTEM

With the knowledge obtained from preliminary SAR measurements using the SAR testbed developed in Chapter 3, and fabrication of custom circularly polarized patch array antennas in Chapter 4, the next step is to integrate both developments into a single SAR system. Before we proceed, a brief explanation on the theoretical scattering of circular polarization signals is required.

5.1 Circular Polarization Scattering Matrix

In the following two equations we used the Sinclair scattering matrix, ***S***, to express the polarimetric signature of the flat plate target. Matrices for other canonical targets is documented in [51].

LP Cartesian polarization basis (H, V) for flat plate:

$$S_{linear} = \begin{bmatrix} S_{HH} & S_{HV} \\ S_{VH} & S_{VV} \end{bmatrix} = \begin{bmatrix} 1 & 0 \\ 0 & 1 \end{bmatrix} \tag{5.1}$$

CP Cartesian polarization basis (L, R) for flat plate:

$$S_{circular} = \begin{bmatrix} S_{LL} & S_{LR} \\ S_{RL} & S_{RR} \end{bmatrix} = \begin{bmatrix} 0 & j \\ j & 0 \end{bmatrix} \tag{5.2}$$

Cartesian polarization basis (H, V) is the LP response where H stands for horizontal polarization and V for vertical. On the other hand, Cartesian polarization basis (L, R) is the CP response where L is for left-handed circularly polarized (LHCP) and R is for right-handed (RHCP). Table 5.1 summarizes the scattering matrices for flat plate, dihedral and thin vertical pole reflectors, for linear and circular polarizations.

Table 5.1: Linear and circular polarization basis scattering matrices for canonical targets used in experiments.

Cartesian polarization basis, ***S***	Flat plate reflector	Dihedral reflector	Thin vertical pole
$S_{linear} = \begin{bmatrix} S_{HH} & S_{HV} \\ S_{VH} & S_{VV} \end{bmatrix}$	$\begin{bmatrix} 1 & 0 \\ 0 & 1 \end{bmatrix}$	$\begin{bmatrix} 1 & 0 \\ 0 & -1 \end{bmatrix}$	$\begin{bmatrix} 0 & 0 \\ 0 & 1 \end{bmatrix}$
$S_{circular} = \begin{bmatrix} S_{LL} & S_{LR} \\ S_{RL} & S_{RR} \end{bmatrix}$	$\begin{bmatrix} 0 & j \\ j & 0 \end{bmatrix}$	$\begin{bmatrix} 1 & 0 \\ 0 & -1 \end{bmatrix}$	$\frac{1}{2}\begin{bmatrix} 1 & -j \\ -j & 1 \end{bmatrix}$

5.2 Linear Rail SAR

Four sets of the circularly polarized array antenna were fabricated and used together with the linear rail system explained in Chapter 3. The aim of this experiment is to verify the functionality of the antennas with the developed SAR measurement system, and study the circular polarization characteristics on different reflectors. Due to difficulties in preparing an outdoor experiment and regulatory requirements on transmitting and receiving high powered RF signals, the experiment had to be made indoors. In hindsight this was the better condition as we have since developed a completely new configurable SAR measurement scheme for the laboratory.

A three meter long track was placed along the azimuth synthetic aperture length, L_{sa}, in an anechoic chamber as the arrangement in Figure 2.2. Since the chamber is small, the antennas will be static while the reflector will move along the azimuth. This setup is similar to inverse SAR [9]. An aluminum plate was used as a point target reflector and is placed at a range distance, r_0, from the radar on a moveable platform on the track. Besides triggering the RF front-end, the embedded computer in the SAR measurement system is assigned an additional function to control the moving platform. All antennas and reflectors were placed at the same height from the ground. The installed antennas and reflector is shown in Figure 5.1. Measurements are performed in four setups of co-polarization (LL, RR) and cross-polarizations (LR, RL) as listed in Table 4.3. For example, a cross-polarization measurement at any one time may utilize a right-handed transmit antenna, and a left-handed receive antenna (RL measurement).

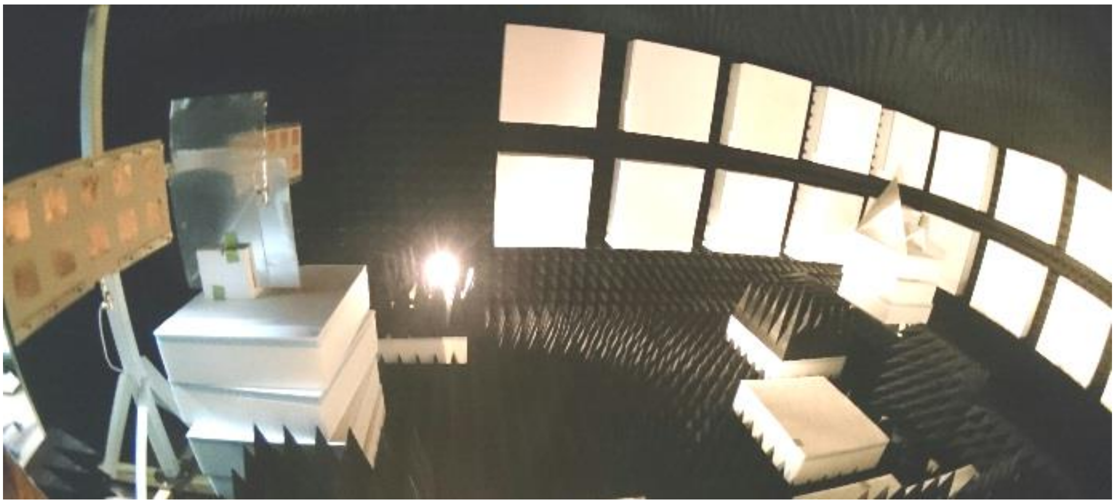

Figure 5.1: The reduced side-lobe antennas installed on the mounting on the left and corner reflector placed on the moving platform on the far right of the image.

The side length of the plate should ideally be 10 times the signal wavelength [43]. Since the operating frequency is 1.27 GHz the reflector should have a size of 2.5 meters on each side. This is prohibitively difficult, thus a 900 x 600 mm sized aluminum plate was used instead. This will result in a much smaller point target reflection intensity value due to a reduced radar cross section. As the test is performed in an anechoic chamber, there will not be much backscatter from the environment.

In this test the stop-and-go method is used to capture backscattered data along the azimuth. The platform moves along a high precision track at 50 mm per interval for a total of 51 points along the azimuth. Captured data at each interval will be stamped with its corresponding location relative to the movement on the track. Platform movement and chirp signal transmit trigger are controlled by the SAR system that was explained in Chapter 3.

Knowing the geometry of our setup several SAR performance parameter can be estimated. The range resolution δ_r is inversely proportional to the system bandwidth, B_r, according to the equation

$$\delta_r = c_0/2B_r \,, \tag{5.3}$$

where c_0 is the speed of light. The range distance is r_0, and synthetic aperture length is given by $L_{sa} = \lambda r_0/L_a = 2.55$ meters. The azimuth resolution can be estimated using the following equation:

$$\Theta_a = r_0 \frac{\lambda}{2L_{sa}} = \frac{L_a}{2} \tag{5.4}$$

The antenna real aperture length is L_a = 590 mm. Eq. (5.4) shows that the azimuth resolution is half the antenna length, thus the azimuth resolution is roughly 295 mm.

5.2.1 Single point CP range measurement

Some of the cross-polarized RL measured range data is shown in Figure 5.2. It shows a high intensity scatter reading that occurs after the chirp signal travels from the FPGA, through the RF front-end amplifier, via coaxial cables to the antennas, propagate through the air, hitting the reflector target and returning in a reverse direction. The analog to digital converter sampling rate of 200 MHz also captured multi-scattering signals that show behind the main spike signal. The multi-scattering signals appear to be periodic and is assumed to be bouncing of the propagating signals between the antenna and plate reflector.

By arranging the range data bins along each of the 51 azimuth points, the entire raw data set can be represented as an image as shown in Figure 5.3. The figures show that co-polarized signals have more scattering. Comparatively, cross-polarized signals have notably less scattering as described previously, and have greater magnitude.

5.2.2 Range profile measurements

Theoretically, co-polarized measurements (LL and RR) should have reduced scattering as compared to cross-polarized setup [52]. This is consistent with the measured intensity values between the two cases. In the case of using a flat plate as a reflector, utilizing cross-polarized antennas provide a clearer image of the target.

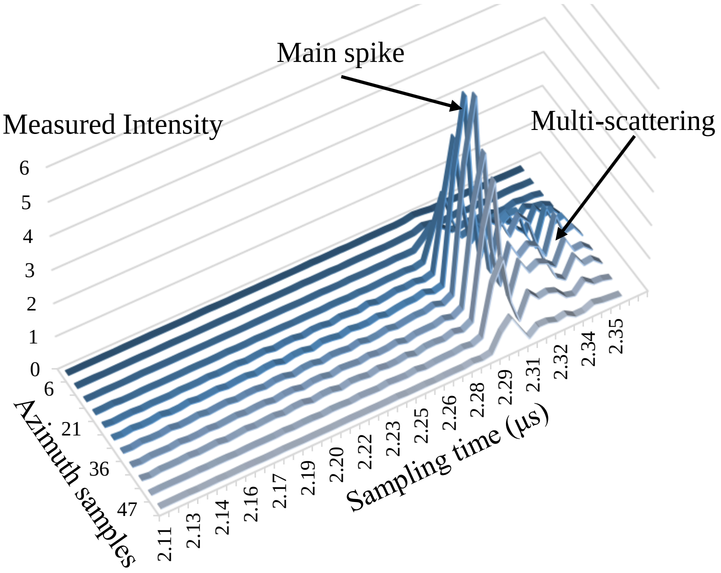

Figure 5.2: Measured RL range data showing high intensity caused by reflection from the plate on the moving platform.

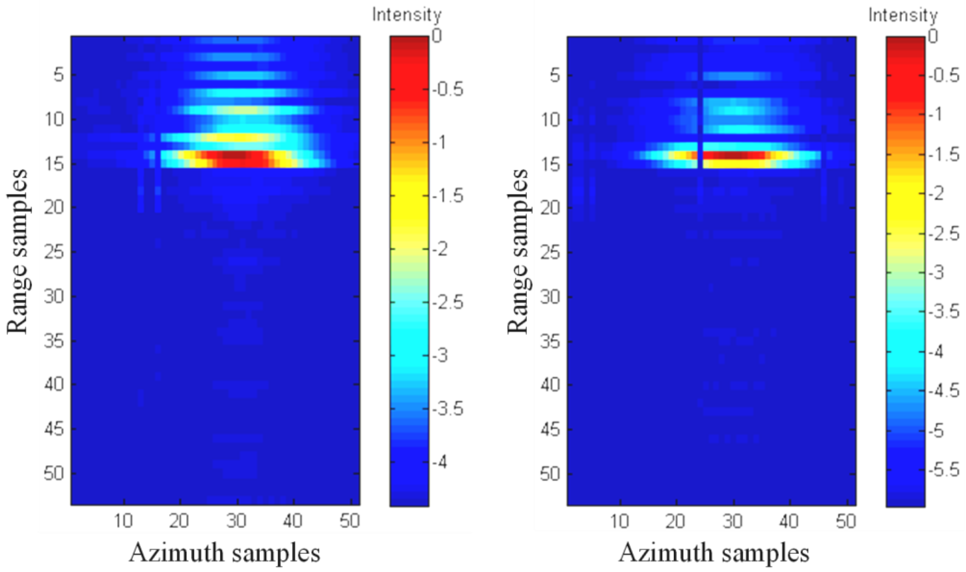

(a) (b)

Figure 5.3: Entire raw data range bins sampled for (a) co-polarized (RR), and (b) cross-polarized configurations (RL).

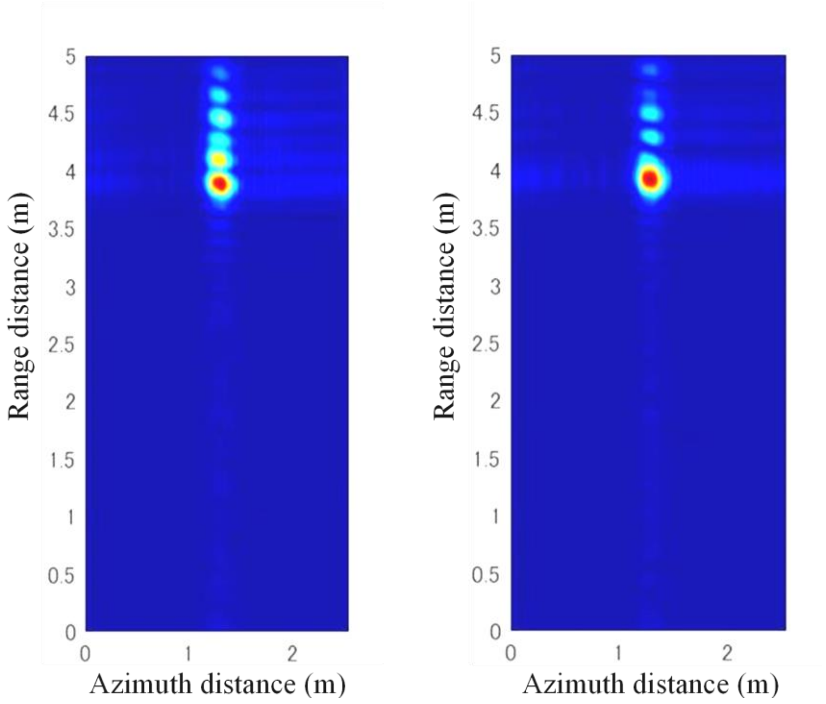

(a) (b)

Figure 5.4: Range and azimuth compressed image output for (a) co-polarized (RR), and (b) cross-polarized configurations (RL).

5.3 Rotary Turntable SAR

Next, a study is made by using a rotary turntable with the inverse SAR measurement method. Here, different combinations of frequency bandwidth and antenna polarizations were tested and compared. The receiving and transmitting radar are stationary. Again, the setup is a quasi-monostatic RCS measurement, such that receive and transmit antennas are spatially separated by a distance of 20 mm apart. A set of open boundary quad-ridged horn antennas with operating capability between 700 MHz to 10 GHz, which can be set to be linearly or circularly polarized, was utilized [41]. The planned operating bands are X, C and L-bands. A target to be observed is placed on a polystyrene turntable at a range distance, R, of 70λ away from the antennas so that the incident wave can be considered as a plane wave. The turntable angle, θ, can be controlled to an angular resolution, $\Delta\theta$, of 0.1°. A two-port vector network analyzer (VNA) provides a convenient means of generating the SFCW signal for transmission and capturing the backscattered signals.

Setting up the VNA correctly is critical to ensure good response data is captured. Important settings for the VNA include center frequency, frequency span, transmit power, scattering measurement, number of sampling points and time-domain gating. A repetition of the response signal at regular intervals caused by insufficient sampling is called aliasing. The alias-free range is directly proportional to the number of sampling points and inversely proportional to the frequency bandwidth, given by the following equation [53].

$$\text{Alias-free range (meters)} = (1/\Delta f) \times V_f \times c \tag{5.5}$$

where

Δf = frequency step size (frequency bandwidth / number of sampling points)

V_f = the velocity factor in the transmission line

c = velocity of light in free space, 3×10^8 ms^{-1}

The alias-free range is the entire electrical length traveled by the signals from port 1 to port 2 of the VNA. Taking into account the lengths of the 20 meter long cables connecting the VNA to the antennas, the distance to the target, and a velocity factor of 0.66 for polyethylene dielectric cables, the number of sampling points and frequency bandwidth can be calculated. In this study, the maximum bandwidth is 4 GHz, which corresponds to a minimum sampling number of 606. The minimum sample number on the VNA was chosen to be at least 801 points.

The target range resolution of a radar is the ability to distinguish between two or more targets that are very close in the range direction. The theoretical range resolution, ΔR, can be calculated with the following equation.

$$\Delta R \geq \frac{k_r \times c \times v_f}{2 \times bw} \tag{5.6}$$

In Eq (5.6) k_r is the response resolution factor which is based on the relationship between the frequency bandwidth and the VNA window selection on response resolution mode for responses of equal amplitude. Using the bandpass impulse time domain mode with minimum window, k_r is estimated to be 1.20. We are only interested in signals that are propagated in the free space between the antenna and target, thus the velocity factor here is 1.0. If the bandwidth is 4 GHz, the range resolution is calculated to be 45 mm.

5.3.1 Radar measurement

To test the validity of the measured data, measurements were made on a point target using real aperture radar. For calibration, both transmit and receive antennas were set to vertical polarization (VV). The initial target to be imaged was a flat aluminum plate of 8λ x 10λ in size. The antennas and target were all located 1.50 meters above the ground level. This setup can be seen in Figure 5.5. Turntable rotation angle, measurement trigger and data logging were controlled by a custom computer program which communicates via a general purpose interface bus (GPIB). Frequency response of the target is captured and is as shown in Figure 5.6. At the VNA, a time domain gating windowing function was used to obtain data only for the desired target zone. Time domain gating is formulated as follows:

$$f(t) = f_o(t) * w(t) \tag{5.7}$$

where

$f(t)$ = gated signal
$f_o(t)$ = original signal before gating
$w(t)$ = windowing function

(a) Metal plate for point target measurement placed on a rotating polystyrene platform in an anechoic chamber. Note the quasi-monostatic placement of the receiving and transmitting horn antennas.

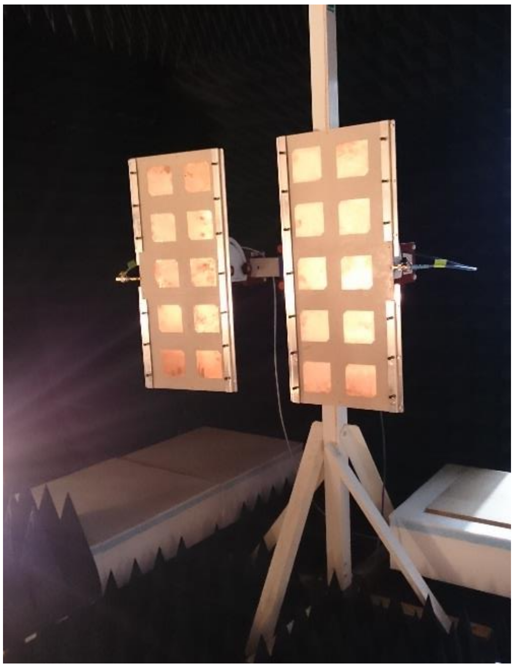

(b) Custom circularly polarized microstrip patch array antenna as receiving and transmitting radar antennas.

Figure 5.5: Antennas and target setup in an anechoic chamber.

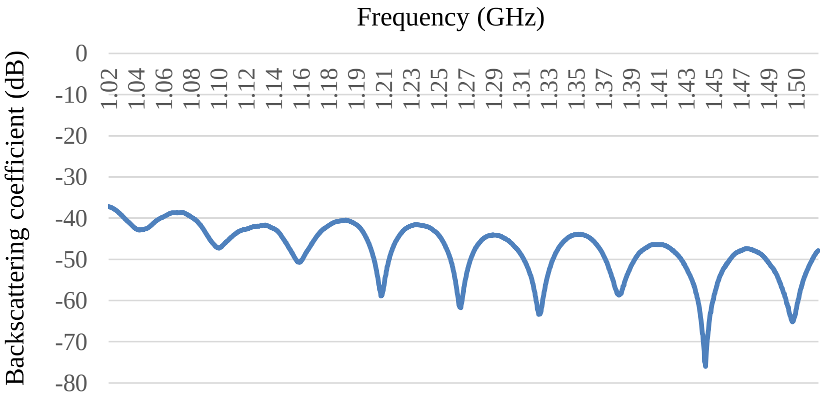

Figure 5.6: Frequency response of a steel plate at L-band 1.27 GHz with 500 MHz bandwidth.

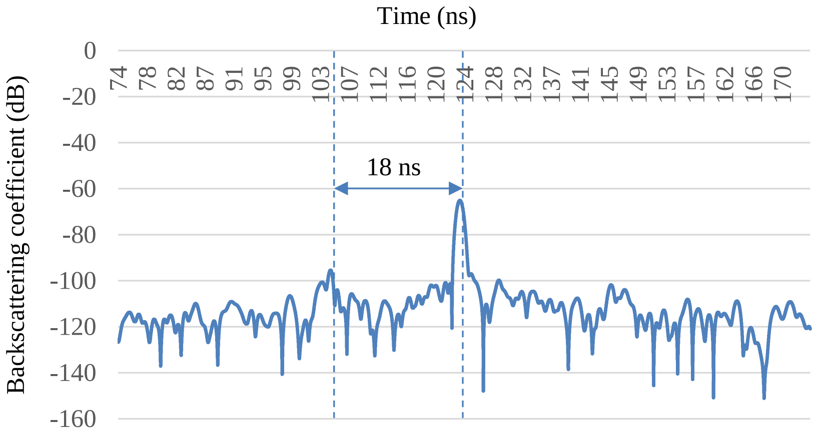

Figure 5.7: Range profile in the time domain after transformation.

Measured frequency points from the VNA was converted to backscattering coefficients versus range profile in time domain using Inverse Fast Fourier Transform (IFFT). The time domain transformed waveform showing measured scattering response of the target perpendicular to the antenna illumination is shown in Figure 5.7. Distance calculated from the radar to the target was based on the response time where there is a peak intensity. The calculated distance matches the actual location in the setup.

For a parametric comparison, a method-of-moments based software was used to simulate RCS values of the target [54] [55]. The horn antenna was also simulated to provide the closest possible radiation pattern to the actual antennas in the experiment. Waveforms showing simulated scattering response of the target perpendicular and parallel to the antenna illumination are shown in Figure 5.8(a). Measured values shown in Figure 5.8(b) were considerably weaker than the simulated response with a 30 dB difference. This is most probably due to the simulation not taking into account of the signal propagation loss. Simulated and measured results for the entire cross-range field is shown in Figure 5.9. Measurement was tested on the required X, C, S and L-bands. Findings for each band are noted in the following sections.

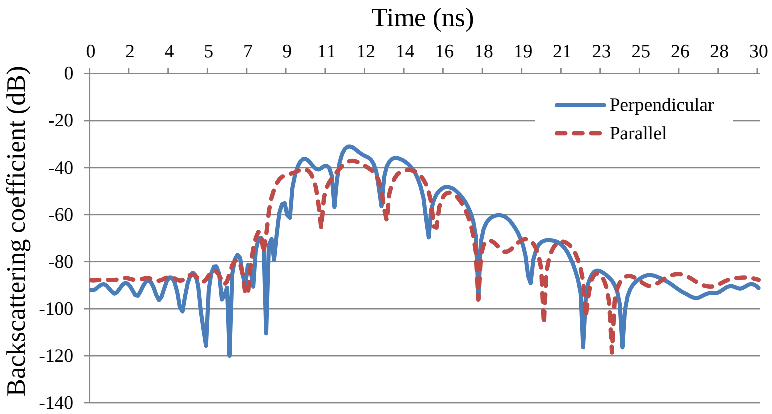

(a) Simulated results

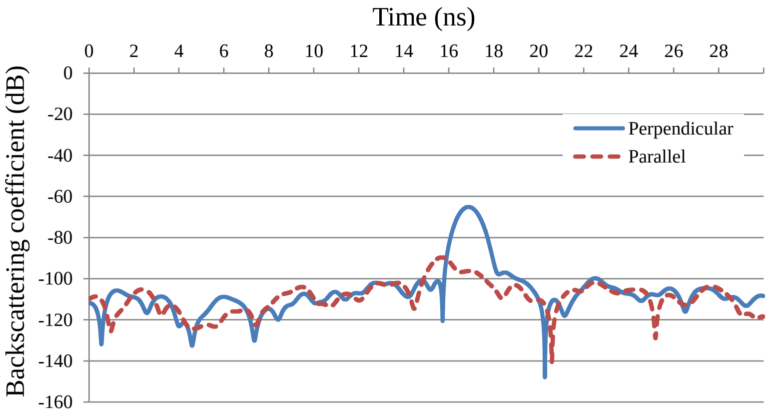

(b) Measured results

Figure 5.8: Range profile of the target at $\theta = 0°$ (perpendicular) and 90° (parallel).

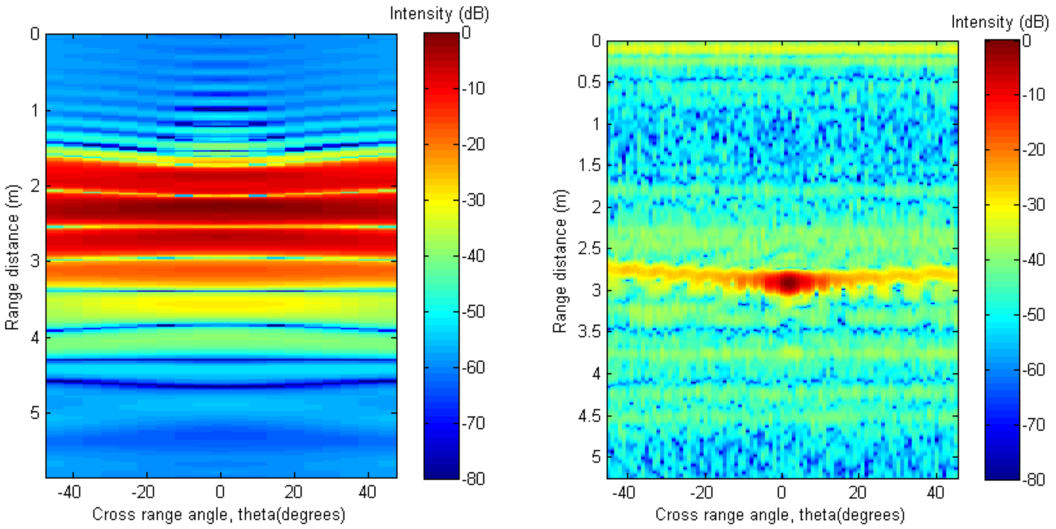

(a) Simulated results

(b) Measured results

Figure 5.9: Baseband ISAR (angle (θ), range (r)) domain data of the target.

5.3.2 Comparison of measured results

The next step after the data capture is the two-dimensional Fourier transform that will generate the desired ISAR image. Variations can be made in the transform method to provide different quality images with different processing times. The radar antenna can also be changed to study the effects of using circular polarized signals on the ISAR image.

5.3.2.1 X-band measurement

A 9.0 GHz SFCW signal with 1.0 GHz bandwidth was set for transmission. Transmit power in the X-band mode was set between 0 dBm and 1 dBm for the target to be clearly visible in the point target measurement.

5.3.2.2 C-band measurement

A C-band signal was generated with a center frequency of 6.0 GHz and bandwidth of 4.0 GHz using a VNA. The fractional bandwidth is thus 130% which puts our measurement in the ultra-wideband range. In this operating frequency range the far field condition is easily fulfilled with an open boundary quad-ridged horn antenna placed 2.75 meters from the target. At 6 GHz the antennas have a 3dB beamwidth of 32°. An S21 measurement is performed and the frequency and time domain response data from -45° to +45° rotation of the target is saved. The entire cross-range response in time domain is shown in Figure 5.9(b). The target can clearly be seen in the middle of the image as the object with the highest intensity.

5.3.2.3 S and L-band measurement

The S and L-band frequencies were set at the VNA to be 2.5 GHz and 1.27 GHz respectively. With a relatively narrow bandwidth of 500 MHz, it was noticed that even at minimum power output setting, the peaks of the antennas and target were visible during the point target test.

5.3.2.4 L-band with circularly polarized antennas

The horn antennas were replaced with a set of circularly polarized microstrip antenna arrays which were previously developed [45]. Figure 5.5(b) shows the array antenna mounted in the anechoic chamber. The 10-element array has a center operating frequency of 1.27 GHz and a narrow bandwidth of 77 MHz.

5.3.2.5 Observations

Using the customized circularly polarized antennas to generate SAR images prove to be challenging as the reflection intensity is less compared to linearly polarized antennas. Variation of the phase values also have to be taken into account by post-processing algorithms. In terms of data quality, measurements with larger bandwidths provide clearer peaks in the point target test. This is in agreement with the theory of higher bandwidth being proportional to the image resolution. However larger bandwidth is only useful if it can be captured and recorded. Thus a high sampling number is also required. The GPIB connection between the control computer and VNA does not provide sufficient data transfer speeds to perform continuous sampling even at the slowest turntable rotational speed. To overcome this limit, a stop-and-go method of data capture had to be adopted.

A system in an anechoic chamber to study fundamentals and test variation in ISAR imaging solutions was developed and tested. By changing the VNA parameters such as frequency range, power output and sampling number, changes in the measured results were observed. Differences in readings when using different antenna types were also studied. Experimental as well as simulated results have been obtained in this study for comparison and analysis.

5.4 Turntable Imaging Experiments

Antennas were placed in a quasi-monostatic arrangement such that receive and transmit antennas are spatially separated by a distance of 300 mm apart. For linearly polarized operation, a set of open boundary quad-ridged horn antennas with operating capability between 700 MHz to 10 GHz was utilized [41]. Due to the developed CP patch antennas having small axial ratio bandwidth and low polarization purity, conical log spiral antennas functioning between 1 GHz to 10 GHz were used for circularly polarized operation as seen in Figure 5.10. This enabled wide-band transmission of signals for higher resolution images. However, to further improve axial ratio purity and to maintain similarity between measurements, the same quad-ridged horn antennas were used to generate CP signals with the use of 90° phase shifters [42]. The phase shifters can be seen connected to the horn antennas in Figure 5.11. We confirmed the CP capability of each antenna configuration for left-handed and right-handed operation by performing axial ratio measurements in the anechoic chamber. The antennas and target mid-points were all located at the same height, 1.50 meters above the ground level with zero incidence angle.

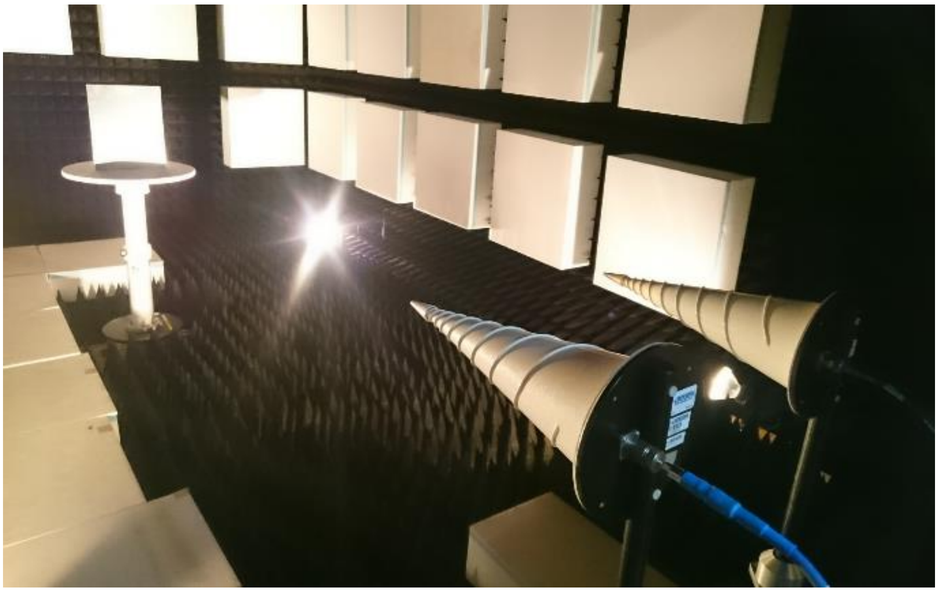

Figure 5.10: Conical log spiral antennas used for circular polarization (left) and flat aluminum plate for point target measurement placed on a rotating polystyrene platform (far right). Note the quasi-monostatic placement of the receiving and transmitting antennas.

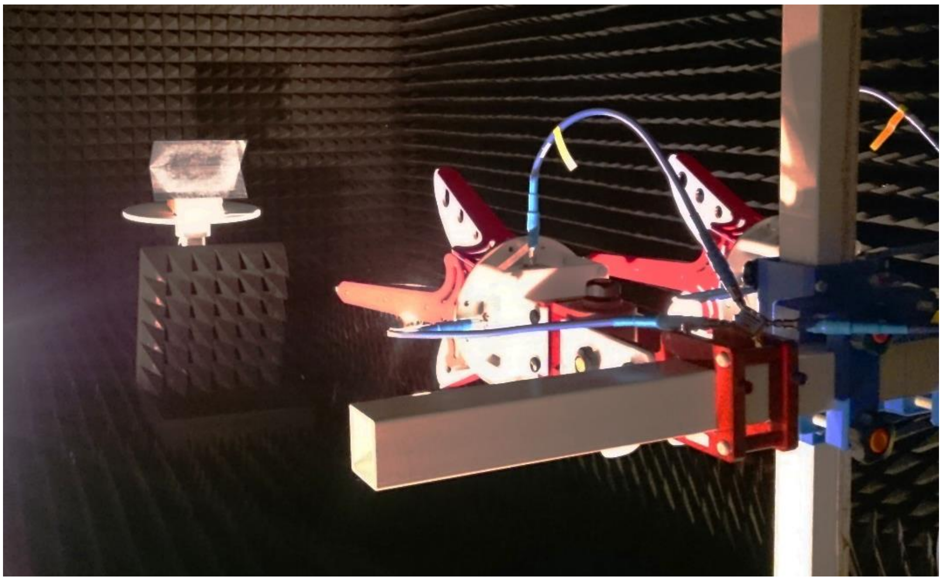

Figure 5.11: Horn antennas with phase shifters used for circular polarization (right) and a dihedral reflector for point target measurement placed on a rotating polystyrene platform (far left). Note the quasi-monostatic placement of the receive and transmit antennas.

For transmit power, the maximum possible value was set to ensure good signal-to-noise ratio. Transmit power was set to 5 dBm (3.16 mW). A C-band signal was generated with a center frequency of 6.0 GHz and bandwidth of 4.0 GHz using a VNA. The fractional bandwidth is thus 130% which puts our measurement in the ultra-wideband range. To avoid aliasing, the minimum sampling number was chosen to be at least 801 points [53]. A measurement is to be made at each rotating angle and saved as a range bin measurement.

5.4.1 Single Point CP Range Measurement

A point target measurement was first made to test the validity of the measured data. First the frequency range, number of measurement points, and transmit power are set using values that were previously discussed. Then the VNA was calibrated to these settings with a 2-port calibration at the antenna connection points. Circularly polarized antennas were used for both receive and transmit. This setup of the antennas with the target on the turntable was shown in Figure 5.11.

Frequency response of the chamber without a target was first measured and saved as background noise data, S_{bn}. Measured data consists of complex values of the scattering readings. The target was then placed perpendicular to the radar and the data captured and saved as measured data, S_m. Using (5.8) we calculated the single range data bin with background noise removed, S_r, in the frequency domain and the CP response for each polarization is as shown in Figure 5.12.

$$S_r\,(f, \theta) = S_m(f, \theta)\ - S_{bn}(f, \theta) \tag{5.8}$$

The VNA can be used to quickly confirm the target location. Measured frequency points was converted to backscattering coefficients versus range profile in time domain using Inverse Fast Fourier Transform (IFFT). Since we have set the sampling rate and frequency range, the frequency interval Δf is known. The maximum theoretical range, R_{max}, can then be calculated using (5.9) to convert the time domain into distance.

$$R_{max} = c\,/\,(2\,\Delta f) \tag{5.9}$$

A time domain gating windowing function was used to obtain data only for the desired target zone. The transformed waveforms showing measured scattering response of the target perpendicular to the antenna illumination are shown in Figure 5.13. The detected distance matches the actual location in the setup. The low co-polarized and high cross-polarized reading confirms polarimetric measurement of a flat plate target.

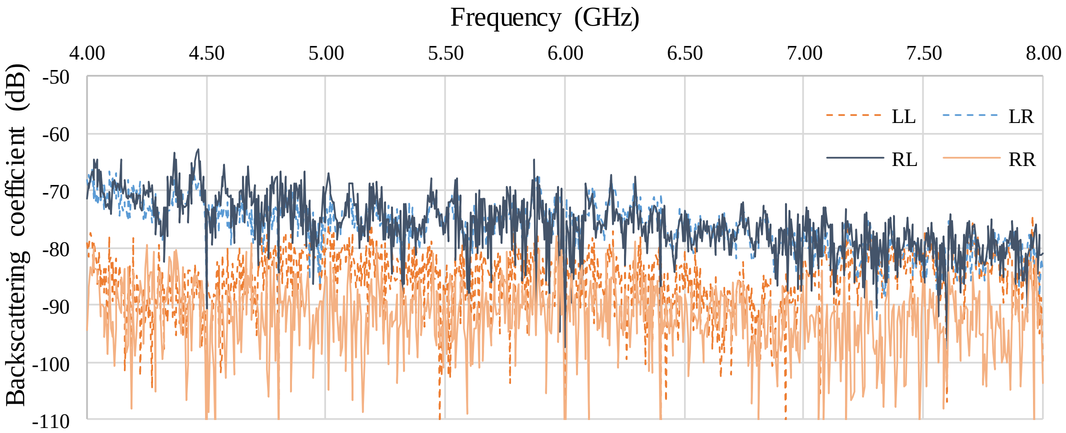

Figure 5.12: CP frequency response of a flat plate at C-band 4-8 GHz with background noise removed. Note the relatively high readings for cross-polarized setup compared to co-polarization.

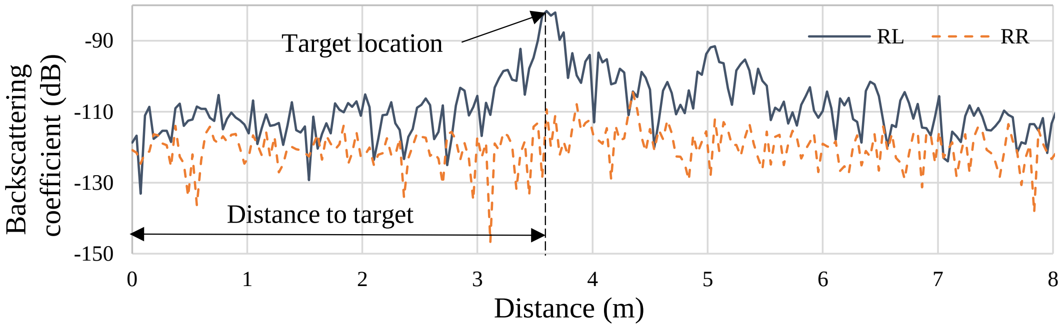

Figure 5.13: Range profile of RL and RR data for perpendicular flat plate after IFFT range compression.

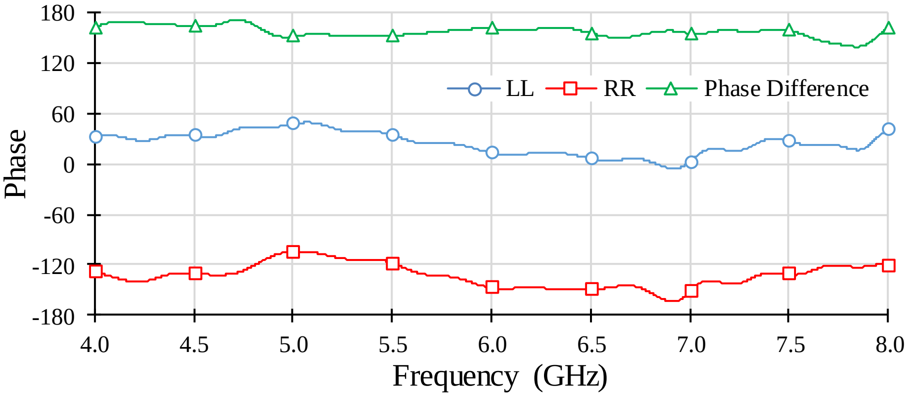

Figure 5.14: Phase difference of the co-polarized scattering signals detected from a dihedral reflector is close to 180 degrees.

We could also confirm that measured phases was in line with scattering theory. The phase, ϕ, of a target was calculated by taking scattering signals of a perpendicularly placed target and multiplying it by a phase factor:

$$\phi(f,\theta) = e^{j(k_r \cdot R)} \times S_r(f,\theta) \qquad (3)$$

where the wave number k_r is $4\pi f/c$ and R is the range distance to the target. Figure 5.14 shows uncalibrated phase of CP co-polarized (LL and RR) scattering signals detected from a dihedral. The difference between the two phases is close to the theoretical value of 180° and shows that the system is able to evaluate phase changes. The phase precision can be further improved with polarimetric calibration.

5.4.2 ISAR Measurement

The next step towards imaging the target is to collect scattering responses at multiple angles. The turntable angle θ was rotated from 0° to 180° with a resolution, $\Delta\theta$, of 1.0° for a total of 180 points. At each angle, the turntable stops and makes a measurement with the same VNA settings as previously explained. A customized computer program which communicates via a general purpose interface bus (GPIB) controls the turntable rotation angle, measurement trigger and data logging. Finally, to obtain an image of the scene using the measured range bins, cross-range compression needs to be performed. This was done with a back-projection algorithm [24][25]. The process above was repeated for all CP and LP polarimetric combinations by changing the horn antenna configuration. The generated images for a rectangular plate reflector for LP and CP are shown in Figure 5.15 for comparison.

Figure 5.15(a) shows LP imaging results. The images are normalized and displayed with a wide dynamic range to understand the scattering effects. We can remove the ripples around the target by simply limiting the dynamic range to around -20 dB. As can be seen in image (1,1) and (2,2) of Figure 5.15(a), the aluminum plate can be visualized when using co-polarized configurations. Images (1,2) and (2,1) show that cross-polarized LP antennas can still barely detect the target since there are fringing effects at the sides of the target.

Figure 5.15(b) shows imaging results when using CP antennas. The cross-polarized results in image (1,4) and (2,3) are as expected from a flat plate target and consistent with the respective theoretical scattering matrix. Some scattering was detected at the target location, which may be due to edge reflections or antenna cross-polarization impurity. The polystyrene column used for mounting was not detected in any measurement. Observation of the full polarimetric imaging results for both CP and LP are consistent with theoretical polarimetric scattering response of a flat plate.

We next tested a dihedral reflector and again confirmed that the measured scattering matches with the theory in literature. The reconstructed dihedral images are shown in Figure 5.16. Phase information was also retained as explained in Section 5.4.1.

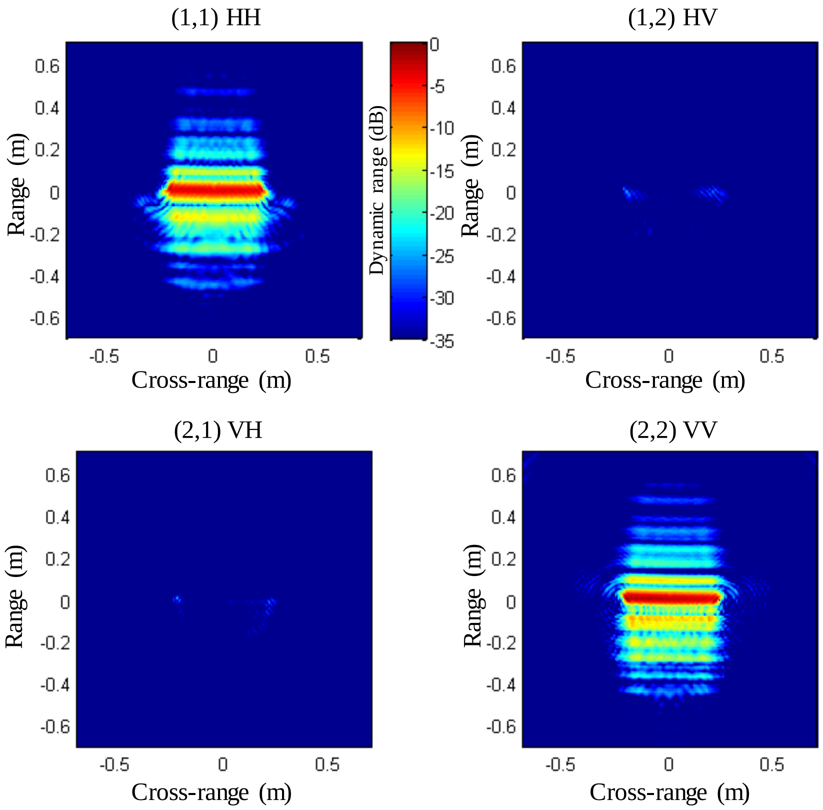

(a) LP imaging output

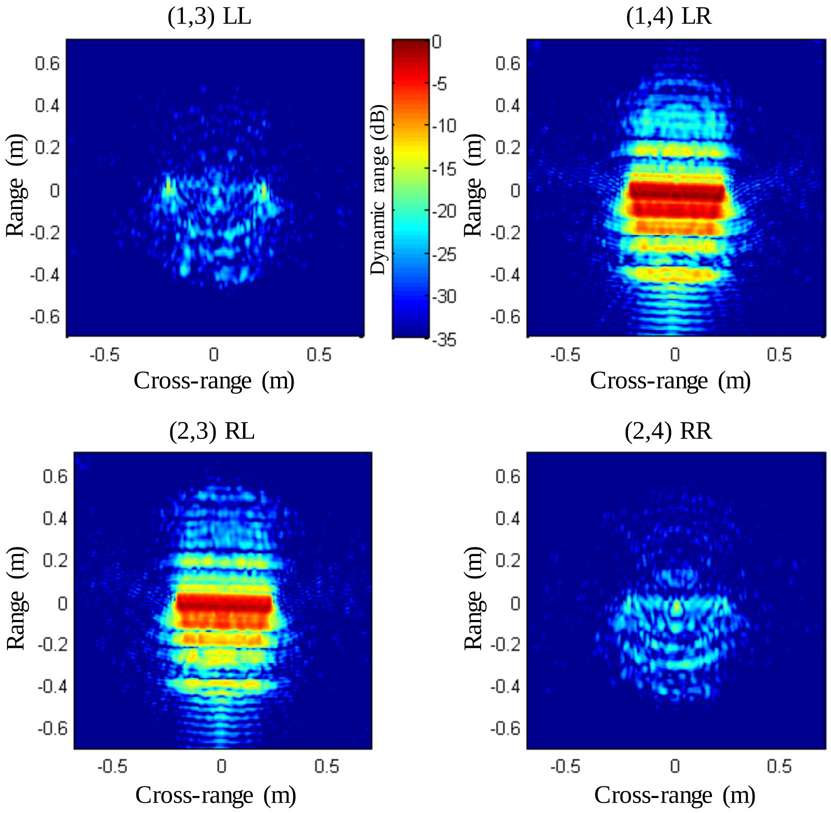

(b) CP imaging output

Figure 5.15: Comparison of linear (LP) and circular polarized (CP) imaging output of a flat plate reflector.

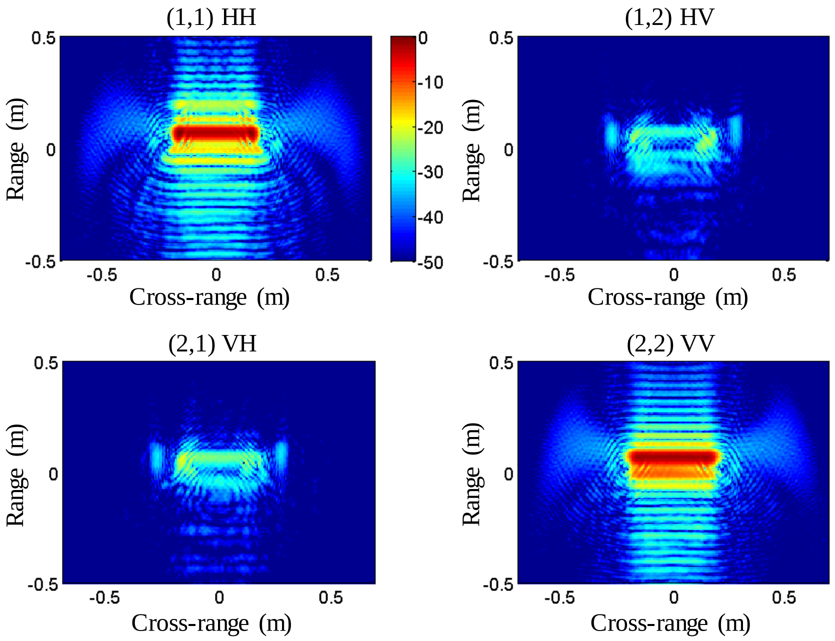

(a) LP imaging output

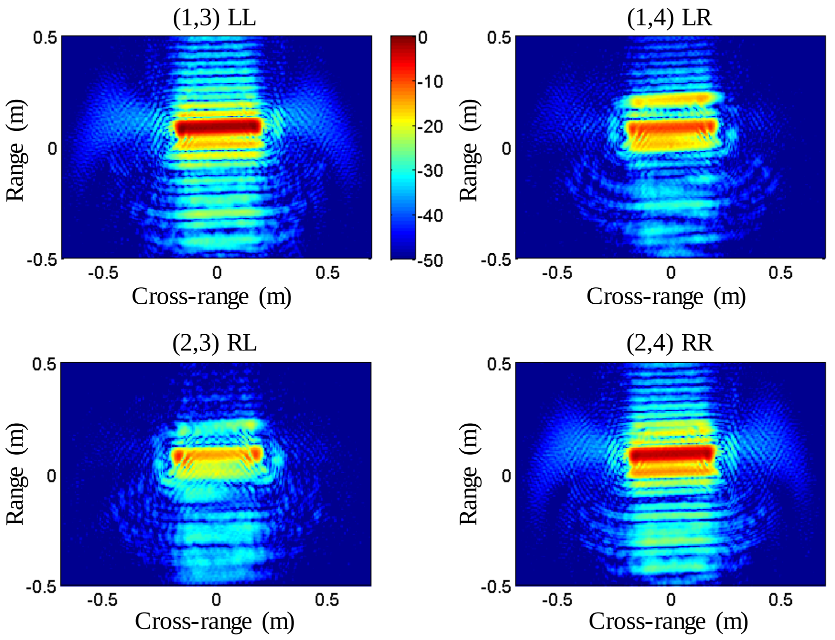

(b) CP imaging output

Figure 5.16: Comparison of LP and CP imaging output of a dihedral reflector.

Finally, imaging of three identical thin vertical poles spaced 450mm apart is shown in Figure 5.17. The metal poles have a diameter of 2 mm, around 5% of the wavelength at 8 GHz. We selected the diameter of the poles to be much smaller than the smallest wavelength to ensure sensitivity to reflector orientation. LP images of the vertically oriented poles are as expected showing good scattering for VV and no scattering for all other polarization pairs. The individual poles can be clearly imaged with matching scattering responses. CP images, on the other hand, have scattering for all receive-transmit pairs. Together with the phase information, these are the results that we consider valuable for continuing polarimetric SAR studies.

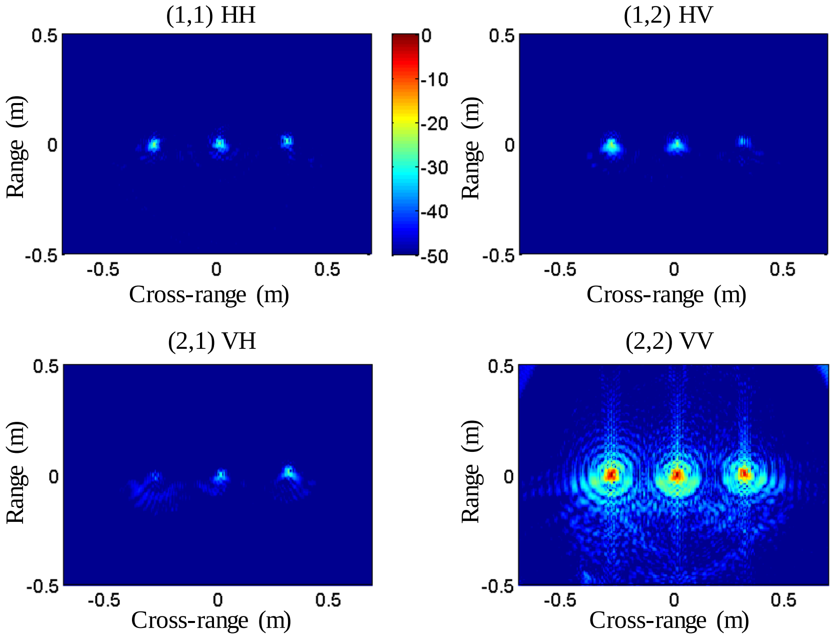

(a) LP imaging output

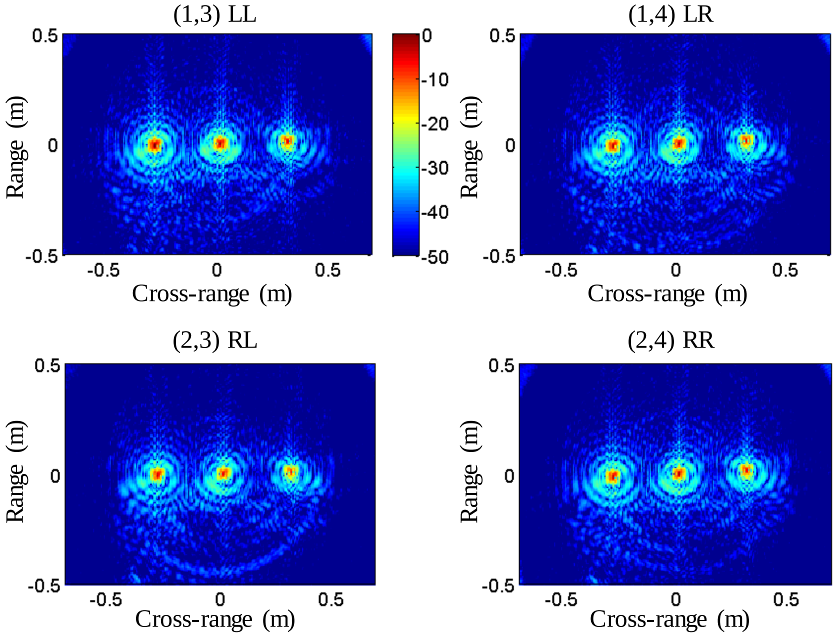

(b) CP imaging output

Figure 5.17: Comparison of LP and CP imaging output of three thin vertical poles.

Since the canonical targets provided satisfactory results, complex targets can then be imaged. A model airplane as shown in Figure 5.18 was imaged with the imaging output as shown in Figure 5.19. The model is made of wood with a resin skin. This combination provides a low but sufficient scattering reading. Only one side of the target was scanned. The back-projection algorithm was still able to image the target. In Figure 5.19 the dynamic range is only shown from zero to -20dB to view a clear shape of the aircraft. Small targets such as the wing and tail tips can be clearly seen. The middle of the image is a cluster of readings due to multipath scattering by various complex objects around the aircraft body such as the propellers and landing wheels. A close comparison between the LP and CP images show that the response is close to the dihedral as discussed previously. Co-polarized LP readings were much clearer than cross-polarized. But for CP, all polarization pairs detected scattering from the target. This result is promising and provides some insight into the study of polarimetric calibration.

Figure 5.18: A model airplane used a complex target to be imaged by the developed system.

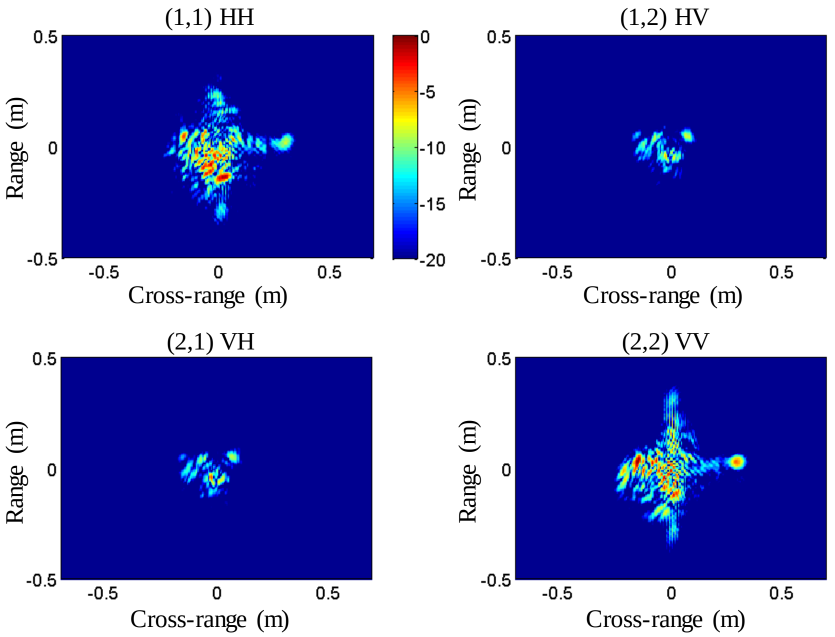

(a) LP imaging output

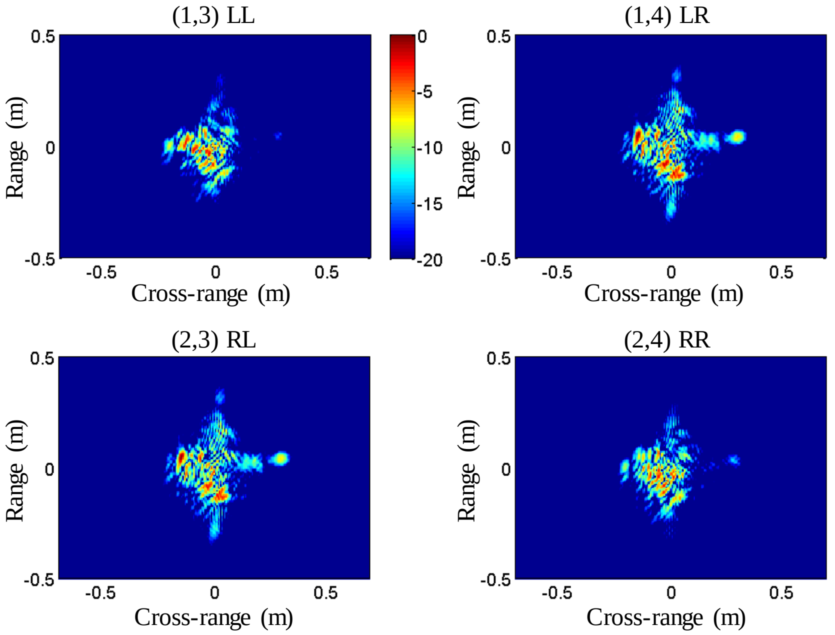

(b) CP imaging output

Figure 5.19: Comparison of LP and CP imaging output of a model airplane.

Chapter 6 CONCLUSION AND FUTURE DEVELOPMENTS

A new reconfigurable anechoic chamber based SAR measurement system has been developed. Prototyped antennas customized for the developed SAR system were tested and imaging solution was also established. Progress has been made in SAR imaging using circularly polarized antennas. The software and hardware systems developed in this thesis are towards the advancement of a stand-alone airborne or spaceborne circularly polarized synthetic aperture radar system.

The entire development process was shown in this thesis, starting with a pilot study to confirm understanding of SAR concepts, design and fabrication of array antennas suitable according to airborne SAR requirements, ending with integration of an indoor close-range SAR measurement solution.

It was shown that the system design is flexible and can be adapted to multiple frequencies. Wideband LP and CP antennas were successfully used for imaging in different frequency bands to study the effects of varying sampling points, bandwidth, and azimuth length among others towards the output image. Following this, customized antennas bound for airborne applications were designed and used with the developed SAR system for performance verification.

The antennas were designed using microstrip patch antenna technology, which is suitable for the light-weight and low profile requirement. In one of the proposed designs several microstrip concepts were implemented in a single array to achieve beam steering at a steep angle, reduced side-lobe level using Dolph-Chebyshev synthesized weights, and minimized spurious radiation via optimized feed network on dual substrates. Full-wave electromagnetic simulation software was used to design and optimize antennas prior to fabrication. The same simulation software was also used to simulate backscatter properties of targets and then compared with measured results using the developed system.

Circularly polarized synthetic aperture radar imaging has numerous possible applications in the mapping of land surface, interferometry, wave scattering mechanism study of snow, ice, vegetation, rocky and desert areas. Potential applied research includes ocean monitoring, snow or ice monitoring and disaster monitoring. The following are proposed future work, which were identified during the course of this work.

1. Antenna bandwidth enhancement for increased image resolution. A major drawback of microstrip antennas is the narrow impedance bandwidth. From that impedance bandwidth, the axial ratio bandwidth required for circular polarization is even smaller. One proposed method to incorporate sequential feeding to increase CP purity, at the expense of a more complicated feed network.
2. Polarimetric calibration to account for losses and errors in the system. Polarimetric calibration of CP radar systems is relatively unexplored and provides a good research opportunity. Initial attempts at CP calibration have proved sufficient but a lot of improvement is still possible.
3. Study the scattering of different targets. Using the rotating turntable, ISAR imaging of real world targets becomes arbitrarily simple. With it, the scattering of CP on various targets such as plants can be studied.
4. Use different imaging algorithms. Only the back-projection algorithm was used in this work, but many other imaging algorithms exist. Studies should be made into discovering the best algorithm for CP.
5. Three-dimensional imaging of targets. This would require major modification to the measurement setup, however the study of three-dimensional imaging using SAR concepts is interesting.
6. Replacing the VNA with different RF front-ends, which would allow the system to be capable of imaging at further distances. An outdoor test is imminent and even though the developed system is capable of performing outdoor measurements, it is not powerful enough for the intended airborne application. Use of RF chirp generators and amplifiers will be of great benefit and study.

This work initially began as a study to design CP antennas for SAR. It has progressed to include development of a basic but reconfigurable and modular SAR imaging system. The research area of SAR imaging using circularly polarized antennas is diverse. In this dissertation, it was decided to focus on mainly C-band measurements. More improvement is still possible in this area and it shows great potential for the eventual application into airborne and spaceborne platforms.

REFERENCES

[1] Pierce, G. Washington, *Principles of Wireless Telegraphy*, pp. 51-55, McGraw Hill: New York, 1910.

[2] C.A. Balanis, *Antenna Theory*, 3rd ed. Hoboken, N.J.: Wiley, 2005.

[3] M. Jehle, M. Ruegg, L. Zuberbuhler, D. Small and E. Meier, "Measurement of Ionospheric Faraday Rotation in Simulated and Real Spaceborne SAR Data," in IEEE Transactions on Geoscience and Remote Sensing, vol. 47, no. 5, pp. 1512-1523, May 2009.

[4] W. A. Imbriale, S. Gao, L. Boccia, *Space Antenna Handbook*, Wiley, May 2012.

[5] S. Gao, Q. Luo, and F. Zhu, *Circularly Polarized Antennas*, Wiley-IEEE Press, November 2013.

[6] K. Suto, J. T. S. Sumantyo, V. C. Koo, M. Y. Chua and W. G. Cheaw, "Development of SAR base-band signal processor using FPGA and onboard PC," 2014 IEEE Geoscience and Remote Sensing Symposium, Quebec City, QC, 2014, pp. 672-675.

[7] M. Z. Baharuddin, K. Suto, J. T. S. Sumantyo, H. Kuze, L. T. Sze, J. Y. K. Shen, W. G. Cheaw, K. V. Chet, “Development of a semi-automated SAR test-bed,” IEEE 2nd Intl. Symp. on Telecommunication Technologies (ISTT), Langkawi, 2014, pp. 236-240.

[8] Ministry of Internal Affairs and Communications, Japan (2016, May 10). *Technical Regulations Conformity Certification System* [Online], Available: http://www.tele.soumu.go.jp/e/sys/equ/tech/

[9] M. Z. Baharuddin, B. Setiadi, J.T.S. Sumantyo, H. Kuze, “An experimental network analyzer based ISAR system for studying SAR fundamentals,” in IEEE 5th Asia-Pacific Conference on Synthetic Aperture Radar (APSAR), Singapore, 1-4 Sept. 2015, pp.103-107.

[10] A. Moreira, P. Prats-Iraola, M. Younis, G. Krieger, I. Hajnsek, K.P. Papathanassiou, “A Tutorial on Synthetic Aperture Radar,” IEEE Geoscience and Remote Sensing Magazine, vol. 1, no. 1, pp. 6-43, March 2013.

[11] D.J. Kim, W.M. Moon, Y.S. Kim, “Application of TerraSAR-X Data for Emergent Oil-Spill Monitoring,” Geoscience and Remote Sensing, IEEE Transactions on , vol.48, no.2, pp.852-863, February 2010.

[12] R.F. Putri, J. Sartohadi, H. Kuze, and J.T. Sri Sumantyo, “Monitoring and Analysis of Landslide Hazard using DInSAR Technique Applied to ALOS PALSAR Imagery: A Case Study in Kayangan Catchment Area, Yogyakarta, Indonesia,” Journal of Urban and Environmental Engineering (JUEE), Vol. 7, No. 2, pp.308-322, February 2013.

[13] W. Graham, “Japanese HII-A successfully launches ALOS-2 mission,” NASASpaceFlight.com [online] 2014, http://www.nasaspaceflight.com/2014/05/japanese-hii-a-launch-alos-2-mission/ (Accessed: 16 June 2014).

[14] P.R. Akbar, J.T. Sri Sumantyo, H. Kuze, “A Novel Circularly Polarized Synthetic Aperture Radar (CP-SAR) onboard Spaceborne Platform,” International Journal of Remote Sensing (IJRS), Vol. 31, No. 4, pp. 1053-1060, 20 February 2010 (London : Taylor & Francis).

[15] J.T. Sri Sumantyo, “Circularly Polarized Synthetic Aperture Radar Onboard Unmanned Aerial Vehicle (CP-SAR UAV),” Autonomous Control Systems and Vehicles, Intelligent Systems, Control and Automation: Science and Engineering, Vol. 65, Springer, pp. 175-192, 2013.

[16] C.C. Chen, H.C. Andrews, “Target-motion-induced radar imaging”, IEEE Tran. Aerospace Electronic Systems, Vol. AES-16, No. 1, pp. 2-14, 1980.

[17] M. Soumekh, *Synthetic Aperture Radar Signal Processing with MATLAB Algorithms*, 1-st edition, Wiley-Interscience, Canada, 1999.

[18] V.G. Borkar, A. Ghosh, R.K. Singh, and N. Chourasia, “Radar cross-section measurement techniques”, Defence Science Journal, Vol. 60, No. 2, pp. 204-212, 2010.

[19] W.G. Carrara, R.S. Goodman, R.M. Majewski, *Spotlight Synthetic Aperture Radar Signal Processing Algorithms*, Artech House, Norwood, MA, USA, 1995.

[20] N. Dahlbäck, Implementation of a fast method for reconstruction of ISAR images, student thesis, Institutionen för systemteknik, Linköping, Sweden, 2003.

[21] N.C. Currie, *Radar Reflectivity Measurement: Techniques & Applications*, Artech House, Norwood, MA, USA, 1989.

[22] A. F. Yegulalp, "Fast backprojection algorithm for synthetic aperture radar," Radar Conference, 1999. The Record of the 1999 IEEE, Waltham, MA, 1999, pp. 60-65.

[23] D. Meng, D. Hu and C. Ding, "Precise Focusing of Airborne SAR Data With Wide Apertures Large Trajectory Deviations: A Chirp Modulated Back-

Projection Approach," in IEEE Transactions on Geoscience and Remote Sensing, vol. 53, no. 5, pp. 2510-2519, May 2015.

[24] S. Demirci, H. Cetinkaya, E. Yigit, C. Ozdemir and A. Vertiy, “A study on millimeter-wave imaging of concealed objects: application using back projection algorithm,” PIER, vol. 128, 2012, pp. 457-477.

[25] M. Soumekh, "Spotlight synthetic aperture radar," in *Synthetic Aperture Radar Signal Processing with MATLAB Algorithms*, 1st ed. Wiley-Interscience, New York, 1999.

[26] W.M. Boerner, “Basic concepts in radar polarimetry,” in PolSARpro V3.0 – Lecture Notes UIC-ECE Communications, Sensing & Navigation Laboratory, ESA, 1999.

[27] Natural Resources Canada (2015, Dec 20). Tutorial: Radar Polarimetry [Online], Available: http://www.nrcan.gc.ca/earth-sciences/geomatics/satellite-imagery-air-photos/satellite-imagery-products/educational-resources/9579

[28] J. C. Souyris, P. Imbo, R. Fjortoft, S. Mingot and J.-S. Lee, “Compact Polarimetry Based on Symmetry Properties of Geophysical Media: The π/4 Mode”, IEEE Trans. Geosci. Remote Sens., vol. 43, no. 3, pp. 634-646, 2005.

[29] M. E. Nord, T. L. Ainsworth, J. S. Lee and N. J. S. Stacy, "Comparison of Compact Polarimetric Synthetic Aperture Radar Modes," in IEEE Transactions on Geoscience and Remote Sensing, vol. 47, no. 1, pp. 174-188, Jan. 2009.

[30] R. Touzi and F. Charbonneau, "Requirements on the calibration of Hybrid-Compact SAR," 2014 IEEE Geoscience and Remote Sensing Symposium, Quebec City, QC, 2014, pp. 1109-1112.

[31] S. Hensley et al., "L-band and P-band studies of vegetation at JPL," 2015 IEEE Radar Conference, Johannesburg, 2015, pp. 516-520.

[32] Y. Kankaku, Y. Osawa, S. Suzuki, and T. Watanabe, "The Overview of the L-band SAR Onboard ALOS-2", Progress In Electromagnetics Research Symposium Proceedings, Moscow, Russia, August 18-21, 2009.

[33] J. T. Sri Sumantyo, "Development of circularly polarized Synthetic Aperture Radar onboard Unmanned Aerial Vehicle (CP-SAR UAV)," 2012 IEEE International Geoscience and Remote Sensing Symposium, Munich, 2012, pp. 4762-4765.

[34] J. T. S. Sumantyo, "Progress on development of synthetic aperture radar onboard UAV and microsatellite," 2014 IEEE Geoscience and Remote Sensing Symposium, Quebec City, QC, 2014, pp. 1081-1084.

[35] J. T. Sri Sumantyo, K. V. Chet and R. H. Triharjanto, "Development of circularly polarized Synthetic Aperture Radar onboard unmanned aerial vehicle," 2013 IEEE International Geoscience and Remote Sensing Symposium - IGARSS, Melbourne, VIC, 2013, pp. 2301-2304.

[36] J. T. S. Sumantyo and K. V. Chet, "Development of Circularly Polarized Synthetic Aperture Radar onboard UAV for Earth diagnosis," Synthetic Aperture Radar, 2012. EUSAR. 9th European Conference on, Nuremberg, Germany, 2012, pp. 136-138.

[37] *IEEE Standard Test Procedures for Antennas*, in ANSI/IEEE Std 149-1979 (R2008), 1979.

[38] B. Y. Toh, R. Cahill, and V. F. Fusco, “Understanding and measuring circular polarization,” IEEE Transactions on Education, vol. 46, no. 3, pp. 313–318, 2003.

[39] T.S. Lim, V.C. Koo, Y.K. Chan, H. Lateh, J.T. Sri Sumantyo, "Development of a ground-based Synthetic Aperture Radar for land deformation monitoring," Synthetic Aperture Radar (APSAR), 2013 Asia-Pacific Conference on , vol., no., pp.536-539, 23 September 2013.

[40] G.L. Charvat, L.C. Kempel, "Low-Cost, High Resolution X-Band Laboratory Radar System for Synthetic Aperture Radar Applications," 2006 IEEE International Conference on Electro/information Technology, pp.529-531, 7-10 May 2006.

[41] ETS Lindgren, *Wireless Antennas: Open Boundary Quad-Ridged Horn*, technical specifications datasheet, revision A, 2007.

[42] Mini-Circuits, Ultra-small ceramic LTCC power splitter/combiner, 2 way-90°, 50Ω, 4000 to 8000 MHz, QCS-83+ Datasheet, Rev. B.

[43] M.A. Richards, *Fundamentals of Radar Signal Processing*, New York, NY, McGraw-Hill, 2005.

[44] I.G. Cumming, F.H. Wong, “Digital Processing of Synthetic Aperture Radar Data: Algorithms and Implementation,” Boston: Artech House, 2005.

[45] Yohandri, V. Wissan, I. Firmansyah, P. Rizki Akbar, J. T. Sri Sumantyo, and H. Kuze, "Development of circularly polarized array antenna for synthetic aperture

radar sensor installed on UAV," Progress In Electromagnetics Research C, Vol. 19, 119–133, January 2011.

[46] H. Saito, and J.T Sri Sumantyo, “Synthetic Aperture Radar for UAVs and Small Satellites,” IEICE Trans. on Comm., Vol. J97-B No.11, pp.992-998, 2014.

[47] P. N. Tan, T. S. Lim, V. Gobi, and Y. K. Chan, “Design and development of a dual operating mode microstrip patch antenna for unmanned aerial vehicle synthetic aperture radar,” Progress In Electromagnetics Research C, Vol. 27, 143-156, 2012.

[48] J.F. Zurcher, and F.E. Gardiol, *Broadband Patch Antennas*, Norwood, M.A., Artech House: 1995.

[49] C. Wolff (2016, April 12). *Phased Array Antenna* [Online], Available: http://www.radartutorial.eu/06.antennas/Phased%20Array%20Antenna.en.html

[50] E. Hammerstad, “Computer-Aided Design of Microstrip Couplers with Accurate Discontinuity Models,” Symposium on Microwave Theory and Techniques, pp. 54-56, June 1981.

[51] J.S. Lee, E. Pottier, Polarimetric Radar Imaging from basics to applications, CRC Press, 2009, pp. 92-98.

[52] Y. Yamaguchi, "Fundamentals and applications of radar polarimetry," pp.66-67, IEICE, Tokyo, 2007.

[53] Agilent, *1287-12 Time Domain Analysis Using a Network Analyzer*, application note, literature number 5989-5723EN, 2012.

[54] X. Wang, C. Wang, Y. Liu, “RCS computation and analysis of target using FEKO”, Proc. Of 3rd Asia-Pacific Conf. on Antennas and Propagation, pp. 822 – 825, 2014.

[55] Y. Bennani, F. Comblet, A. Khenchaf, “RCS of complex targets: original representation validated by measurements—application to ISAR imagery”, IEEE Trans. on Geoscience and Remote Sensing, Vol. 50, No. 10, pp. 3882-3891, 2012.

APPENDICES

Appendix A MATLAB codes for conditioning Raw Data

The following MATLAB codes were to open measured the measured raw real and imaginary data and condition the data to be processed by the back-projection algorithm shown in Appendix B.

```
% ISAR IMAGING WITH BACKPROJECTION ALGORITHM
% POLARIMETRIC ISAR IMAGING OF METAL PLATE

% NOTE 1 : For LP select range gate as 2.25 and 2.85  (R0 : 2.55)
% NOTE 1 : For CP select range gate as 3.25 and 3.85  (R0 : 3.55)


clear all
clc
c = 299792458;

% Geometry
h = 0;                              % Height from ground to antenna

% Set antenna to target distance
r01 = 2.55;          % for LP
r02 = 3.55;          % for CP
R0 = r01;

% TX location in polar coordinates
TX_pol=[R0, 0*pi/180, h];

%% LOAD DATA

% FORMAT:
% Mfm : Scattering matrix = [HH  HV]
%                           [VH  VV]
% Mfm (2,2,N,P).... N: frequency points, P : angular points

%% Load Target Data
cd('C:\Measured_Data\Raw_Data_Compact')

if R0 == r01

    % CASE I: C-BAND LP POLARIZATION
    load M_Cband_lp;
    M_tar = M_Cband_lp;

    load freq_C_band_LP;
    freq = freq_C_band_LP;

    load th_C_band_LP
    th = th_C_band_LP;

else

    % CASE II: C-BAND CP POLARIZATION
    load M_Cband_cp;
    M_tar = M_Cband_cp;

    load freq_C_band_CP;
    freq = freq_C_band_CP;
```

```
    load th_C_band_CP
    th = th_C_band_CP;
end


 clear M_Cband_lp freq_C_band_LP th_C_band_LP ...
     M_Cband_cp freq_C_band_CP th_C_band_CP

%% Apply frequency mask
f1 = input('Select frequency mask start (in GHz, min:4, max:<8):');
f2 = input('Select frequency mask stop (in GHz, min:4, max:<8):');
if f1<4 || f1>8 || f2<4 || f2>8 || f2<=f1
    error('improper window, select between 4 and 8')
end

mask = ( (f1*1e9<=freq & freq<=f2*1e9));
freq = freq(mask);

% Clip Data
M_tar = M_tar(:, :, mask, :);
N= size(M_tar,3);
P= size(M_tar,4);

%% Frequency Related Parameters
if size(freq ,2)==1
    freq = freq';
end

% define the BP filter
kr = 4*pi*freq/c;
min_kr = min(kr);
H = kr;

%% TIME GATING
% Range and time vectors
df = freq(2)-freq(1);
Rmax=c/2/df;                        % Max unambigious range, m
r=linspace(0,Rmax,N);               % Range vector, m


% generate time domain signals
q_plate_11 = ifft(squeeze((M_tar(1,1,:,:))));
q_plate_12 = ifft(squeeze((M_tar(1,2,:,:))));
q_plate_21 = ifft(squeeze((M_tar(2,1,:,:))));
q_plate_22 = ifft(squeeze((M_tar(2,2,:,:))));


% Select gate
if R0 == r01
    disp('LP POL, R0 is around 2.55 m')
else
    disp('CP POL, R0 is around 3.55 m')
end

r1 = input('Select range mask start (in meters):');
r2 = input('Select range mask stop (in meters):');
if r1<0 || r1>Rmax || r2<=0 || r2>Rmax || r2<=r1
    error(['improper window, select between 0 and ' num2str(Rmax)])
end
```

```
mask = ( (r1<=r & r<=r2));
mask = repmat(mask', 1, P);

% make zero outside the window
q_plate_11 (~mask) = 0;
q_plate_12 (~mask) = 0;
q_plate_21 (~mask) = 0;
q_plate_22 (~mask) = 0;

% return to the frequency domain
Mga_tar = zeros(2,2,N,P);

Mga_tar(1,1,:,:) = fft(q_plate_11);
Mga_tar(1,2,:,:) = fft(q_plate_12);
Mga_tar(2,1,:,:) = fft(q_plate_21);
Mga_tar(2,2,:,:) = fft(q_plate_22);


%% APPLY ERROR CORRECTION
% load error coefficient matrix

if R0 == r01
    load C_lp
    C = C_lp;
else
    load C_cp
    C = C_cp;
end


% apply correction
Mga_tar_cal = zeros(2,2,N,P);

for k = 1:P
    for i = 1:N;
        CT = C([i i+N i+2*N i+3*N], :);
        a = inv(CT)*[Mga_tar(2,2,i,k); Mga_tar(1,1,i,k);
Mga_tar(2,1,i,k); Mga_tar(1,2,i,k)];

        Mga_tar_cal(1,1,i,k) = a(2);
        Mga_tar_cal(1,2,i,k) = a(4);
        Mga_tar_cal(2,1,i,k) = a(3);
        Mga_tar_cal(2,2,i,k) = a(1);

    end
end
```

Appendix B MATLAB codes for back-projection algorithm

The following back-projection algorithm written in MATLAB was used to generate an image profile. The algorithm was first developed by [24] and modified for this work.

```
%% ISAR IMAGING WITH BACK-PROJECTION

% polarimetric calibration, ... if desired
ncal = input('Apply calibration ?, y or n : ', 's');

% Windowing for Sidelob Supression ... if desired
nw = input('Appy windowing ?, y or n : ', 's');


% figure
figure, currfig=get(0,'CurrentFigure'); set(currfig,'Name','BPA
IMAGING RESULTS','Units', 'normalized'); figureFullScreen(currfig);

k = 0;
for n = 1:2
    for m = 1:2

        if strcmp(ncal, 'n')
            data_iq = squeeze(Mga_tar(n,m,:,:));
        else
            data_iq = squeeze(Mga_tar_cal(n,m,:,:));
        end

        if strcmp(nw, 'n')
            data_iq = data_iq.';
        else
            w=hanning(N); ww=repmat(w,1,P);
            data_iq = data_iq.*ww;
            data_iq = data_iq.';
        end

% number of FFT points
numFFTpts = 2*1024;

% image dimensions
num_pixels = 2*[128,128];                  % number of pixels
dim_image = 1.5*[-0.5 0.5 -0.5 0.5];           % image dimensions,
meters

% establish coordinates of final image (meters)
x_image = linspace(dim_image(1),dim_image(2),num_pixels(1));
y_image = linspace(dim_image(3),dim_image(4),num_pixels(2));
[X,Y] = meshgrid(x_image,y_image);
X=X(:);
Y=Y(:);

% calculate delay values for each projection
dr = c/2/(freq(end)-freq(1))*N/numFFTpts;
r_exact = dr*[0:numFFTpts-1];
% r_exact = r_exact-mean(r_exact);

% preallocate final image variables
```

```
image_data = zeros(num_pixels(2),num_pixels(1));


% loop over all theta angles
for i = 1:size(data_iq,1)

    % generate low-pass versions of projections
    q = ifft((data_iq(i,:)).*H,numFFTpts);

    % calculate the radii to image center
    [TX_x TX_y] = pol2cart(TX_pol(2)+th(i),TX_pol(1));
    TX_r = sqrt(sum([TX_x TX_y h].^2));

    % calculate the required radii for the image
    r_required_TX = sqrt((X-TX_x).^2+(Y-TX_y).^2+h^2);
%     r_required = (r_required_TX-TX_r);

    % interpolate q to radii required by the output image
    q_interp =
r_required_TX.^2 ./TX_r.^2.*interp1(r_exact,q,r_required_TX,'spline')
.*exp(1i*min_kr*r_required_TX);
%

    % form final image through back projection
    image_data = image_data +
reshape(q_interp,num_pixels(2),num_pixels(1));

end

% plot the output image
k =k+1;
subplot(2,2,k),
dyn_range=20;
image=20*log10(abs(image_data));
image=image-max(max(image));
index=find(image<-dyn_range);
image(index)=-dyn_range;
pcolor(x_image,y_image,image), shading('flat')
axis equal; axis tight
xlabel('Cross-range; y(m)','FontWeight','bold','FontSize',11);
ylabel('Range; x(m)','FontWeight','bold','FontSize',11);
sr=['ISAR Image of Metal Plate, C-band - ',num2str(n),num2str(m) '
POL'];
title (sr,'FontWeight','bold','FontSize',12)
colorbar

    end
end
```

PUBLICATIONS

Only papers submitted as the first author is listed.

Accepted Journal Papers:

1. Mohd Zafri Baharuddin, Yuta Izumi, Josaphat Tetuko Sri Sumantyo, Yohandri, “Side-lobe Reduced, Circularly Polarized Patch Array Antenna for Synthetic Aperture Radar Imaging,” in *IEICE Transactions on Electronics*, manuscript ID: 2016MMP0003, Vol.E99-C, No.10, pp.-, October 2016.
2. M. Zafri Baharuddin, Josaphat T.S. Sumantyo, and Hiroaki Kuze, “Suppressed Side-lobe, Beam Steered, C-band Circularly Polarized Array Antenna for Airborne Synthetic Aperture Radar,” in *Journal of Unmanned Systems and Technology*, accepted: 31 May 2016.

Submitted Journal Papers:

1. M. Zafri Baharuddin, Yuta Izumi, Josaphat T.S. Sumantyo, Hiroaki Kuze, and Sevket Demirci, “ISAR Imaging using Circularly Polarized Antennas in an Anechoic Chamber,” in *IEEE Geoscience and Remote Sensing Letters*, submitted **30 March 2016**.

Published Conference Papers:

1. M. Z. Baharuddin, K. Suto, J. T. S. Sumantyo, H. Kuze, L. T. Sze, J. Y. K. Shen, W. G. Cheaw, K. V. Chet, “Development of a semi-automated SAR test-bed,” *IEEE 2nd Intl. Symp. on Telecommunication Technologies (ISTT)*, Langkawi, 2014, pp. 236-240.
2. M. Z. Baharuddin, B. Setiadi, J.T.S. Sumantyo, H. Kuze, “An experimental network analyzer based ISAR system for studying SAR fundamentals,” in *IEEE 5th Asia-Pacific Conference on Synthetic Aperture Radar (APSAR)*, Singapore, 1-4 Sept. 2015, pp.103-107.

Presentations

1. M.Z. Baharuddin, Y. Osanai, and J.T. Sri Sumantyo, “Suppressed Side-lobe, Beam Steered, C-band Circularly Polarized Array Antenna for Synthetic Aperture Radar Measurements,” in *23rd CEReS International Symposium*, Chiba University, Japan, 2015.
2. Zafri Baharuddin, Prof. Josaphat Tetuko Sri Sumantyo, “Earth Observation using the GAIA-1 and GAIA-2 Satellite Platforms,” in *Japan Geoscience Union Meeting (JpGU)*, Makuhari Messe, Japan, May 2015.